Alma Mater Studiorum – Università di Bologna

DOTTORATO DI RICERCA IN

SCIENZE CHIMICHE

Ciclo XXII

Settore/i scientifico-disciplinare/i di afferenza: CHIM 03

TITOLO TESI

Synthesis and Physical-Chemical characterization of Metallic Nanoparticles

Presentata da: **Guido Fracasso**

Coordinatore Dottorato **Relatore**

Prof. Giuliano Longoni **Prof . Norberto Roveri**

Esame finale anno 2010

Synthesis and Physical-Chemical characterization of Metallic Nanoparticles

Introduction

Nanoparticles (particles of 1–100 nm in diameter) have generated intense interest over the past decades because of their unique electronic, optical, photoresponsive, and catalytic properties. However, nanoparticles are subject to the irreversible particle aggregation and the oxidation reactions. Thus the stabilization of nanoparticles against these problems is a requirement for further advancement in nanoparticle science and technology. In 1981, Schmid et al .[1] synthesized the first example of the ligandstabilized gold nanoparticles, Au55(PPh3)12Cl6. However, the dependable and practical formation of more stable an isolable monolayer-protected gold nanoparticles was achieved about a decade ago by Brust et al. [2]. The organic monolayers, which bind to the surface of metal nanoparticles, not only prevent aggregation of the metal nanoparticles, but also stabilize

them from harsh reaction conditions and enhance the solubility in various solvents[3–5]. Subsequent investigations were extended to different metal particles including Au, Ag,
Cu, Pt, Pd, Ni and alloy particles. Other organic compounds with different reactive head groups, such as thiol, disulfide, sulfide, thiosulfate, xanthate [38], phosphine, phosphine oxide, ammonium, amine, carboxylate, selenide, and isocyanide can protect metal nanoparticles by selfassembly assembly [6].

Monolayers with different functional groups and moieties can also be incorporated onto the surface of metal nanoparticles [3–5]. The modification of nanoparticles by the incorporation of a functional group is of potential significance for the expansion of chemical and biological applications of these nanomaterials. This review focuses on the synthesis of various metal nanoparticles protected with monolayers containing different reactive head groups and functional tail groups.

Gold nanoparticles

Gold nanoparticles have drawn remarkable interest in the last few years because of their high stability to oxidation and their optical and well-defined size-related electronic (e.g., quantized charging) properties [7,8]. Biological applications of hybrid Au nanoparticles have also shown a great promise for the use of these nanomaterials in biotechnology [4]. The synthesis of monolayer-protected gold nanoparticles will be described based on the reactive head groups, which provide self-assembly of organic monolayers onto the nanoparticle surface.

The stabilization of gold nanoparticles with alkanethiols was a direct result of advancement in the passivation of two-dimensional gold surfaces using alkanethiols in the late 1980s and early 1990s, which results in the formation of self-assembled monolayers on gold substrates [9]. The first report regarding the capping of Au nanoparticles with alkanethiols was made by Giersig and Mulvaney [10] in 1993. Brust et al. [2] reported a convenient two-phase synthesis of isolable and soluble alkanethiolate-protected gold nanoparticles in 1994, which had a huge impact on the nanoparticle research. In this reaction $AuCl_4$ was transferred to toluene using tetraoctylammonium bromide as the phase-transfer reagent. Addition of dodecanethiol to organic-phase $AuCl_4$ followed by the reduction with NaBH4 generated dodecanethiolate-protected gold nanoparticles. The research was extended to the alkanethiols with different chain lengths (C3–C24) [3].

Gold nanoparticles synthesized using the modified Schiffrin reaction generally have the average core size of 1–10 nm. The core size of gold nanoparticles could be controlled by modification of reaction conditions. It has been found that the nanoparticle formation behaves as a nucleation growth passivation process [3]. Therefore the average core size of particles gets smaller when a larger thiol/gold mole ratio is used, the reductant is added faster (<10 sec) at lower temperature, the

reaction is quenched after a shorter period of time (30 min to 1 h) has elapsed, or sterically bulkier ligands are used [3,4,11-13]. Because alkanethiolate-protected gold nanoparticles generated by the Schiffrin protocol are still somewhat polydisperse, there have been several studies aimed at getting more monodisperse particles using solubility fractionation, extraction, annealing, chromatography, and capillary electrophoresis [14,15]. Alkanethiolate-protected gold nanoparticles are generally considered as nonreactive species. By incorporation of o-functional groups to the monolayer, these nanomaterials can have specific functions and reactivities. p-Mercaptophenol-protected gold nanoparticles were synthesized directly from p-mercaptophenol and $AuCl_4$ in a one-phase system, which was reported first by Brust et al.[16] This research was extended to various ofunctionalized alkanethiols,[3–5] alkanethiols with internal amide groups,[17] thiols terminated with oligo- or polyethylene oxide [18], thiols with ionic liquids [19], fluorinated thiols [20], arenethiols [3], and crown ether-functionalized thiols[21] using the modified Schiffrin reaction and yielded various functionalized nanoparticles including watersoluble gold nanoparticles [3,4]. Later, a mixture of alkanethiols was also used to synthesize mixed monolayer-protected gold nanoparticles [22]. This result showed that the coadsorption of alkanethiols is governed by solvation-driven thermodynamic reactivities of the precursor ligands. When polymeric Au(I)-SG (glutathione: N-g-glutamyl-cysteinyl-glycine) was reduced with NaBH4 in water, it produced small (1–2 nm) water-soluble monolayer-protected gold nanoparticles [23]. The reduction of trithiol (thiocyanuric acid)-Au polymer precursor with potassium bitartrate resulted in the formation of watersoluble nanoparticles with varied geometric shapes [24].

Dithiol, trithiol, tetrathiol (thiolated resorcinarenethiolated a-, and thiolated b-cyclodextrin-protected gold nanoparticles were also reported [25–26]. Templeton et al. [3] reported the "ligand-place exchange'' method to modify the composition of the monolayer-protected nanoparticles. This research enabled incorporation of many different functional groups and moieties onto the surface of gold nanoparticles. In the exchange reaction, the incoming ligands replace the thiolate ligands on nanoparticles by an associative reaction, and the displaced thiolate becomes a thiol. The rate of ligand exchange depends on the chain length and/or steric bulk of the initial monolayers and electronic charge on nanoparticles. Various functional groups ranging from simple organic functional groups to functional complexes (electroactive or photochemical groups) were incorporated into the nanoparticles using ligand-place exchange reactions [3–5].

Reactions of functionalized gold nanoparticles were also frequently used for the incorporation of more specific organic groups and moieties having electroactive, photoresponsive, catalytic, mechanical, and biological properties [3–5].

In this work, Au, Au4/Ag1 and Au1/Ag4 nanoparticles were synthesised with the aim to fill chrysotyle nanotubes hollows. Decanethiol was used to coat the nanoparticles surface with the pur pose to fill the nanotube cavities with the nanoparticles owing to an interdigitation process occurring between the long alkilic chains on neighbouring nanoparticles.

Ag nanoparticles

Recently, research efforts have been intensified for the synthesis of Ag nanoparticles because of important roles played by Ag particles in antimicrobial applications, catalysis, and as a substrate for SERS. Thiols [27,28] have been the most popular choice of capping reagent for Ag nanoparticles because of a higher stability over other capping reagents, such as amines [29,30] and carboxylates [31, which are weakly anchored to Ag particle cores. Other organic compounds, such as dialkyl disulfides [32,33], dialkyl sulfides [34], thiosulfates [35], thiosalicylic acids [36], and xanthates[37] have been used to generate monolayer-protected Ag nanoparticles.

Ag nanoparticles protected with different organic species have been prepared. In fact a synthesis of alkylamine-capped silver nanoparticles was developed using thermal decomposition of [Ag(m-mesityl)4] (mesityl=2,4,7-$Me_3C_6H_2$) derivatives in alkylamine solution [38]. Two-phase (n-heptane/water) $NaBH_4$ reduction of N-hexadecylethylenediamine silver nitrate complex produced N-hexadecylethylenediamine-protected silver nanoparticles [39]. The colloidal solution of diamine- protected silver nanoparticles was free from flocculation and aggregation for several months.

Long-chain carboxylates (or fatty acids) have been one of the most commonly used ligands for silver particles [40-42]. The simple dissolution of silver 2-ethylhexanoate in DMSO (as both a solvent and reducing agent) produced silver nanoparticles [40]. Addition of stabilizing agent, sodium citrate, produced stable yet catalytic monolayer-protected silver nanoparticles. Thermal reduction of silver trifluoroacetate in isoamyl ether in the presence of oleic acid generated Ag nanoparticles with diameters in the range of 7–11 nm with narrow size distribution [42].

Surface-enhanced Raman scattering studies of 4-biphenylisocyanide of silver nanoparticles proved the adsorption of isocyanide on silver surfaces [43]. Dyeprotected silver nanoparticles were prepared through the reduction of metallic Ag ions by $NaBH_4$ in aqueous media [44]. The dye used was a cyanine derivative, 5,5'- dichloro-3,3-disulfopropylthiacyanine sodium salt.

Alkanethiolate-protected Ag nanoparticles were synthesized using the modified two-phase Schiffrin reaction [45-46]. Two-dimensional ordered superlattices of the Ag nanoparticles could be formed by evaporating a drop of the particle solutions on carbon films [46]. The fluorinated thiol-capped Ag nanoparticles could be prepared using the $NaBH_4$ reduction of $AgNO_3$ in the presence of

perfluorodecanethiol in acetone/water. These particles could be redispersed in acetone and liquid and supercritical CO_2 [47]. Thiolated b-cyclodextrin-protected Ag nanoparticles were also synthesized from $AgNO_3$.[48] N,N-Dimethylformamide (DMF) was used as both the solvent and the reducing agent in this reaction. Synthesis of water-soluble tiopronin-protected Ag nanoparticles was also reported [49].

Unlike Au nanoparticles functionalized by the adsorption of dialkyl disulfides, the monolayers of alkanethiolate- protected Ag nanoparticles derived from dialkyl disulfides were somewhat less crystalline than those prepared similarly from alkanethiols [32]. Positively charged Ag nanoparticles were synthesized by the $NaBH_4$ reduction of $AgNO_3$ in the presence of quaternary ammonium dialkyl disulfides [50]. Adsorption of benzyl phenyl sulfide on silver nanoparticles in water has been studied [51]. Alkanethiolate-protected Ag nanoparticles were synthesized from sodium S dodecylthiosulfate in aqueous solution [52]. Silver nanoparticles, produced by the borohydride reduction of $AgNO_3$ in H_2O, were stabilized by the adsorption of S-dodecylthiosulfate followed by the removal of the SO_3 moiety.

Alkyl xanthates were also used for the capping of Ag nanoparticles [37]. Xanthate-capped Ag particles are less hydrophobic than alkanethiol-protected Ag nanoparticles and less stable than the oleate-capped particles (but still stable in aqueous solutions for over a month). Thiosalicylic acid (TSA)-functionalized silver nanoparticles were synthesized from $NaBH_4$ reduction of TSA-AgNO3 in aqueous ethanol solution.[53].

Copper nanoparticles

Because of the expected marked electronic and optical properties of copper nanoparticles, there has been an increased interest in the preparation of stable monolayer-protected copper nanoparticles. Alkyl xanthates [37], alkylamines [29], tetraalkyl ammonium complexes [54], and alkanethiols [55, 56] ligands have been utilized to protect copper nanoparticles. However, a limited progress has been obtained because of the high instability of copper nanoparticles. In order to contrast copper nanoparticles, irreversible aggregation and oxidation, Chen and Sommers [55] have prepared copper nanoparticles protected by alkanethiolate in one-phase system. Their prepared spherical (1-2nm in diameter) Cu particle bound hexanethiolate monolayers undergo to the oxidation of copper core, morphological evolution, and irreversible aggregation process. Long-chain alkanethiols, which have been found to selfassemble into compact monolayers (i.e., three-dimensional self-assembled monolayers) on metallic nanoparticles [57,58], cannot only induce metallic nanoparticles to be readily isolated, but also reduce their conductivity [37].

Copper thiolates are generating intense research interest because of their possible applications in

technological, chemical and biomedical fields.

Recently nanorods, nanodisks and nanoplatelets of the semiconducting material Cu_2S were obtained by thermolysis of copper alcanethiolates [59] and the semiconducting nature of a copper thiolate has been reported [60].

In organic chemistry, copper arenethiolates act as catalysts in many organic reactions [61,62].

Copper thiolate clusters are present in many proteins and play an important role in cell metabolism. Recently a novel [(His)7Cu4(í4-S)] cluster was discovered in the active site of nitrous oxide reductase [63].

Thiolate protected copper nanoparticles can be regarded as assemblies of copper thiolates fastened on a metallic core that acts as templatig device. From this point of view they can be new usefull tools in organic synthesis and catalysis. Furthermore thiolate protected copper nanoparticles can represent starting materials to obtain new copper complexes with S donor ligands.

Concerning with the electronics field, the insulator metal transition has been discovered to occur at 270, 255, and 25 K for arrays of copper nanoclusters passivated with 1-decanethiole, lauric acid and tridecilamine respectively [64].

Thiolate protected copper nanoparticles for chemical, technological and biomedical applications must have adequate stability and an elevated degree of monodispersion. Furthermore the organic thiolate moieties on the nanoparticle surface must produce the minimal steric hindrance to improve their interactions with molecules or other nanoparticles. Unfortunately short chain alcanethiols or aryl thiols can be inadequate in protecting nanoclusters core against oxidation [64-66] and gaps form easily on the nanoparticle surface protected with small thiol molecules less fastened together by Van Der Vaals interactions than long chain (CH_2>8) thiols.

Synthesis methods reported in literature to obtain thiolate protected copper nanoparticles involve usually $Cu(NO_3)_2$ and $CuCl_2$ reactions with long chain alcanethiols (CH_2>8) while ethanol, tethrahydrofuran, water or mixtures of these are used as solvents. The reduction of copper-thiol adducts is obtained by $NaBH_4$ solubilized in ethanol or water or by $LiBH_4$ in tetrahydrofuran (superhydride) [64,66]. Diffractometric and XPS analysis reveal that Cu_2O is present in negligible quantity or even absent in the core of these thiolate protected copper nanoclusters [64]. However they are quite polydispersed probably due to the formation of insoluble copper – thiol adducts before the reduction step. Furthermore long chain alcanethiolates protecting the nanoparticles core can limit their possible chemical catalitic or biological properties and give rise to irreversible aggregation processes due to interpenetration (interdigitation) of the alchilic chains on their surfaces.

We recently started a research program to investigate how the physicochemical conditions

occurring during the syntheses and the nature of the thiols used can influence structure, and stability of copper nanoparticles.

The comprehension of these parameters is useful in tuning their properties for possible applications in many fields both technological and biomedical. The aim of this study is to synthesize 3-(6-mercaptohexyl) thiopheneprotected copper nanoparticles which, in absence of long chain alkanethiols and in absence of irreversible aggregation, could represent new high-conductive metallic nanoparticles with improved potentialities of tuning their optical and electronic properties.

To increase the stability of copper nanoparticles protected with other thioletes, we have developed and compared three synthetic routes in this work. Butanethiol and 4-methilbenzenethiol were used in the syntheses with the aim of reduce the sterical hindrance during the interactions of the nanoparticles with molecules, templating structures or other kinds of substrates.

Selenium

Research activity in selenium chemistry and physics is continuously growing due to both thecnological and biomedical relevance of this element. The grey purplish trigonal selenium with its structure of long helical chains of atoms is the most thermodynamically stable allotropic form and reveals light enhanced semiconductive properties. This feature make it an usefull and cheap substitute of silicon in the photovoltaic cell fabrication. Selenium is also used in photographic exposure meters. It has also found to improve the abrasion resistence of vulcanized rubber.

Concerning with the biological field, selenium plays a fundamental role in cell metabolism being responsible of many enzymes and other proteins activity. Among these glutathione peroxidase reduces lipid hydroperoxides to the corresponding alcohols and hydroperoxide to water so removing strong oxidizing molecules responsible of the cellular oxidative stress.

Studies on nanometric size selenium structures and selenium nanoparticles give rise to an always increasing research work owing to the novel electronic, optical, photoresponsive, and catalytic properties that nanometric dimensions confer to the materials.

Syntheses reported in literature of nanoparticles or other selenium nanostructure imply the reduction of selenous oxide by means of many reducing agents: among these can be mentioned or glutathione [67] hydrazine [68] dextrose [69], ascorbic acid [70] sodium ascorbate [71], sodium thiosulphate [72].

Selenium nanostructures of variable shapes and sizes like nanowires [73], and hollow nanospheres [74] were obtained using oligosaccarides and proteins respectively as templating devices.

However selenium nanotubes were obtained by a hydrothermal synthesis also in absence of templating structures. In this case sodium formiate was used to reduce selenous oxide and the reaction was completed in 25 hours at 100°C [75].

Polivinil alcohol [76] gelatine [77] and other large molecules were used to obtain stable and as far as possible monodispersed selenium nanoparticles and to prevent their irreversible aggregation.

These molecules however are weakly adsorbed by means of Van der Waals forces to the selenium nanoparticle surfaces so delaying but not stopping nanoparticle nuclei aggregation processes. Stable well monodispersed nobel metal nanoparticles with sizes of two to four nanometers were synthesized coating their surface with alcanethiols or other molecules bearing the thiolic function chemically bonded by means of the sulphur atoms to the nanoparticle surface by Brust and co-workers [2]. On the suggestion of this work, we have synthesized selenium nanoparticles protected by phenolic molecules chemically bonded to their surface.

Selenium shows both metallic and non-metallic properties and can form organic and inorganic compounds functioning both as an oxidant and reductant [78]. Selenium exists in the environmental and biological systems in the form of inorganic species, toxic and soluble Se(IV) ($SeO_3^{2-,}$ selenite), Se(VI) (SeO_4^{2-}, selenate), insoluble and non-toxic elemental Selenium, the most acutely toxic selenide (e.g. HgSe) and also organoselenium compounds in a wide range of molecular masses, resulting much less toxic if compared with the inorganic Selenium species. Selenium shows ambivalent behaviour; in fact, it is essential for life and can be toxic little beyond health levels. Dietary levels for the desired Se amount are in a very narrow range. Food intake containing Se above 1 mg Kg -1 leads to toxic manifestation, whereas intakes lower than 0.1 mg Kg -1 of Se results in deficiency [79,80].

The biochemical role of Selenium started with its discovery in the active site of glutathione peroxidise [81,82], it increased through the discovery of many selenoproteins [83] and selenoenzymes [84-87] and has been widely described [88-91]. During the past decades many stable organoselenium compounds have been synthesised to be used as antioxidants, enzyme inhibitors, antitumor and anti-infective agents, cytokine inducers, immuno-modulators and biological models to simulate catalytic functions of natural ezymes [92-96].

Se anticarcinogenic effects by multiple mechanisms have been extensively investigated and documented [97,98]. Se is defined a genuine nutritional cancer-protecting element and a significant protective effect of Se against major forms of cancer; dietary intakes in the range of 200-300 g/day are suggested for this purpose [99,100]. Metallic nanoparticles with size ranging from 1 to 100 nm in diameter have generated intense interest over the past decades because of their unique electronic, optical, photoresponsive, catalytic and biological properties. However, these nanoparticles have to

be stabilized against irreversible aggregation and oxidation reactions. In 1981, Schmid et al. [1] synthesized the first example of the ligand-stabilized gold nanoparticles; however, only a decade ago, the more stable and monolayer-protected gold nanoparticles were achieved by Brust et al.[2]. The organic monolayers, which bind to the surface of metal nanoparticles, not only prevent their aggregation, but also stabilize them from redox reactions and enhance their solubility in various solvents [3-5]. Selenium containing nano-materials have excellent photoelectrical characteristics, semiconductor properties and high biological activity [7].

Both reduction and oxidation techniques can be employed to prepare Selenium nanoparticles, starting with suitable precursors. Most of the work on the production of Se nanoparticles has been obtained by the reduction method, using no biocompatible reagents like glycol, hydrazine, surfactant, high temperature etc. [8]. Se(0) nanoparticles have been obtained by bacteria reduction of selenite [101] and by oxidation of its precursors as well [102]. Stable Se nanoparticles have been synthesized in polymer media such as hydroxyethylcellulose [103], polyvinylpyrrolidone [104] and also by natural biopolymer like chitosan [105]. Polyvinyl alcohol stabilized spherical Se nanoparticles in a size range of 20-80 nm have been synthesized from an aqueous sodium selenosulphate precursor by sulphuric acid [106]. Selenium was obtained in different nanostructures like nanorods, nanowires, nanotubes and nanospheres for high technological applications [107-109]. Many efforts have been performed in order to develop novel greener methods to obtain metallic nanoparticles by using vitamin B2 and vitamin C as reducing and capping agents, due to their high water solubility, biodegradability and low toxicity compared with the common reducing agents (sodium borohydride, hydroxylamine hydrochloride or surfactants) [110.111]. Green tea containing Selenium revealed higher antioxidant and prebiotic activities than common green tea [112]. This is probably due to the synergy obtained with the contemporary presence of Se and polyphenols like epigallocatekina gallato and teaflavina, which contain some phloroglucinol rings like quercitine, antocianine and flavonoids, which are notorious natural antioxydant agents [113]. Among phenol molecules, phloroglucinol is one of the strongest reactive since its three hydroxyls orto-para orienting are able to activate electrofilic attachment in every free C in the molecule. Phloroglucinol was found to possess cytoprotective effects against oxidative stress [114], thanks to reactive oxygen species (ROS) which are associated with cells and tissue damages and are the contributing factors for inflammation, aging, cancer, arteriosclerosis, hypertension and diabetes [115-120]. The aim of this paper is to report a new method to synthesise in mild conditions amorphous Se nanopaticles surface capped with phloroglucinol, which is used during synthesis as reducing agent to obtain stable Se nanoparticles in ethanol, performing the synergies offered by the specific anticarcinogenic properties of Se and the antioxiding ones of phloroalucinol.

Synthetic chrysotile nanotubes

Asbestos is the usual term indicating a number of mineral silicates with a markedly fibrous asbestiform habit which belong to the amphibole and serpentine families. In fact, these minerals are made up of incombustible, chemically resistant, inert, phono-absorbing, flexible and tensile fibers. The chemical and physical properties of asbestos made it, in past decades, one of the most important inorganic materials for industrial uses and technological applications. In fact, the asbestos minerals were the components of a large variety of building materials such as cement products, acoustic and thermal sprays, pipe and boiler wraps, flooring and roofing materials, plasters, paints and many others [121]. The three most common types of asbestos are: a) chrysotile, b) amosite and c) crocidolite. Chrysotile, also known as white asbestos and a member of the Serpentine mineral group is the most common.

Asbestos chrysotile ($Mg_3Si_2O_5OH_4$) structure consists of wrapped sheets composed of layers of Si-centered tetrahedra in a pseudo-hexagonal network joined to layers of octahedral Mg hydroxides (Fig. 1).

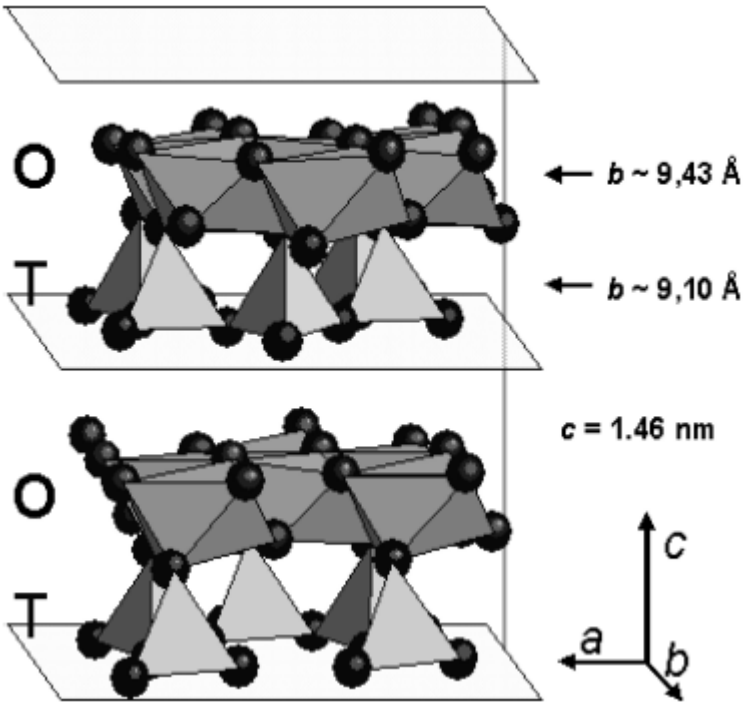

Fig. 1. A prospective view of OT layers in the chrysotile structure. Mg environment is represented by octahedral, Silicon environment bytetrahedral. Different lengths along the b-axis for O-T layer is reported.
[Reproduced by permission of G. Falini, E. Foresti, M. Gazzano, A.F. Gualtieri, M. Leoni, I.G. Lesci, and N. Roveri: Tabularshapedstoichiometric chrysotile nanocristals. Chem.-Eur. J. 10, 3043 (2004).]

Layers are concentrically or spirally wound preferentially around the x-axis (clinochrysotile and orthochrysotile), and seldom around the y-axis (parachrysotile), into a tubular structure of about 22–27 nm in diameter. The rolls possess a hollow core of about 7 nm, due to the mismatch along the b direction of the smaller layer dimension of the SiO_4 sheet with respect to the $Mg(OH)_2$ layer (Figs. 2 and 3).

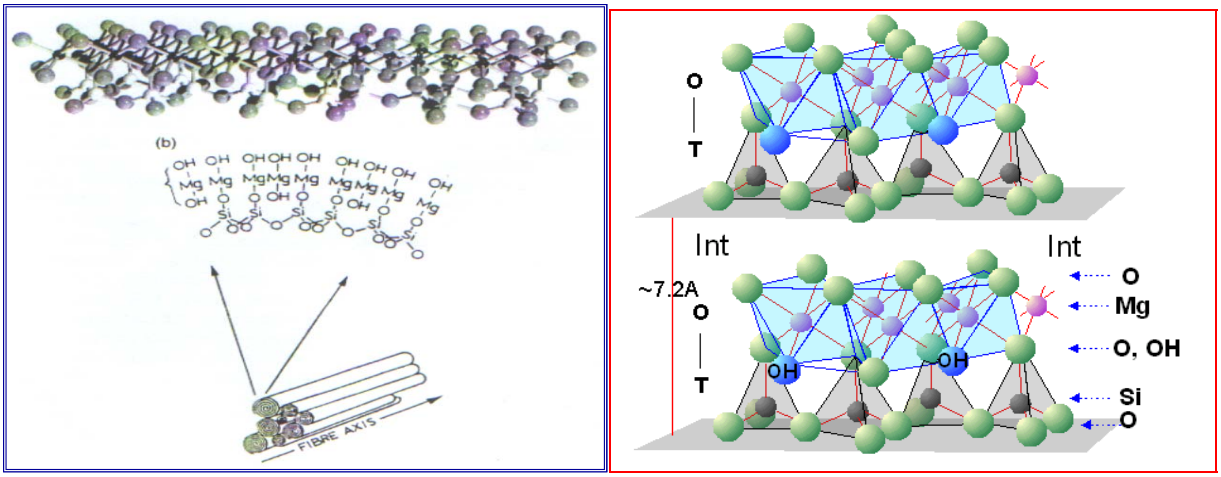

Fig. 2

These fibers are contaminated with trace metals such as Al, Ni, and Fe, which can be replaced with Mg and Si, usually developing structural defects [122]. This heterogeneity can be invoked to explain the different chrysotile crystal morphologies observed: hollow cylinders, non-hollowed cylinders, tube-in-tube fibers, conically wrapped fibers, cone-in-cone-shaped concentric spiral structures, and multispiral structures (Fig.3) [123].

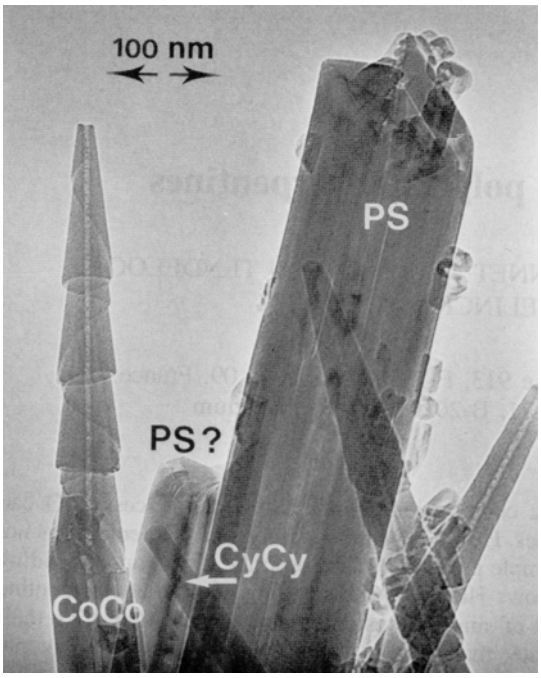

Fig. 3. Natural chrysotile nanocristals

The high degree of heterogeneity in chrysotile strongly affects the biological–mineral system interactions, which has been widely investigated to single out the causes of health hazards associated with asbestos fibers [124,125]. Actually, several investigations have been reported that asbestos toxicity may be related to the production of reactive oxygen species (ROS) and other free-radical species, even if genetic factors can also be invoked [126-128].

The capability of asbestos fibers to enhance ROS production is believed to depend both on their chemistry and their morphology [129.130]. In addition, their physicochemical properties are also responsible for their solubility, biodurability, and biopersistence [131]. Fiber properties, related to their cytotoxicity [132,133] and mutagenic response [134], are strongly affected by the surface chemical features, which are fully responsible for the interaction with the biological environment.

Natural chrysotile, formed by densely packed bundles of multiwalled hollow nanotubes, is a mineral very suitable for nanowires (NW) preparation when their inner nanometer-sized cavity is filled with a proper material. Bundles of chrysotile nanotubes can then behave as host systems, where their large interchannel separation is actually expected to prevent the interaction between individual guest nanoparticles and act as a confining barrier.

Chrysotile nanotubes have been filled with molten metals such as Hg, Pb (Fig.4), Sn, semimetals, Bi, Te, Se, and with semiconductor materials such as InSb, CdSe, GaAs, and InP using both high-pressure techniques [135] and metal-organic chemical vapor deposition (MOCVD) [136,137]

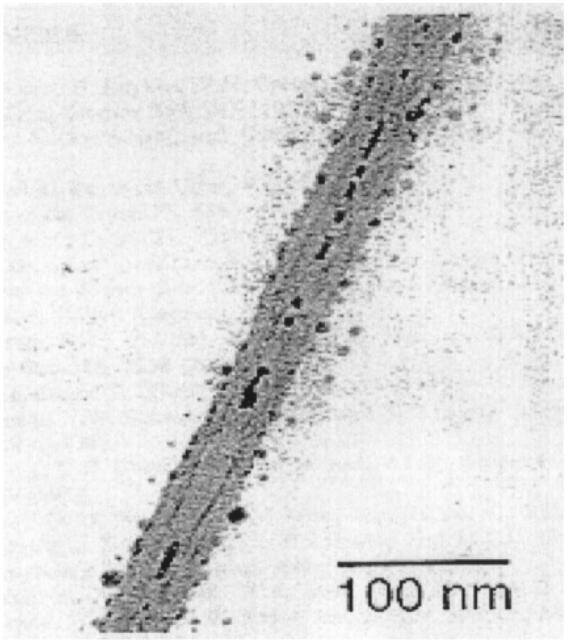

Fig. 4. TEM image of an isolated mineral chrysotile nanotube partially filled with lead. [Reproduced by permission of C. Metraux, B. Grobety, and P. Ulmer: Filling of chrysotile nanotubes with metals. J. Mater. Res. 17(5), 1129 (2002).]

A variety of semiconducting ultrathin filaments, real quantum wires, inside mineral chrysotile nanotubes have been prepared by means of injection of molten semiconducting materials into the asbestos channels.

CdSe and GaAs have been synthesized inside the channels of mineral chrysotile nanotubes [138,139].

Recently, hydrothermal synthesis of chrysotile has been utilized primarily for the purpose of obtaining pure chrysotile nanocrystals as a reference standard for ongoing investigation of asbestos cytotoxicity and carcinogenicity. A second aim, but not less important, is their use as new synthetic inorganic nanotubes with high potentiality for application in the developing field of nanotechnology.

The optimum hydrothermal conditions to synthesize chrysotile nanocrystals as a single phase are reported to be 300 °C, 82 atm, using SiO_2 mesophase MCM41 previously synthesized according to Kresge et al. [140] and $MgCl_2$ as a starting material, Si/Mg molar ratio equal to 0.66, pH 13, reaction time longer than 24 h [141]. The high purity of the synthesized chrysotile nanocrystals can be evinced by microcalorimetric and spectroscopic analysis. DTA and TGA curves do not show any of the additional peaks or bands usually assigned to impurities associated with mineral chrysotile.

TEM images of stoichiometric synthetic chrysotile nanocrystals with single-tube morphology is reported in Fig. 5(a), witnessing a high structural and morphological uniformity. Figure 5(b) reports

a selected area electron diffracting (SAED) image of a chrysotile nanocrystal showing the typical split of the diffraction spots due to the cylindrical crystal lattice, resembling what was observed by Yada in 1967 in a mineral sample [142]. The powder diffraction refinement of the nanochrysotile structure was obtained with a model composed of a statistical assembly of six layers, a reasonable approximation of the cylindrical stacking with random disorder along the b-axis. Hydrogen atoms were also included for completeness but not refined; their positions were adapted from those refined for lizardite, the planar analogue of chrysotile [143]. The availability of pure synthetic crystalline crysotile nanocrystals allowed to refine the structural and microstructural parameters using a modified version of DIFFaX software[144]. The new unit cell parameters for the ideal orthogonal layer are: a _ 0.5330(1), b _ 0.9220(1), c_0.73508(9) nm [145]. The structure has been refined also by means of General Structure Analysis System (GSAS) anisotropic broadening parameters along the b-axis, by using the stacking fault model, improving the previous model used for the quantitative phase analysis with the Rietveld method on a natural and obviously impure standard sample [146]. The search for the best space group indicates a Cc space group with c _1.469 nm, which corresponds to an OT layer thickness of 0.734 nm. The present result proves extremely useful in that it fills the gap opened in the literature, since Wicks demonstrated the I inconsistency of chrysotile space group [147]. Transmission electron microscopy analysis was carried out on synthetic chrysotile nanocrystals, showing the cylindrical shape of many microns in length. The central area that runs longitudinally along the crystal indicates that the crystal core is void or containing low electron dense material. The hollow tubular morphology of a typical single crystal is clearly shown in Fig. 5, top, where three tubular subunits are concentrically arranged in a telescopic form.

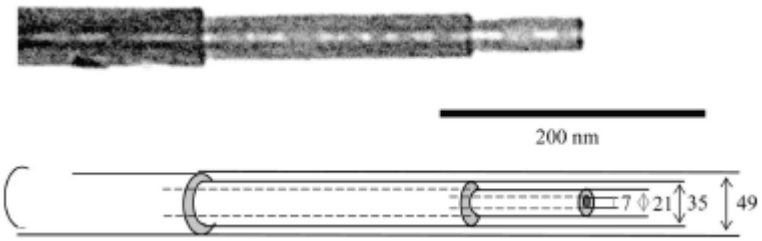

Fig. 5 (top) TEM image of a single tubular chrysotile nanocrystal; (bottom) graphical representation of the nanocrystals including dimensions in nm. [Reproduced by permission of G. Falini, E. Foresti, M. Gazzano, A.F. Gualtieri, M. Leoni, I.G. Lesci, and N. Roveri: Tubularshaped stoichiometric chrysotile nanocristals. *Chem.-Eur. J.* 10, 3043 (2004).]

A value of 7 ± 1 nm for the central hole diameter as well as for the average wall thickness was determined by TEM. Atomic force microscopy (AFM) imaging has been used to evaluate the mean outer diameter of single, double, and triple tubes concentrically arranged as 21 ± 1, 35 ± 1, and 49 ± 1 nm respectively [148]. A detailed investigation into hydrothermal reaction mechanism leading to chrysotile nanotubes was performed by [149]. They followed the reaction products after using different combinations of reagents, such as MgO, SiO_2, $MgSiO_3$, and $Mg_3[Si_4O_{10}](OH)_2$, at pH >13 and several temperatures between 100 and 450 °C and observed that chrysotile nanotubes formed most quickly in the range of 350–400 °C using SiO2 and MgO as reactants. In addition, compounds with a layered structure are the first step towards the formation of $Mg_3Si_2O_5(OH)_4$ nanotubes under hydrothermal conditions.

The opportunity to have geomimetic sybthetic chrysotyle nanotubes allowed to utilize these inorganic nanotubes to be filled with different metallic nanoparticles.

Biomimetic hydroxyapatite nanocrystals as carriers for Au/Ag alloy anticancer particles

Control at the nano-scale is a fundamental concern in the production of biomimetic materials, particularly in the case of bone substitutes where the chemical and biological properties are very much size dependent. In fact, as the mineral phase of bone is constituted of carbonated hydroxyapatite (HA) nano-crystals, biomimetic calcium phosphates need to be synthesized with similar nanoscale dimensions, as well as with properties such as low crystallinity, non-stoichiometric composition, crystalline disorder, and presence of carbonate ions in the crystal lattice. On the other hand, nanoparticles with unique optical properties, facile surface chemistry and appropriate size scale are generating much enthusiasm in nanomedicine.

Noble metal, especially Au nanoparticles has immense potential for both cancer diagnosis and therapy. In the first case in fact, due to the phenomena of the surface plasmon resonance the adsorption and scattering cross-sections of Au nano-particles are significantly superior to the absorbing and fluorescent dyes conventionally used in molecular biology and nanomedicine. In this way conjugation of Au nano-particles to ligands specifically targeted to biomarkers on cancer cells allows molecular specific imaging and detection of cancer. On the other hand, Au nanoparticles efficiently convert the strongly adsorbed light into localized heat, which can be exploited for the selective laser photothermal therapy of cancer.

According to the about, metal nanoparticles-HA nanocrystals composites should have tremendous potential in novel methods for therapy of cancer [150] and represent innovative approach to fine-tune cellular response of implanted nano-biomaterials by environmental stimuli (above all light).

In this work Au-Ag alloy nano-particles have been conjugated to HA nanocrystals trough mercapto-undecanoic acid a linker.

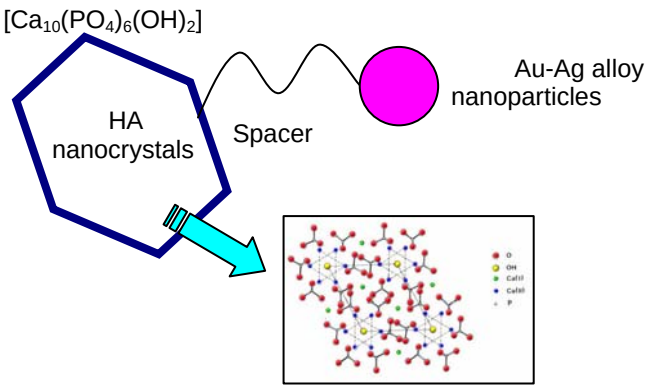

It worth notice that nanomaterials exhibit multi-functional properties if building blocks have been combined through structural and morphological integration at the nanoscale. As a consequence of it, the structural organization of the resulting composite need to be controlled.

Finally, the formation of hydroxyapatite/metal nano-particles assembly opens fascinating perspectives for the biological implication derived from conferring conductive properties to calcium phosphates nanocrystals.

Exsperimental

Reagents and solvents

1-butanethiol (Fluka; 97%), $CuCl_2$ (Aldrich); 4-methylbenzenethiol (Aldrich, 98%) LiBr (Riedel de Haen, pure grade); ascorbic acid (Sigma, 20-200 mesh); lithium chloride (Fluka, 99%); tetrabutylammonium bromide (Fluka, 98%); sodium borohydride (Sigma Aldrich, 98%); dichloromethane (Sigma-Aldrich, pure grade); methanol (Fluka, 99,8%); diglyme (Aldrich, 99%); Tetrahydrofurane (Riedel de Haen; 99%).

Synthesis of surface protected metallic nanoparticles:

The surface protected metallic nanoparticles were synthesized in a two phase system as reported in literature [151,152]. Reagents and solvents used are listed below: $AgNO_3$(>_99,0%;Acros Organics), $AuCl_3$.HCl(Aldrich; concentred hydrochloric acid 30% solution), KBr(Sigma-Aldrich; 99,5%) dacanethiol (Aldrich; 96%) butanethiol (Aldrich; >_99%), 4-methylbenzenethiol(Aldrich;98%), $NaBH_4$(Aldrich;>_98%); toluene (Sigma-Aldrich; 99,5%), MilliQ-water and tethraoctilammonium bromide (TOABr) (aldrich;98%).

Synthesis of surface protected Ag nanoparticles

Solutions of silver nitrate and potassium bromide were mixed in a 250 ml three naked round bottom flask. The metal salt concentration, and the final volume were 0,05 mmoles/ml, and 30 ml

respectively. After addition of TOABr (20 ml of a 0,150 molar solution in toluene) under continuous stirring the precipitate in the water phase disappeared in about 30 minutes indicating the complete removal of the metallic salts from the water to the organic phase. 30 ml of thiol solution in toluene (0,0410 molar in the case of 4-methylbenzene thiol and 0,1 molar in that of butanethiol and decanethiol) were then poured in the flask followed by 15 ml of a 0,70 molar solution of $NaBH_4$ in MilliQ-water.

After three hours of continuous stirring, the organic phase was separated from the water phase, repeatedly washed with Milli-Q water and dried with Na_2SO_4. The toluene was removed under vacuum conditions, the residue redispersed in few ml of dichloromethane and finally dropped in methanol cooled at -10C°. The black brown precipitate was repeatedly washed with cooled methanol and redispersed in 40 ml of dichloromethane (mother suspension).

Synthesis of surface protected Au nanoparticles

Hydrogen tetrachloroaurate (30 ml of a 0,05 molar solution) was mixed with TOABr (20 ml of a 0,150 molar solution in toluene) in a 250 ml three naked round bottom flask under continuous stirring. The orange color in the water phase disappeared in about 30 minutes indicating the complete removal of the auric salt from the water to the organic phase. 30 ml of thiol solution in toluene (0,0410 molar in the case of 4-methylbenzene thiol and 0,1 molar in that of butanethiol and decanethiol) were then poured in the flask followed by 15 ml of a 0,70 molar solution of $NaBH_4$ in MilliQ-water. After three hours of continuous stirring, the organic phase was separated from the water phase, repeatedly washed with Milli-Q water and dried with Na_2SO_4. The toluene was removed under vacuum conditions, the residue redispersed in few ml of dichloromethane and finally dropped in methanol cooled at -10C°. The black brown precipitate was repeatedly washed with cooled methanol and redispersed in 40 ml of dichloromethane (mother suspension).

Synthesis of surface protected Ag/Au nanoparticles

Solutions of silver nitrate, hydrogen tetrachloroaurate, and potassium bromide were mixed in a 250 ml three naked round bottom flask. The overall metal salt concentration, and the the final volume were 0,05 mmoles/ml, and 30 ml respectively with silver to gold ratios of 1/0, 4/1;1/4; 0/1 in each synthesis. After addition of TOABr (20 ml of a 0,150 molar solution in toluene) under continuous stirring the precipitate in the water phase disappeared in about 30 minutes indicating the complete removal of the metallic salts from the water to the organic phase. 30 ml of thiol solution in toluene

(0,0410 molar in the case of 4-methylbenzene thiol and 0,1 molar in that of butanethiol and decanethiol) were then poured in the flask followed by 15 ml of a 0,70 molar solution of $NaBH_4$ in MilliQ-water.

After three hours of continuous stirring, the organic phase was separated from the water phase, repeatedly washed with Milli-Q water and dried with Na_2SO_4. The toluene was removed under vacuum conditions, the residue redispersed in few ml of dichloromethane and finally dropped in methanol cooled at -10°C. The black brown precipitate was repeatedly washed with cooled methanol and redispersed in 40 ml of dichloromethane (mother suspension).

Preparation of 11mercaptoundecanoic acid protected Au-Ag nanoparticles

The 1-buthanethiol surface protected Au4/Ag1 nanoparticles isolated as a brown precipitate, were re-dispersed in tetrahydrofuran (30 ml) using TOABr (427,85 mg; 0,8 mille-moles) as solubilizer and the 11-mercaptoundecanoic acid (419,57g; 0,50 mille-moles) to replace the 1 buthanethiol on the nanoparticle surface .

The reaction mixture was kept under continuous stirring in a 100 ml round bottomed flask for 90 minutes. The residue obtained evaporating the solvent, was re-dispersed in 10 ml of methanol, added to a solution of Na_2CO_3 deca-hydrate (5g; 0,017 moles in 40 ml of milliq water) and stirred for two hours. The obtained dispersion has been washed with 60*3 ml of diethylether. The precipitate formed in the water phase was collected by centrifugation.

Synthesis of CuBr

Ascorbic acid (25 ml of a 0,52 molar water solution) was added dropwise to a water solution of lithium bromide(4, 37g; 0,05 moles) and cupric chloride (4,257g; 0,025 moles) under continuous stirring and nitrogen flux. The white precipitate (sometimes pale yellow) was allowed to stir for half an hour. It was separated by centrifugation at 3000 rpm, washed with water, methanol and finally with diethylether. After dryng under vacuum it was stored in a dessiccator.

Synthesis of butane thiolate protected Cu nanoparticles (I method)

Cuprous bromide (429 mg; 3,0mmoli) was solubilized by means of tetrabuthylammonium bromide TBABr (1,100g; 3,4 mmoli) in 120ml of tethrahydrofuran together with 960 ml (9 mmoles) of 1-butanethiol. The formation of a precipitate was not observed. After ten minutes 45 ml of a LiCl-$NaBH_4$ diglyme suspension* was dropped in the reaction mixture with a dropping time of about 5 minutes under continuous stirring and nitrogen flux. The colour of the solution changed rapidly from pale yellow-green to dark brown and a white precipitate became to form. The reaction mixture

was allowed to stir for 50 minutes and then transferred in a separating funnel filled with 200 ml of dichloromethane. The organic phase was washed with 2 l of Milli-Q water and dried for an hour with Na_2SO_4., The residue after solvent removal at 30C°, was redissolved in 5ml of dichloromethane and dropped in 50 ml of methanol to remove tetrabutylammonium bromide and the excess of thiol l. The brown precipitate M formed, was collected, washed repeatedly with methanol and redispersed in dichlorometane. The pale brown compound C that was observed to form owing to this operation was washed repeatedly with dichloromethane and desiccated on P_2O_5. A dark brown residue R was collected after solvent removal from the liquid phase. Both the products were desiccated on P_2O_5 and stored under inert atmosphere.

The reducing mixture was prepeared by gently adding *$NaBH_4$ (1,14g; 30 mmoles) to 45 ml of a LiCl(1,95g; 46 moles) dispersion in diglyme under nitrogen flux. The synthesis has been also repeated in ambient conditions (without nitrogen flux), but variations in the reaction product physicochemical properties were not detected with respect to those synthesized under nitrogen flux. All the products were desiccated on P_2O_5 and stored in protected ambient.

Synthesis of butane thiolate protected Cu nanoparticles (II method)

Cuprous bromide (280mg; 1,9 mmoles) and tetrabutylammonium bromide (680mg; 2,1 mmoles) were finely grinded in an agate mortar. The mixture was poured in 80 ml of dichlorometane. After 20 to 30 minutes the solubilization was completed and 20 ml of a 0,25 molar butanehiol solution in the same solvent were added in the flask. The reaction mixture was kept in nitrogen flux under continuous stirring for 30 minutes without precipitate formation. On dropping 20ml of a $NaBH_4$ 1 molar water solution in the reaction mixture, the copper-thiol adduct reduction took place. After three hours the organic phase was repeatedly washed with milli-Q water and dried on Na_2SO_4.

The residue after solvent removal at 30°C, was redissolved in 5ml of dichloromethane and dropped in 50 ml of methanol to remove tetrabutylammonium bromide and the excess of thiol. The brown precipitate M formed, was collected, washed repeatedly with methanol and redispersed in dichlorometane. The pale brown compound C that was observed to form owing to this operation was washed repeatedly with dichloromethane and desiccated on P_2O_5. A dark brown residue (R) was collected after solvent removal from the liquid phase. Both the products were desiccated on P_2O_5 and stored under inert atmosphere. The synthesis has been also repeated in ambient conditions (without nitrogen flux), but variations in the reaction product physicochemical properties were not detected with respect to those synthesized under nitrogen flux. All the products were desiccated on P_2O_5 and stored in protected ambient.

Synthesis of butane thiolate protected Cu nanoparticles (III method)

Copper(II) chloride dihydrate (664mg; 4,0 mmoli) tetrabutylammonium bromide (3,10g; 9,6 mmoles) and lithium bromide(684mg; 8,0 mmoles) were finely grinded in an agate mortar. The mixture was gently poured in 160 ml of dichlorometane. On adding 40 ml of a 0,22 molar butanethiolthiol solution in the same solvent, the reaction mixture changed from dark violet to colourless. The reaction mixture was kept in nitrogen flux under continuous stirring for 30 minutes without precipitate formation. On dropping 40ml of a $NaBH_4$ 1 molar water solution in the reaction mixture, the copper-thiol adduct reduction took place. After three hours the organic phase was repeatedly washed with milli-Q water and dried on Na_2SO_4. The residue after solvent removal at 30C°, was redissolved in 5ml of dichloromethane and dropped in 50 ml of methanol to remove tetrabutylammonium bromide and the excess of thiol. The brown precipitate M formed, was collected, washed repeatedly with methanol and redispersed in dichlorometane The pale brown compound C that was observed to form owing to this operation was washed repeatedly with dichloromethane and desiccated on P_2O_5. A dark brown residue (R) was collected after solvent removal from the liquid phase. Both the products were desiccated on P_2O_5 and stored under inert atmosphere. The synthesis has been also repeated in ambient conditions (without nitrogen flux), but variations in the reaction product physicochemical properties were not detected with respect to those synthesized under nitrogen flux. All the products were desiccated on P_2O_5 and stored in protected ambient.

Synthesis of 4-methylbenzenethiol protected Cu nanoparticles (I method)

Cuprous bromide (429 mg; 3,0mmoli) was solubilized by means of tetrabuthylammonium bromide TBABr (1,100g; 3,4 mmoli) in 120ml of tethrahydrofuran together with 960 μl(9 mmoles)of 4methylbenzenethiol. The formation of a precipitate was not observed. After ten minutes 45 ml of a LiCl-$NaBH_4$ diglyme suspension* was rapidly added to the reaction mixture under continuous stirring and nitrogen flux. The colour of the solution changed rapidly from pale yellow green to yellow orange and a white precipitate became to form. The reaction mixture was allowed to stir for 60 minutes and then transferred in a separating funnel filled with 200 ml of dichloromethane. The organic phase was washed with 2 l of Milli-Q water and dried for an hour with Na_2SO_4. A pale yellow crystalline solid was observed to form removing the solvent. It was collected, washed repeatedly with methanol and desiccated on P_2O_5.

*The reducing mixture was prepeared by gently adding $NaBH_4$ (1,14g; 30 mmoles) to 45 ml of a LiCl (1,95g; 46 moles) dispersion in diglyme under nitrogen flux. The synthesis has been also repeated in ambient conditions (without nitrogen flux) but variations in the reaction product

physicochemical properties were not detected with respect to those synthesized under nitrogen flux.

Synthesis of 4-methylbenzenethiol protected Cu nanoparticles (II method)

Cuprous bromide (280md; 1,95 mmoli) and tetrabutylammonium bromide were finely grinded in an agate mortar. The mixture was poured in 80 ml of dichlorometane. After 20 to 30 minutes the solubilization was completed and 20 ml of a 0,25 molar 4methylbenzenethiol solution in the same solvent were added in the flask. The reaction mixture was kept in nitrogen flux under continuous stirring for 30 minutes without precipitate formation. On dropping 20ml of a $NaBH_4$ 1 molar water solution in the reaction mixture, the copper-thiol adduct reduction took place. After three hours the organic phase was repeatedly washed with milli-Q water and dried on Na_2SO_4. The residue after solvent removal at 30°C, was redissolved in 5ml of dichloromethane and dropped in 50 ml of methanol to remove tetrabutylammonium bromide and the excess of thiol. A brown precipitate formed. It was collected, washed repeatedly with methanol and desiccated on P_2O_5. The synthesis has been also repeated in ambient conditions (without nitrogen flux) but variations in the reaction product physicochemical properties were not detected with respect to those synthesized under nitrogen flux.

Synthesis of 4-methylbenzenethiol protected Cu nanoparticles (III method)

Copper(II) chloride dihydrate (664mg; 4,0 mmoles) tetrabutylammonium bromide (3,10g; 9,6 mmoles) and lithium bromide(684mg; 8,0 mmoles) were finely grinded in an agate mortar. The mixture was gently poured in 160 ml of dichlorometane. On adding 40 ml of a 0,22 molar 4 methylbenzenethiol solution in the same solvent, the reaction mixture changed from dark violet to colourless. The reaction mixture was kept in nitrogen flux under continuous stirring for 30 minutes without precipitate formation. On dropping 40ml of a $NaBH_4$ 1 molar water solution in the reaction mixture, the copper-thiol adduct reduction took place. After three hours the organic phase was repeatedly washed with milli-Q water and dried on Na_2SO_4. The residue after solvent removal at 30°C, was redissolved in 5ml of dichloromethane and dropped in 50 ml of methanol to remove tetrabutylammonium bromide and the excess of thiol. A brown precipitate formed. It was collected, washed repeatedly with methanol and desiccated on P_2O_5. The synthesis has been also repeated in ambient conditions (without nitrogen flux), but variations in the reaction product physicochemical properties were not detected with respect to those synthesized under nitrogen flux.

Synthesis of phenol protected selenium nanoparticles (I method)

A suspension of selenous oxide (0,550g; 5 mmoles) in 25ml of formic acid was kept to boil by means of an oil bath under nitrogen flux.
The initially clear suspension of powdered selenous dioxide in formic acid turned to a dark grey-violet colour while a brown grey precipitate of crystalline selenium was observed to form according to the reaction reported below.

$$2HC(O)OH + SeO_2 \rightarrow 2CO_2 + Se^0 + H_2O$$

Heating was arrested after few minutes to limit the formation of dark brown crystalline selenium.
The reaction mixture was than allowed to cool at room temperature.
25 ml of a 0,1 molar solution of phenol in formic acid were added to the reaction mixture that was heated again and kept under reflux for an hour. The dark brown precipitate formed A, was separated by centrifugation at 5000 rpm from the liquid phase and repeatedly washed with formic acid, methanol and diethyl ether. The liquid phase was centrifuged at 8000 rpm for 20 minutes and dropped in water kept at 0°C. The dark brown precipitate B formed was repeatedly washed with water, lyophilized and dried on P_2O_5.
A water bath was also used to heat the SeO_2suspension in formic acid before and after the addition of phenol. A reaction temperature of 96°C was reached without reflux conditions. An increased amount of amorphous selenium was observed to form in this case.

Synthesis of phenol protected selenium nanoparticles (II method)
To increase the phenol protected selenium nanoparticles yield, selenous oxide and phenol in the same molar ratios of the former method were mixed at the same time in formic acid and the reaction mixture was kept to reflux for one hour under nitrogen flux. The dark brown precipitate formed A, was separated by centrifugation at 5000 rpm from the liquid phase and repeatedly washed with formic acid, methanol and diethyl ether. The liquid phase was centrifuged at 8000 rpm for 20 minutes and dropped in water kept at 0°C. The dark brown precipitate B formed was repeatedly washed with water, lyophilized and dried on P_2O_5.

Synthesis of phloroglucinol protected selenium nanoparticles
A phloroglucinol solution was obtained at room temperature dissolving phloroglucinol dehydrate (FLUKA 98%) in 50 ml of ethanol obtaining a 0,40 M concentration. Selenous acid solution was prepared dissolving Selenium dioxide (SeO_2 Aldrich 98%) previously finely hand-ground in 50 ml of Milli-Q water obtaining a 0,20 M concentration. These two solutions were mixed under stirring

in a 250 ml flask in N_2 atmosphere at 84 °C for one hour. The solution turned from colourless to pale yellow, to orange and finally to a persistent brown, indicating that the reaction (1) was complete. The solution was taken to reach room temperature and rotavapored up to ¼ of the initial volume. The orange-red precipitate, probably due to the reaction 2), was removed by centrifugation, repeatedly washed with Milli-Q distilled water, lyophilized, dried on P_2O_5 and stored for two months. No changes in the colour were noticed in aged samples.

$$nH_2SeO_3 \xrightarrow{C_6H_6O_3} Se_n(C_6H_5O_3)_m$$

Synthesys of 1 heptane protected Si nanoparticles

Silicon tetrachloride (92 μliters; 0,8 mmoles) along with of Tetrabutilammonium bromide (1,5 g; 2,70 mmoles) were solubilized in 100 ml of anhydrous toluene. 2ml of a 1molar $LiAlH_4$ solution in THF were added to the mixture that was allowed to stirr for three hours. After quenching the residual $LiAlH_4$ with 20ml of methanol, 100μl of a 0,1 M $H_2PtCl_6 \cdot 6H_2O$ solution along with 2ml of 1-heptene (14,2 mmoles) were added. After three hours of continuous stirring, the solvent was removed under vacuum conditions.

The residue was resolubilized in 20ml of hexane and sonicated for 20 minutes. The solution was filtered and washed with methylformammide (100ml) and milliq water.

Synthesis of Hydroxyapatite nanocrystals

Hydroxyapatite nanocrystals (HA) were prepared from an aqueous suspension of $Ca(OH)_2$ (1.35 M, 1 L) by slow addition of aqueous H_3PO_4 (1.26 M, 600 ml), at 95 °C. The reaction mixture was kept under stirring at 95 °C, for 24 hours, then stirring was suspended and the mixture left standing for 2 hours to allow deposition of the inorganic phase. This was isolated by filtration of the mother liquor, repeatedly washed with water and freeze-dried at -60 °C under vacuum (3 mbar) for 24 h.

In all the above syntheses, the nanocrystals powder fraction having granular dimensions ranging from 100 to 150 μm was selected for the study.

Synthesis of chrysothyle nanotubes

The chrysothyle nanotubes were synthesized according to a method devised in our laboratory [148] using amorphous silica aerosil 380, Magnesium chloride hexahydrate (Sigma Aldrich 99,0-102,02%), NaOH (Riedel de Haen 99%) and Milli-Q water.

The hydrothermal synthesis of chrysothyle nanotubes was performed by means of a 4382 Parr reactor equipped with a 300 ml T316SS steel vessel.

Namely a gel was obtained mixing amorphous silica (aerosil 380: 4,2730g; 0,07 moles) and Magnesium chloride hexahydrate (21,2636 g; 0,105 moles) in 60 ml of Milli-Q water. On adding 240 ml of a 0,70 molar solution of NaOH, the pH was increased up to 9,8 and adjusted at about 13 with 21 ml of a 5,1 molar solution of NaOH. The gel was left to stirr for 80 minutes and 200 ml of it were poured in the reactor vessel. The set out reaction temperature and the pressure reached were of 300 °C and 82 atm respectively. After about 24 hours the heating was stopped and the product allowed to cool at room temperature, was washed with milli-Q water and dried at about 120 °C with an IR lamp.

Chrysotile nanotubes filling method

The nanotubes (30 mg in 2 ml of dichloromethane) were kept under reduced pressure at 0°C and the solvent periodically reloaded. In the following step nanotubes were kept overnight at -20°C. The dichloromethane was then removed with a pipette and replaced with 2 ml of nanoparticle suspention to soak the nanotubes and replaced daily for a week. The solvent was then partially removed under vacuum conditions under reduced pressure and replaced with fresh nanoparticle suspension for two times. Finally the nanotubes were carefully washed with diclorometh ane and dried under inert atmosphere. All the nanoparticle suspension amounts used during the filling process were previously centrifugated at 8000 rpm for about 15 minutes.

In another experiment 4-methylbenzenethiol surface protected Silver nanoparticles were successfully used to fill the crysotyle nanotube hollows. In this case nanotubes were added to a dichloromethane filled shlenck tube and sonicated for 2 or 3 seconds repeatedly five or six times to break the molecoular membrane between the outer liquid phase and the empty nanotube cavity so allowing the solvent to occupy the hollows and at the same time to prevent the nanotube disruption due to the ultrasound effect. The nanotube suspension was stirred for one hour and preserved in dichloromethane.

4 ml of nanotube suspension were collected in a screw cap tube. The solvent was gently removed with a pipette after decantation and replaced with a freshly prepeared nanoparticle suspension previously centrifugated at 10000 rpm to remove possible nanoparticle clusters.

The tube content was gently sonicated again and kept to slowly stir for three days.

The liquid phase was carefully removed with a pipette after decantation and the nanotubes washed repeatedly with dichloromethane.

UV-vis absorption spectrophotometry

Optical spectra were recorded with λ6 and λ16 Perkin-Elmer spectrometers in a single beam mode using quartz cuvettes (1cm-path length) filled with metallic nanoparticles suspensions obtained diluting a centrifugated (8000 r. p. m. for 15 minutes) amount of a mother solution (see metallic nanoparticle synthesis section (paragraph)).

Transmission Electron Microscopy (TEM)

The TEM images were obtained with an electron transmission microscope JEM 2010 located at the Modena University C.I.G.S. (Centro Interdisciplinare Grandi Strumenti). The instrument was equipped with a GATAN 694 SLOW SCAN CCD camera and a LINK INCA 100 microanalysis device.

The sample was prepeared dispersing in Milli-Q water and sonicating for 60 seconds chrysothyle nanotubes previously grinded gently in an agate mortar. Droplets of the dispersion were allowed to evaporate on copper-chrome microgrids coated with a graphite layer. The sample was dried at room temperature or by means of an IR lamp.

An elemental analysis of the sample was carried out using energy dispersive spectroscopy (EDS) technics.

X-ray diffraction investigation

X-ray powder patterns were collected by means of a Philips 1050/81-PW1710 powder diffractometer. The instrument equipped with a graphite monochromator on the diffracted beam and a proportional counter, operated at a voltage and current intensity of 40 kV and 40 mA respectively generating a CuKα radiation with a λ of 1,541873 Å.

The steps were of 0,03° with a time per step of 1 second while the 2Θ range spanned from 10° to 80°. APD, PDF2 programs and Xpert software were used for the diffractogram visualisation and phase identification.

FT-IR Spectroscopy

The infrared spectra were recorded under nitrogen atmosphere from 4000 to 400 cm^{-1} with 2 cm^{-1} resolution using a NICOLET 210 FT-IR spectrometer. Other settings include an 8 mm aperture, 32 scans, velocity of 10 kHz, DLATGS detector and a 3-term Blackman-Harris apodization function. KBr pellets were prepared grinding chrisothyle nanotubes (1-2 mg) and FTIR grade KBR (300-350 mg) in an agate mortar. 100 mg of the solid mixture were pressed at 8 tons by means of a Spekak press.

Thermogravimetric and Differential scanning calorimetric analysis

Thermogravimetric (TGA) measurements were carried out using a ThermalAnalysis-SDT Q600 (TA Instruments, New Castle, DE, USA). Heating was performed in nitrogen flow (100 ml min^{-1}) using an alumina sample holder at a rate of 5 °C/min (10 °C/min in the DTA experiment) from room temperature to 1200 °C. The weight of the samples was approximately 10 mg.

Results and discussion

1) Surface protected metallic nanoparticles filling chrysotile nanotubes

The chrysothyle nanotubes were synthesized according to a method devised in our laboratory and described in the exsperimental section.

Morphological characterization

The morphological analysis of inorganic chrysothyle performed by TEM microscopy reveals the nanotubular nature of the reaction product.

Namely the several hundreds nanometers long nanocrystals present inner and external diameters of 7 and 21nm respectively and are caracterized by high structural and morphological uniformity (Fig.6 a, b).

A closer inspection of the synthetic chrysotyle TEM images reveals that the structure of the nanotube walls is made of about ten concentrical layers (Fig. 7).

An EDS (Energy Dispersive Spectroscopy) analysis performed by the same TEM microscope confirms the presence of only Mg, Si and O in the synthetic nanotubes according to the chrysothyle formula $Mg_3Si2O_5(OH)_4$ (Fig. 8).

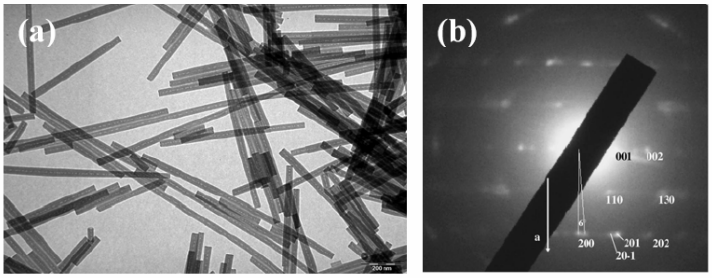

Fig. 6. a) TEM micrograph of the synthetic chrysotyle nanotubes. b) single tubular chrysotile nanocrystal electron diffraction pattern

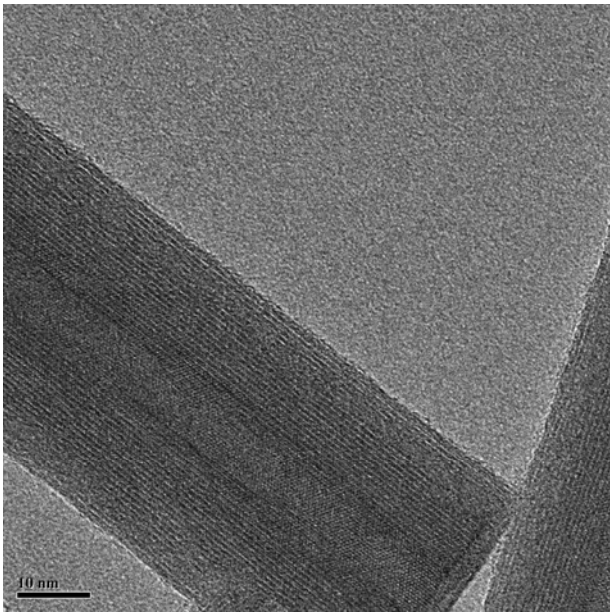

Fig. 7 TEM micrograph of a double wall synthetic chrysotyle nanotub

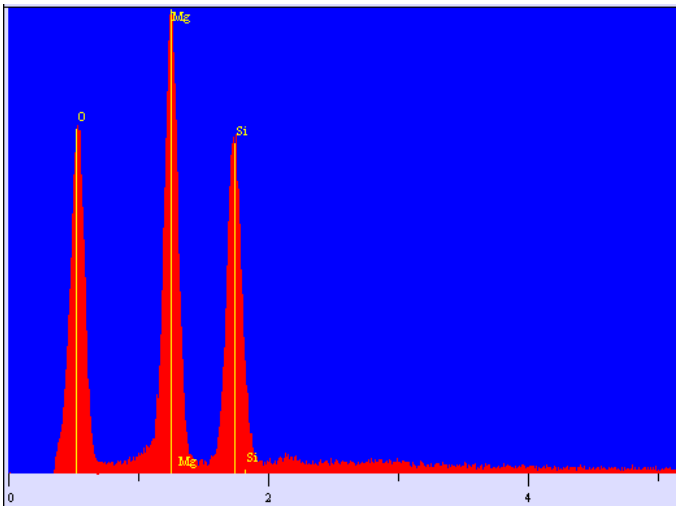

Figure 8. EDS (Energy Dispersive Spectroscopy) analysis confirming the chrysothyle formula $Mg_3Si_2O_5(OH)_4$ (Fig. 7).

X-ray diffraction investigation

The powder x-ray diffraction pattern of the synthesized chrysotile displays the characteristic reflections of high crystalline chrysotile, as unique crystalline phase (Fig. 9).

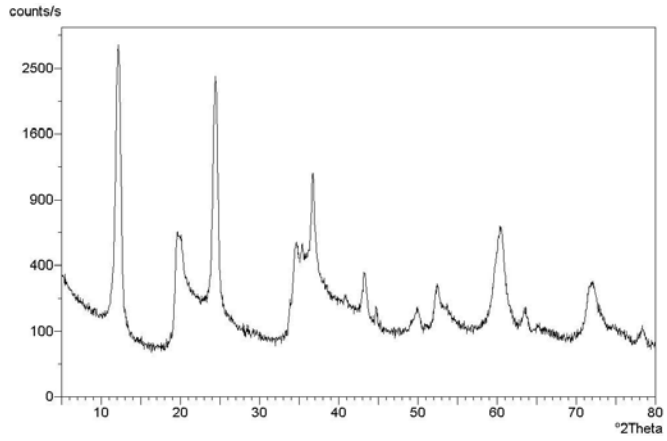

Fig. 9x-ray diffraction pattern of the synthesized chrysotile

An attempt was made to determine the cell parameters of the synthetic chrysothyle using the coordinates of an ideal trioctahedral OT unit in the unit cell with c=1.46 nm, space group *Cc,* as input for a Rietveld structure refinement in GSAS [153].

The refined unit cell parameters were a=0.5340(1) nm, b=0.9241(1) nm, c=1.4689(2) nm, β=93.66(3)°. Although the validity of the structure refinement is limited, the result is very useful because it proves that the refined pattern belongs to a pure chrysotile sample.

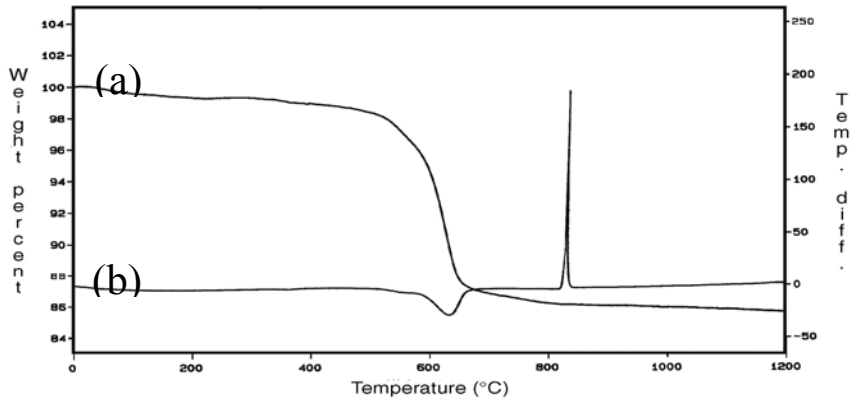

Fig. 10 TGA-DTA thermogram of the chrysothyle crystals

Thermogravimetric and Differential scanning calorimetric analysis

The TGA-DTA thermogram of the chrysothyle crystals show an endothermic area at 650°C corresponding to a dehydroxylation reaction and a sharp exothermic peak at 810°C which indicates the crystallization of the remaining amorphous anhydrous materials (the so-called meta-chrysotile $Mg_3Si_2O_7$) into forsterite (Mg_2SiO_4) (Fig. 10) [154].

Synthetic chrysotile crystals are of high omogeneity and purity as can be recognized from the lack of additional peaks (observed in the mineral chrysotile fibers thermal analyses) together with the sharpness of the transformation to forsterite and silica.

FT-IR analysis

The FTIR spectrum of the synthetic chrysotile nanocrystals is reported in Fig. 11.

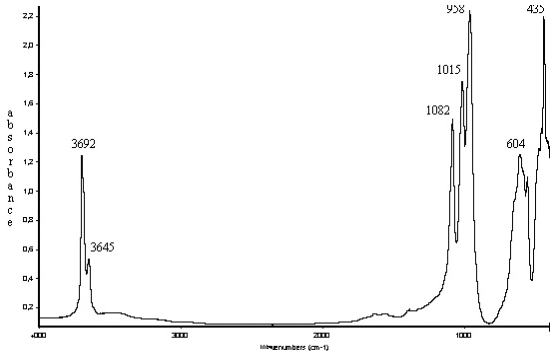

Figure 11 FTIR absorption spectrum of synthetic chrysotile fibers in the range 4000-400 cm^{-1}. The main absorption peaks are marked.

The main band frequencies listed in Table 1 agree with the literature data and confirm the absence of other phases.

FTIR cm^{-1}	Assignment	Assignment
3692	MgOH stretch	external MgOH stretch
3645 (shoulder)	MgOH stretch	internal MgOH stretch
3410 (broad)	H_2O stretch	antisymm. Si-O-Si stretch
1640 (broad)	H_2O bend	symm. translation mode Si-O
1082	Si-O-Si stretch	Mg-OH symm.translation mode Mg-O symm. mode
1015	Si-O-Mg stretch	
958	Si-O stretch	
604	Mg-OH libration	Mg-O antisymmetric mode
435	Si-O-Mg bend	

Table 1 Assignment of the chrysotile FTIR and Raman bands.

Characerization of metallic nanoparticles used to fill the chrysotile nanotubes

The optical absorption spectra of the synthesized decanethiol capped Au, Ag and Au-Ag alloy nanoparticles dispersed in dichloromethane were recorded in the wavelength range of 250-700 nm and reported in Fig. 12. The spectra show an intense surface plasmon (SP) absorption band whose peak maximum position is directly related to the Au/Ag ratio in the nanoparticle core.

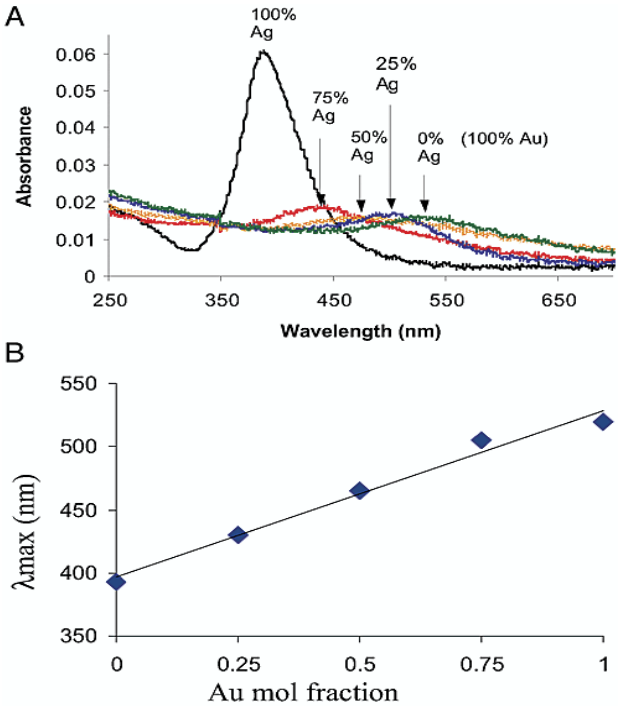

Fig. 12 Optical absorption spectrum, recorded in the 250-700 nm wavelength range, of synthesized decanethiol capped Au, Ag, Au4Ag1, Au1Ag4 nanoparticles.

Peak maxima at about 400 and 540 nanometers appear in the Gold and silver decanethiole surface protected nanoparticles respectively.

The maxima of the alloy clusters fall between and a red shift of the peaks with increased Au content is noted according with the literature data.

The position of the absorption maximum also depends on the nature of the molecules forming the monomolecular layer on the nanoparticle surface as can be seen comparing the absorption maximum positions in the spectra of the silver nanoparticles coated with decilmercaptane (about 400nm) (Fig.12) and buthilmercaptane (450nm) Fig13.

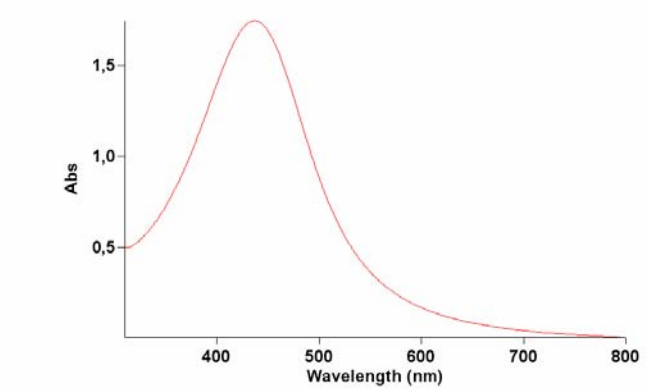

Fig13 Optical spectrum of butilmercaptane capped silver nanoparticles

A well defined absorption maximum is associated to a high degree of monodispersion for Au, Ag and AuAg alloy nanoparticles. This feature is prerequisite for the formation of ordered nanoparticle arrays filling the nanotube hollows and consequently for all their optical and electrical properties. For comparative purpose we report in fig 14 the optical spectrum of

Cisteine coated polidispersed Au nanoparticles synthesized in a one phase method as reported in literature.

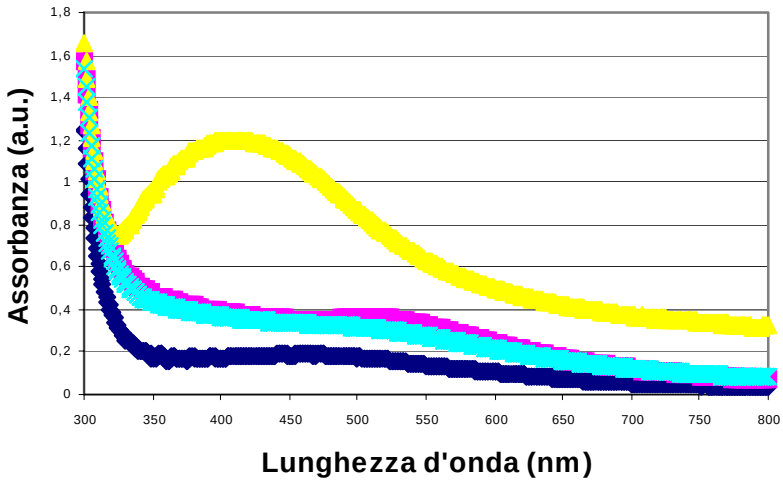

Fig.14 Optical spectra of cisteine capped Ag, Au, Au-Ag alloy capped nanoparticles (Ag: yellow; Au1/Ag4: blue; Au4/Ag1: light blue; Au: pink).

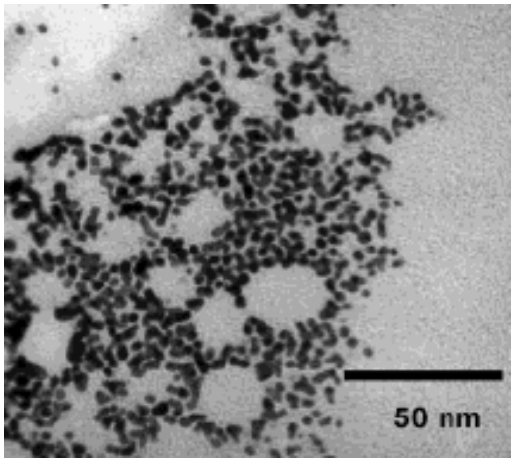

Fig. 15 TEM image of polydispersd cisterne capped Au nanoparticles

The morphology of the thiol surface protected metallic and bimetallic nanoparticles synthesized as reported in experimental section, has been investigated by TEM microscopy. The samples were prepared evaporating small drops of a particle dispersion in booth ethanol or water on a carbon coated copper grid.

In Fig. (16) is reported the TEM micrograph of the decilmercaptane surface coated Au4/Ag1 particles These reveal an approximately spherical shape of about 2 nm in diameter.

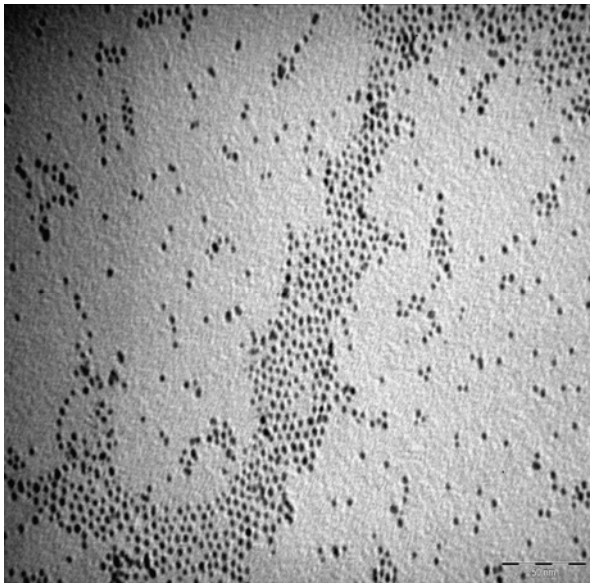

Fig. 16 TEM micrograph of the decilmercaptane surface coated Au4/Ag1 particles

FT-IR Analysis

The FT-IR ATR absorption patterns of decilmercaptane surface protected Au4/Ag1 and buthilmercaptane surface protected Ag nanoparticles are reported in Fig. (17 a,b). These patterns show the typical absorption bands due to the alkilic chains surrounding the nanoparticle surface. Namely sharp and strong absorptions attributed to the symmetrical and asymmetrical stretching modes of the C—H bonds, can be found in the 3000—2800 cm^{-1} region. Bending and rocking vibrational modes of the C—H, C—C are responsible of the bands below 1500cm^{-1}.

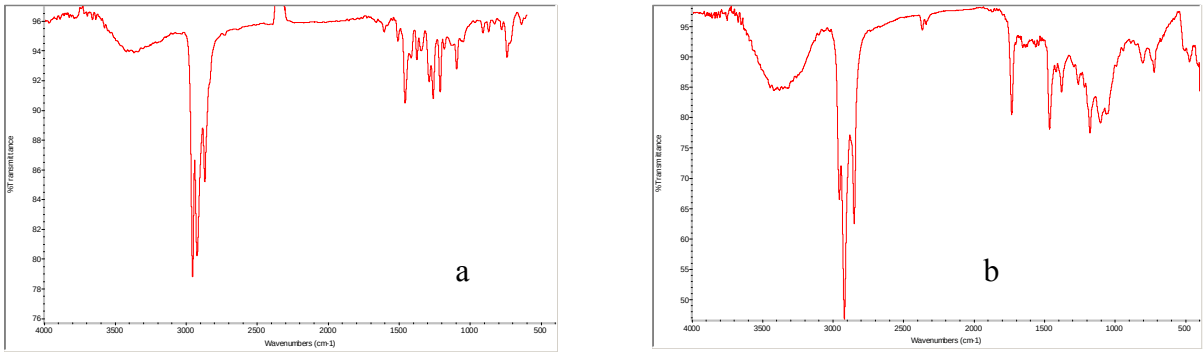

Fig. 17 FT-IR ATR absorption patterns of decilmercaptane surface protected Au4/Ag1 (a) and buthilmercaptane surface protected Ag nanoparticles (b)

Synthetic chrysotyle nanotubes filled with the previously prepared nanoparticles

In Fig. (18) is reported the TEM micrograph of the synthetic chrysotyle nanotubes partially filled with the above mentioned nanoparticles.

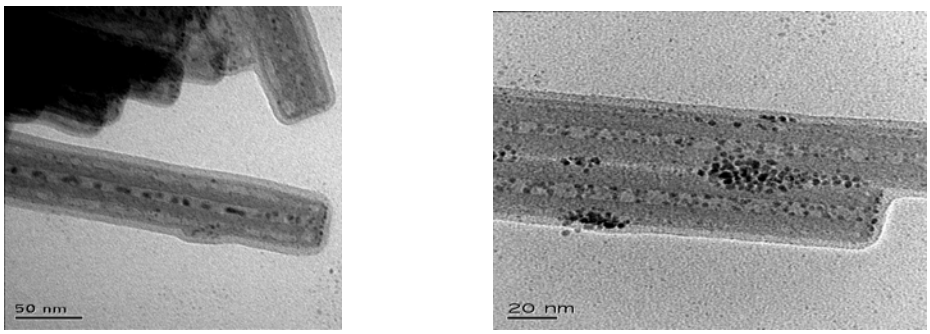

Fig. 18. TEM micrograph of the synthetic chrysotyle nanotubes partially filled with decanethiol coated Au4/Ag1 nanoparticles.

Synthetic crysotyle nanotubes were also filled with buthanethiole Surface coated silver nanoparticles with dimensions ranging between 2-3 nm (Fig. 19). And with 4-methylbenzenethiol surface coated silver nanoparticles (Fig 20)

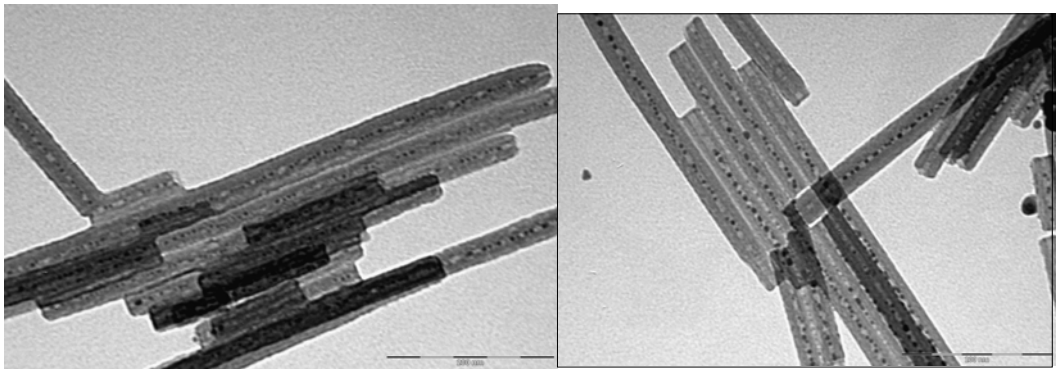

Fig. 19 TEM micrograph of butanethiol protected Ag nanoparticles partially filling synthetic chrysothyle hollows

Synthetic chrysotyle nanotubes filled also with 4-methylbenzenethiol protected silver nanoclustersare are reported in Fig. 20.

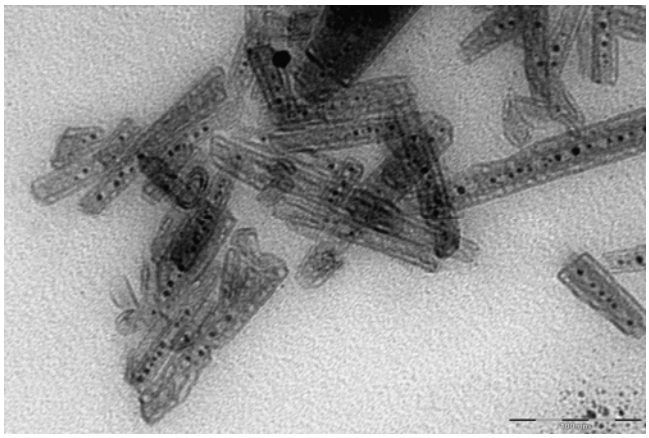

Fig. 20 TEM micrograph of 4-methylbenzenethiol protected Ag nanoparticles partially filling synthetic chrysothyle hollows.

In many cases, nanoparticles filling the nanotubes appear fused forming clusters separated each other by gaps probably because of gas bubbles due to the decomposition of the molecules on the nanoparticle surface during the morphology characterization by TEM.

The choose of the experimental conditions in the filling process was devoted to the nanotube integrity preservation.

Aprotic solvents were used to soak nanotubes instead of protic ones that in many cases decompose the octahedral magnesium hydroxide layer coating the external nanotube walls.

Hexane diethylether and tethrahydrofurane were discarded because nanoparticles tend to form clusters together greater in size than nanotube hollows in these solvents. Thetrahydrofuran particularly weakens the nanotube walls that are so easily disrupted under the electron beam of the

microscope. Chloroform and dichlorometane were successfully used in the filling process but the first one was discarded due to its toxicity.

The nanotubes were at first kept in dichloromethane at -10°C and under reduced pressure conditions to remove gases into the cavities and to fill them with solvent by capillarity action. The nanoparticles were then forced into the hollows by diffusion and convection as described in the experimental section. Nanoparticle suspension wetting the cavity walls was periodically renewed to prevent the irreversible nanoparticle clusters formation. Nanotubes were also successfully filled with 4 methilbenzenethiol protected silver nanoparticles. In this case dichloromethane was allowed to fill the cavities simply breaking the molecoular membranes at the tube ends by means of ultrasounds used carefully to avoid the nanotube disruption. The soaked nanotubes were then kept in contact with a freshly prepeared nanoparticle dispersion in dichloromethane and the mixture was gently stirred so allowing the nanoparticles to fill the hollows by both convection and diffusion and at the same time avoiding the formation of clusters.

Decanethiol capped Au4/Ag1 nanoparticles filled successfully the nanotube hollows probably owing to the formation of ordered arrays in the cavities by means of Van der Vaals interactions between interpenetrating alkyl chains on adjacent nanoparticles but gave irreversible cluster formation on the outer nanotube wall.

Buthanethiol and 4 methylbenzenethiol capped silver nanoparticles (BCN) were used as filling material in order to get Charge transfer by tunnel effect between their neighbouring metallic cores poorly protected by short buthilic chains. Moreover the observed fusion of these nanoparticles in the nanochristal hollows is due to the same reason.

In conclusion geoinspired synthetic $Mg_3Si_2O5(OH)_4$ nanotubes, which have similar radial dimensions as multiwalled carbon nanotubes (e.g., 7 nm and about 20 nm of inner and outer diameter respectively) are considerably longer (up to a few millimeters) than carbon nanotubes and are constituted of an insulating material. These characteristic features make synthetic chrysotile nanotubes excellent candidates to prepare innovative inorganic nanowires.

The proved nontoxicity of stoichiometric synthetic chrysotile nanotubes allows their application in industrial fields without impediments for human health. They could exhibit strong quantum-size effects in optical nonlinearity, in lightharvesting systems, optoelectronics, and photonics.

Synthetic $Mg_3Si_2O_5(OH)_4$ nanotubes do not form densely packed bundles such as mineral chrysotile fibers.

Moreover, geoinspired $Mg_3Si_2O_5(OH)_4$ nanotubes possess the high advantage that they can be synthesized modulating their wall thickness dimensions (7, 14, 21, 8, 35 nm), correspondent to multiple of OT sheets, each 7 nm thick.

Stoichiometric synthetic chrysotile nanotubes have been partially filled with bi and monometallic highly monodispersed nanoparticles with diameters ranging from 1,7 to 5,5 nm depending on the core composition (Au, Au4/Ag1, Au1/Ag4, Ag). In the case of 4 methylbenzenethiol protected silver nanoparticles, the filling was carried out by convection and capillarity effect at room temperature and pressure using a suitable organic solvent (Fig. 17(b)).

2)Biomimetic hydroxyapatite nanocrystals as carriers for Au/Ag alloy anticancer particles

Characterization of HA nanocrystals.

HA nanocrystals were synthesized according to the above described method. Powder X-ray diffraction patterns (Figure 21 a) showed characteristic diffraction maxima of hydroxyapatite single phase (JCPDS 9-432).

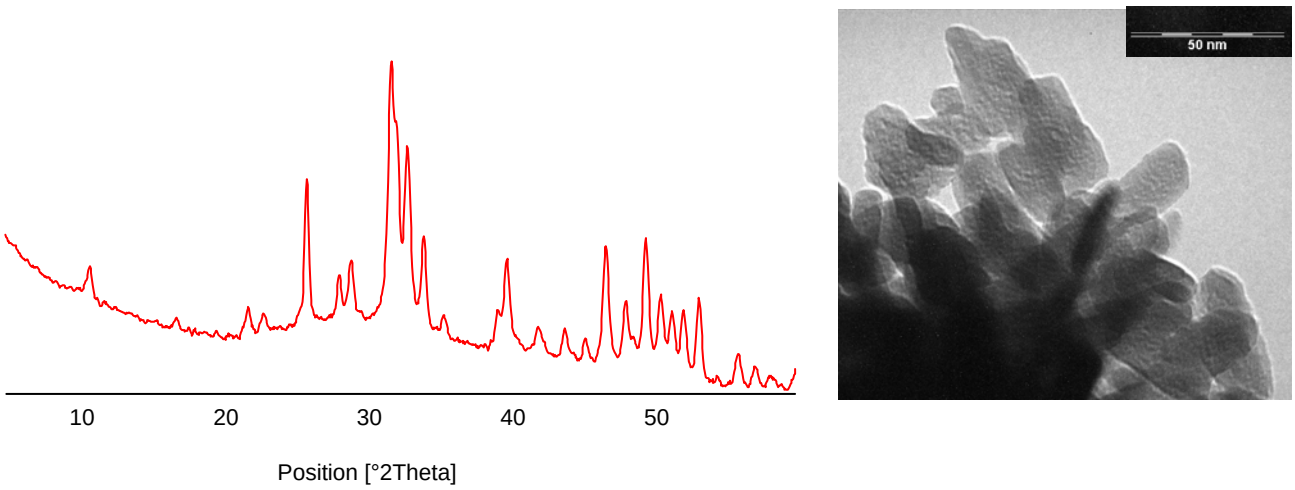

Fig. 21. X-ray diffraction patterns of synthesized HA nanocrystals (a), and Transmission electron microscopy (TEM) image. Scale bars is 100 nm

The degree of crystallinity was quantified according to previous method (Table 1). The crystal domain sizes along the *c*-axis and along a perpendicular to it, were calculated by the Scherrer's formula (see experimental section) using the 2θ = 26° (002) and 2θ = 39° (310) diffraction peaks respectively (Table 1). The surface Ca/P ratio determined by X-ray photoemission spectroscopy (XPS) analysis was significantly lower than the bulk Ca/P ratio as a result of nanocrystalline apatite surface disorder.

Table 1. Chemical and structural parameters of the synthetic HA nanocrystals.

	Degree of crystallinity	D_{002} (nm)	D_{310} (nm)	Length dimensions TEM (nm)	Surface area (m^2/g)	Bulk Ca/P (XPS)	Surface Ca/P (ICP-OES)
HAhc	79 % ± 3	50 ± 7	23 ± 3	80 ± 10	60 ± 6	1.65 ± 0.05	1.30 ± 0.05

HA transmission electron microscopy (TEM) images revealed the presence of plate-like nanocrystals clusters (length 80 ± 10 respectively) (Figure 1,b).

Characterization of Au/Ag nanoparticles

The 11 –mercapto-undecanoic acid (MUDA) surface protected Au_4Ag_1 nano-particles have been obtained by an exchange reaction. MUDA capped nano-particles have been collected by centrifugation and re-dispersed in aqueous media so that an alloy colloidal suspension (1,4 mg/ml Au; 0,18 mg/ml Ag; pH=8,6) have been obtained and selected for the study. The Au/Ag alloy nanoparticles suspension had a 4,1 Au/Ag molar ratio. The colloid showed high stability at a pH ranging from neutral to slightly basic (8,6) and no sedimentation has been observed even after 2 years. The stability could be ascribed to the negative charges of the coated nanoparticles as documented by their low zeta potential at pH=8,6 (ca. -56 mV).

TEM analysis indicates that dried, mercapto-undecanoic acid covered nano-particles showed a rather narrow size distribution (Fig. 22a). The diameter Gaussian distribution of Au-Ag nanoparticles was centred at 6.5± 1,6 nm, while the minimum diameter measured 1,6 nm and the maximum 8,6. Consistently with their dimensions Au-Ag nanoparticles presented a 525 nm UV absorption maxima (Fig. 22b).

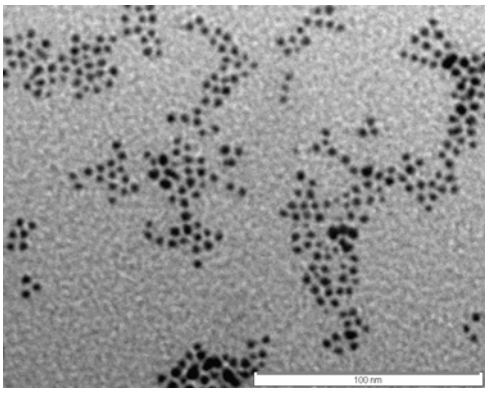

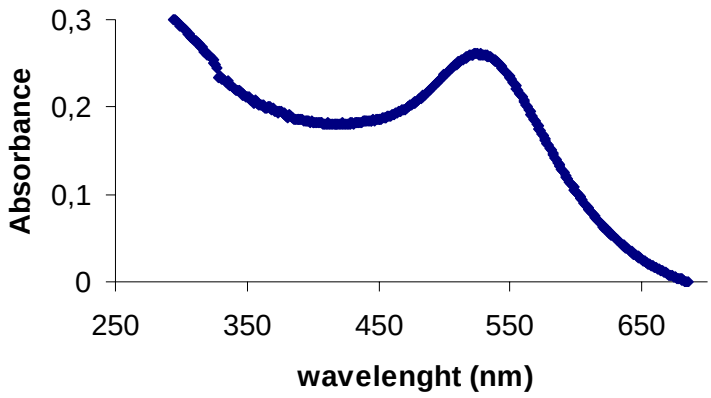

Fig.22 a) Assembly of metal nanoparticles onto HA nar
as a proof of the nanoparticles high monodispersion degree

The sequence of TEM micrographs reported in Fig. 23 confirms that 11 mercaptoundecanoic surface protected Au4/Ag1 nanoparticles feature a strong affinity for hydroxyapatite

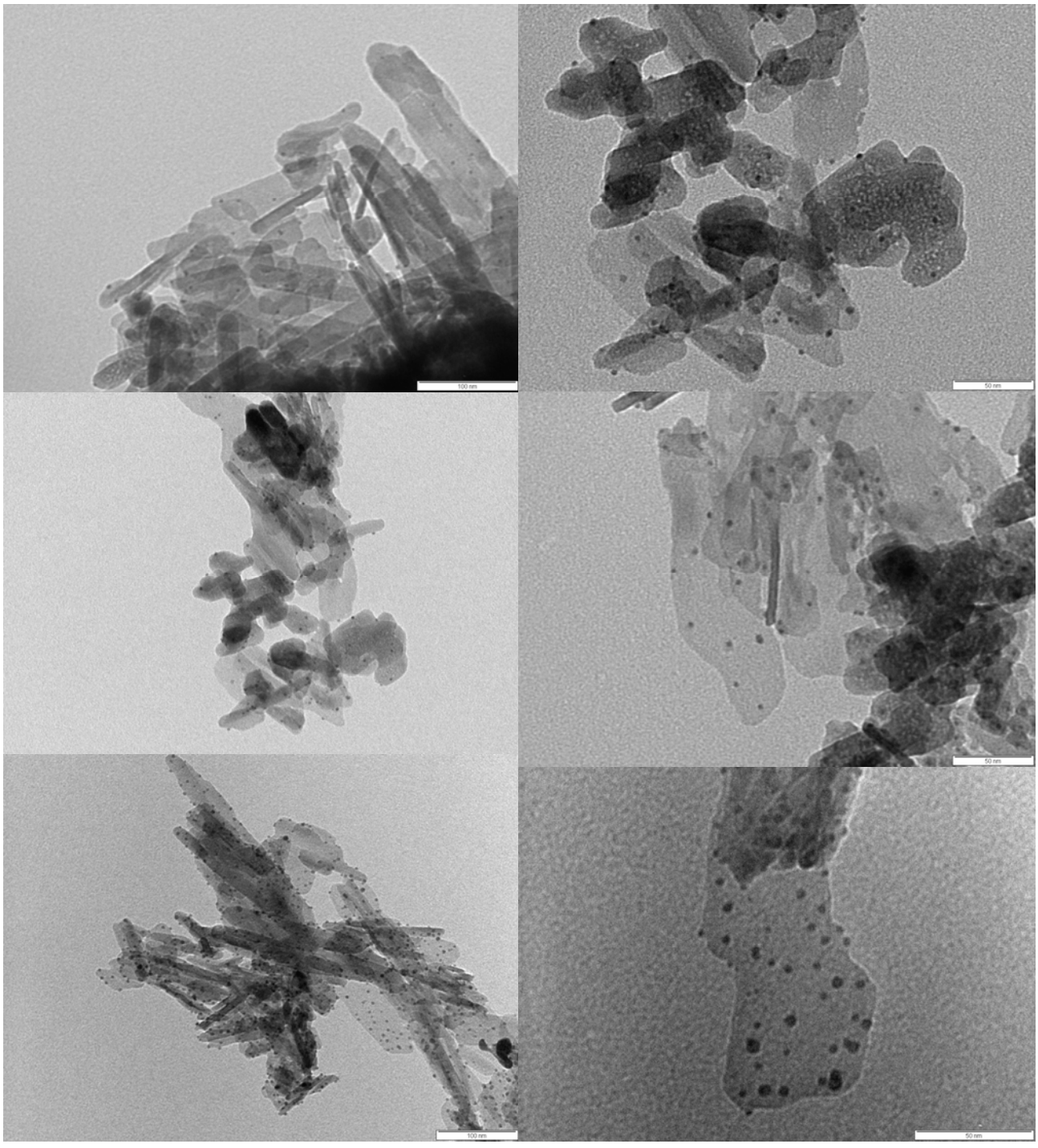

Fig. 23 11 mercaptoundecanoic surface protected Au4/Ag1 nanoparticles adsorbed on nanometric apathyte crystals

In conclusion we have successfully prepared an anticancer nanoparticles deliver system utilizing

biomimetic hydroxyapatyte nanocrystals as biomimetic deliver agents.

3) Cuprous bromide nanocrystals

Cuprous Bromide nanocrystals has been obtained like a white precipitate (sometimes pale yellow) as previously reported in the exsperimental section. It was separated by centrifugation at 3000 rpm, washed with water, methanol and finally with diethylether and after dryng under vacuum it was stored in a dessiccator.

Morphological analysis

Nanocrystals of about spherical shape and diameters of about 20 nanometers surrounding large crystals of irregular boundaries and sizes of about 100 nanometers appear in the micrograph reported in Fig. 24.

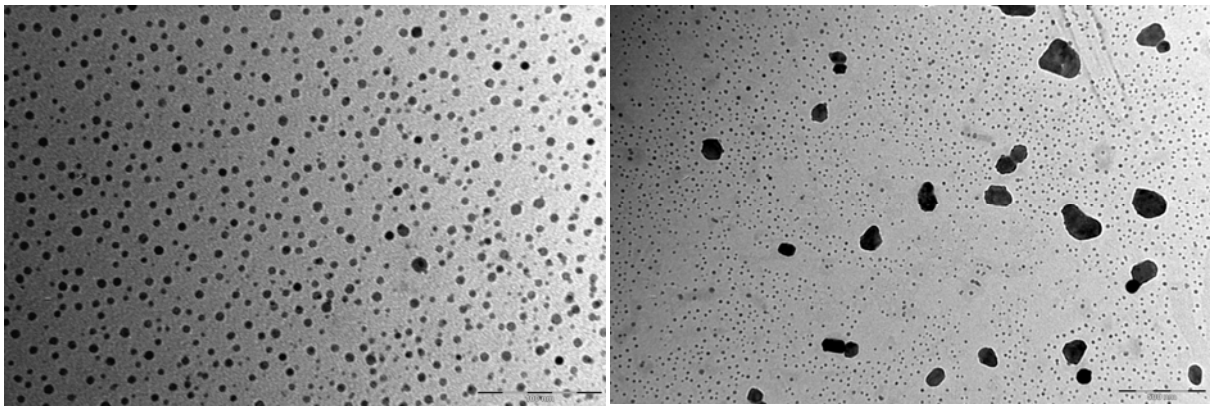

Fig. 24 TEM micrograph of cuprous bromide nanocrystals with different morphologies

X Ray Diffractometric analysis

The diffraction pattern (Fig.25) of the obtained product shows peaks that can be indexed to the (1 1 1), (2 2 0), (3 1 1) and (3 3 1) crystal planes of cubic CuBr.

The calculated lattice constant of the resultant product is 5,68 Å. It was calculated from ICSD using POWD-12++, (1997).

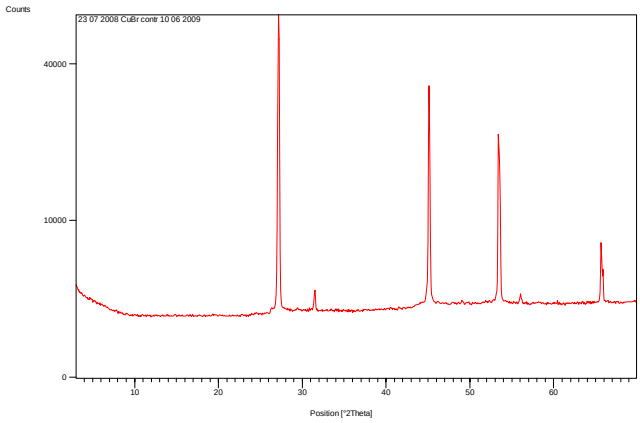

Fig. 25 X-ray diffraction pattern of cubic cell copper(I) bromide nanocrystals

In conclusion a semiconducting copper(I) bromide nanocrystals were synthetized with a diameter of about 20 nanometers according to a new sybthetic method.

4) Butanethiolate protected copper nanoparticles

Butane thiolate protected Cu nanoparticles have been synthetized according to the three different syntesys methods reported in the exsperimental section.

UV-vis absorption spectrophotometry

The samples for the optical studies were prepared dispersing in dichloromethane (10ml) 3-4 mg of the dark brown residue R (see description of the syntheses). The dispersion was centrifugated at 8000 rpm and diluted 1/5 with the same solvent in a quartz cuvette (1cm-path length).

Transmission Electron Microscopy (TEM)

The samples for the TEM investigations were prepared dispersing in ethanol (water)

a) the dark brown precipitate M from methanol,
b) the dark brown residue R.

c) The crystalline pale brow compound C.

The dispersions were dropped on the graphite layer coating the TEM grids and the solvent was allowed to evaporate.

FT-IR Spectroscopy

The samples for the FT-IR analysis were prepared finely grinding in an agate mortar 200 mg of KBr mixed with 2mg of:

a) the dark brown precipitate M from methanol,
b) the dark brown residue R .
c) The crystalline pale brow compound C.

X-ray diffraction investigation

The samples for the DRX analysis were prepared using the front loading of standard quartz sample holders which are 1 mm deep, 20 mm high and 15 mm wide.

As can be found comparing the diffractometric and FTIR data the same products were obtained with the three synthetic routes (Figs. 26 and 27): namely the brown precipitate M from methanol is a mixture of butanethiolate protected copper nanoparticles (R) with a crystalline compound C (Figs. 28, 29 and 30).

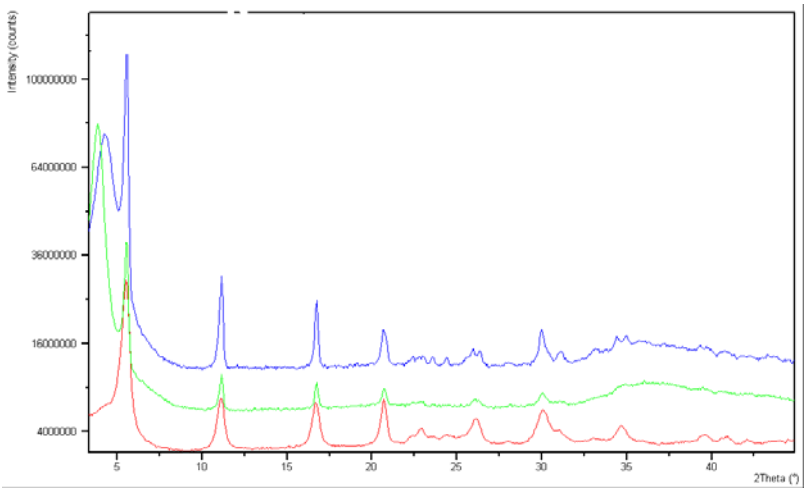

Fig. 26 From the top X-ray diffraction pattern of the brown precipitate M obtained with the 3, 1 and 2 synthesis routes

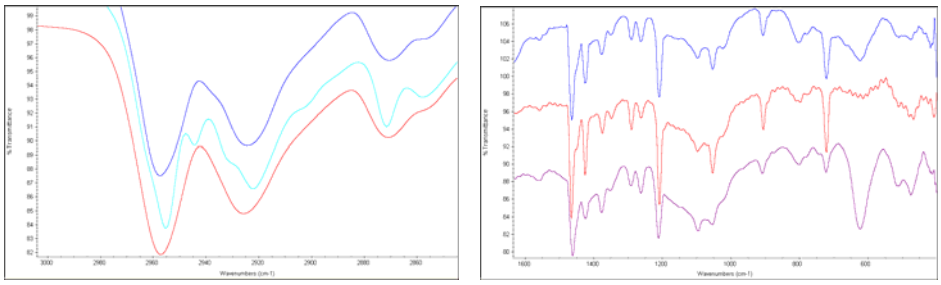

Fig. 27 FT-IR spectra of the brown precipitate M obtained with the 2, 1 and 3 synthesis routes from the top

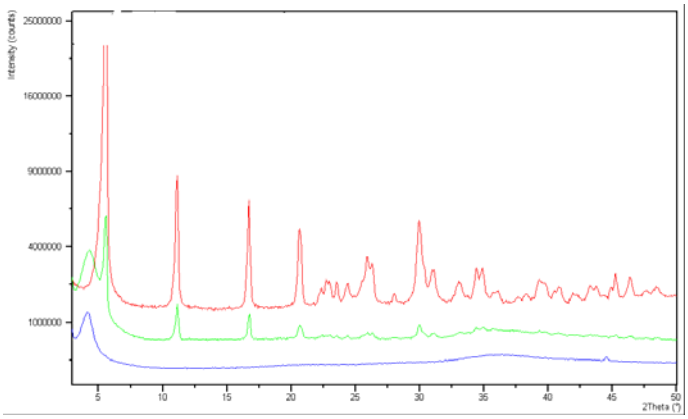

Fig.28 From the top, X-ray diffraction pattern of the layered copper butanethiolate C, the brown precipitate M, the butanethiolate protected copper nanoparticles R and

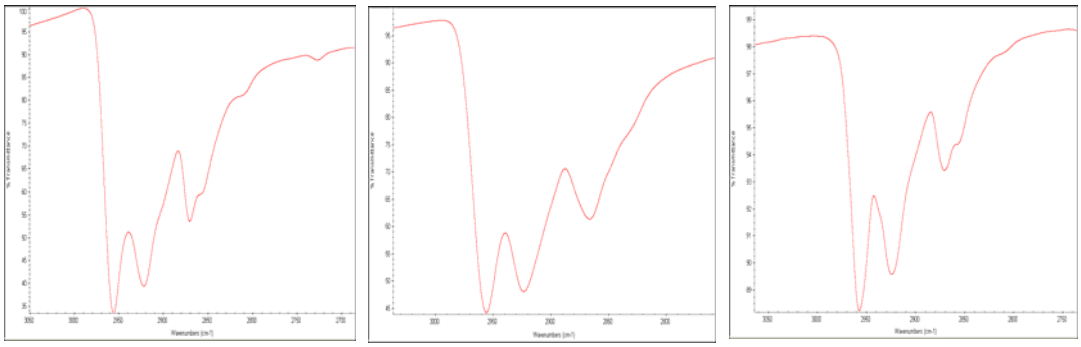

1 2 3

Fig. 29 FT-IR spectra in the range 2800-3000cm-1 of the crystalline compound C(1), of the butanethiolate protected copper nanoclusters(2) and of the precipitate M (3)

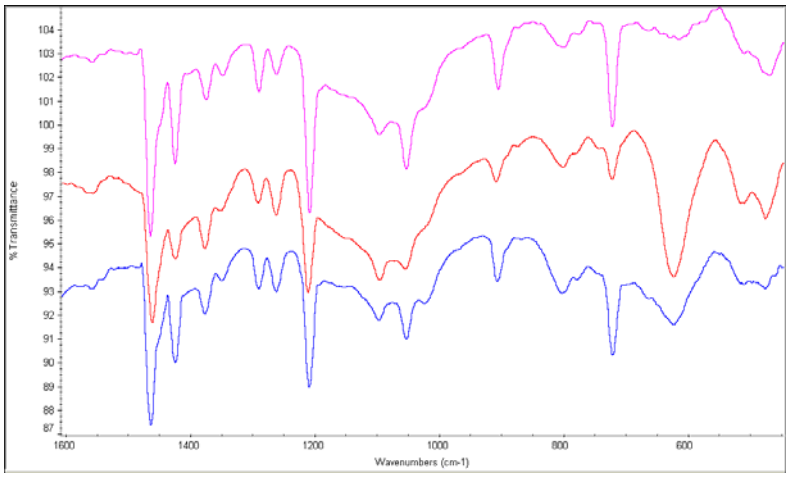

Fig.30 FT-IR spectra of the crystalline compound C, of the copper nanoparticles B and of the brown compound precipitating from methanol A.

Morphological analysis

The morphology of the reaction products was investgated by TEM microscopy.

Differences in morphology and stability of the products were found in the TEM micrographs depending on the synthetic method and on the medium used to disperse the sample.

The isolated crystalline compound C could not be detected by TEM microscopy for all the syntheses investigated.

Synthesis route 1 (Dispersing medium: Ethanol)

Precipitate M

Nanoparticles rapidly decomposing under the electron beam of the microscope and leaving nanocrystals of about 25 nanometers in size were observed (Fig 31).

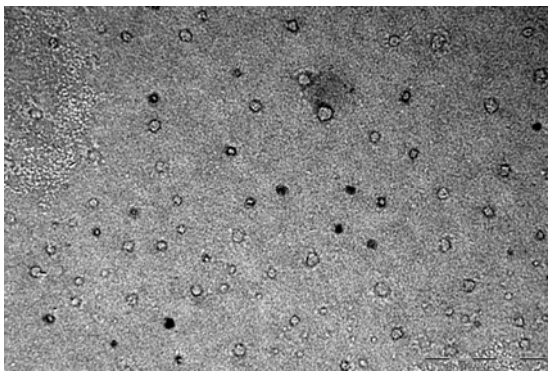

Fig.31 TEM micrograph of the brown precipitate M from synthesis route 1. Methanol was used as dispersing medium

Synthesis route II

Butanethiolate protected copper nanoparticles R

Stable butanethiolate protected copper nanoparticles with sizes ranging from 1 to 2 nm were observed both isolated and forming small clusters (Fig. 32).

Butanethiolate protected copper nanoparticles are too small to be easily detected by TEM microscopy and become more visible as they form clusters that appear as black spots of variable sizes and shapes in the TEM micrograph.

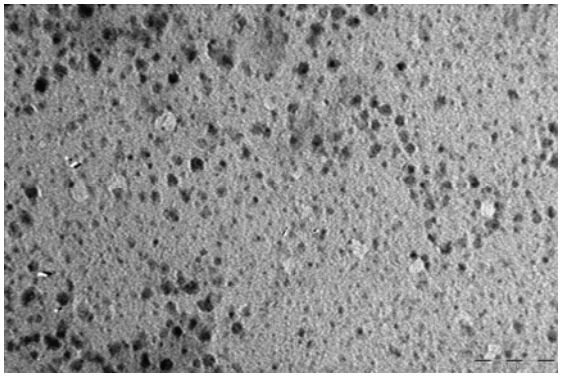

Fig. 32 TEM micrograph of the butanethiolate protected copper nanopatrticles obtained with synthesis route 2. Ethanol was used as dispersing medium

Precipitate M

Stable nanoparticles (or small nanoparticle clusters) of about spherical shape with an average diameter of 3,5 nanometers and an high degree of monodispersion appeared along with few large nanoparticle clusters Fig. 33.

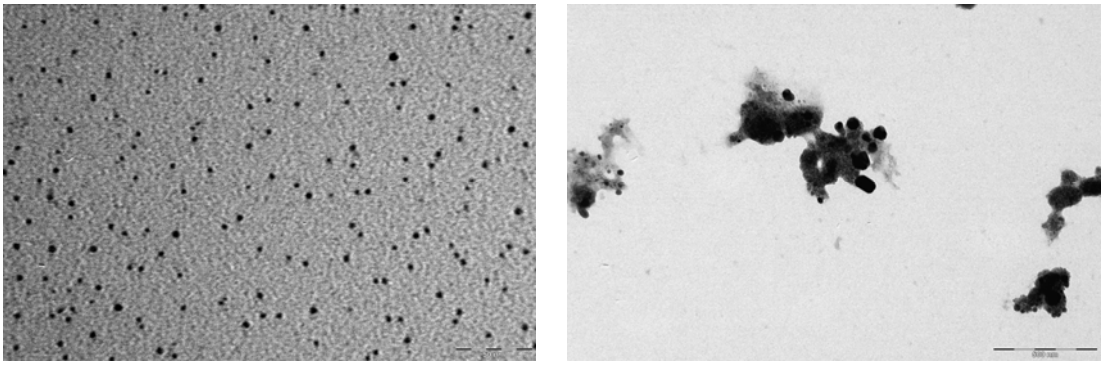

Fig. 33 TEM micrographs of the brown precipitate M from synthesis route 2. ethanol was used as dispersing medium

Synthesis route III

Precipitate M

Spherical Nanoparticles with diameters ranging from 20 to 50 nanometers and decreasing in size under the electron beam were observed (fig 34).

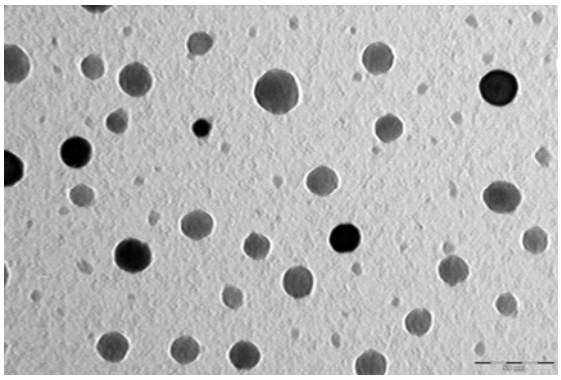

Fig. 34 TEM micrograph of the brown precipitate M from synthesis route 3. Methanol was used as dispersing medium.

Synthesis route 2(Dispersing medium: Water)

Precipitate M

Clusters of stabile nanoparticles of about 10 nm in size were observed. (fig 35)

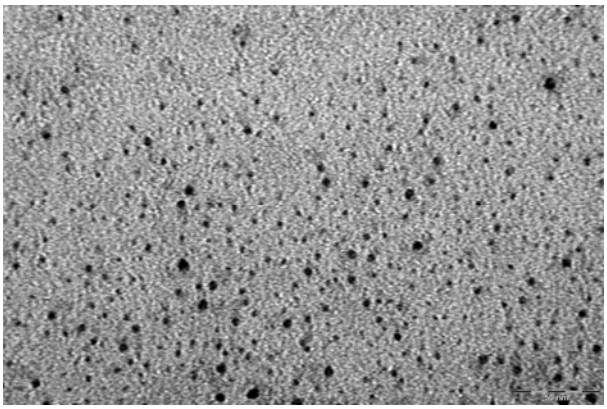

Fig.35 TEM micrograph of the brown precipitate M from synthesis route 2. Water was used as dispersing medium.

Butanethiolate protected copper nanoparticles R

Nanoparticles of about 2nm average diameter and nanoparticle clusters with size of about 10 nanometers were observed along with spherical microparticles of about 100 nm in diameter

(Fig. 36). A similar behaviour was found also by Chen and Sommers [66]. These authors ascribed this finding to the formation of nanoparticle bilayer structures where the top layer sits at the 2-fold saddle sites between neighboring particles.

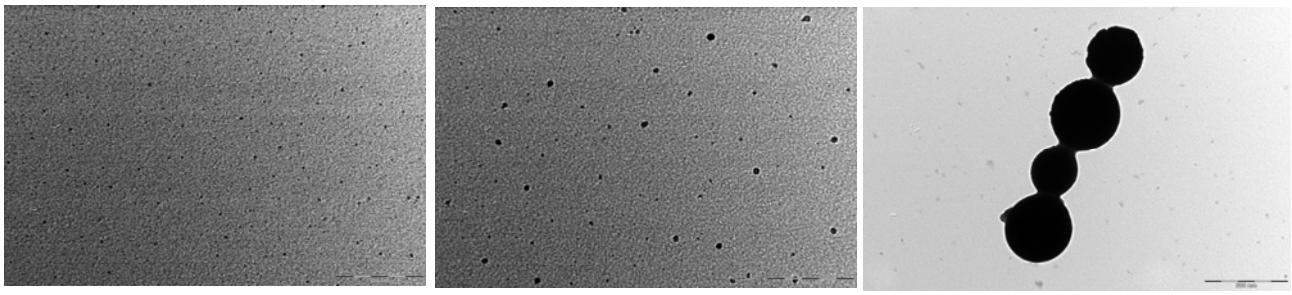

Fig.36 TEM micrographs of butanethiolate protected copper nanoparticles synyhesized with method 2. Water was used as dispersing medium.

Synthesis route III

Precipitate M

Large nanoparticles of spherical shape and sizes ranging from 20 to 50 nanometers were observed to disappear under the electron beam forming small low density nanocrystals with irregoular boundaries and sizes ranging from 10 to 20 nanometers (Fig. 14).

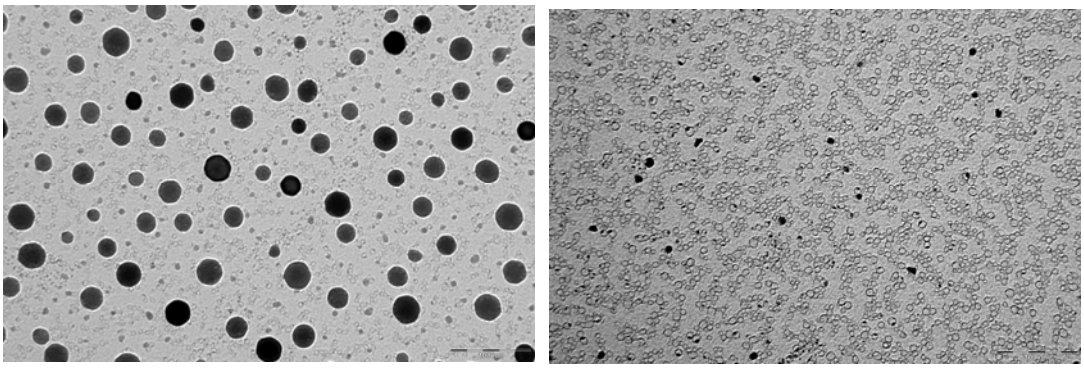

a b

Fig.37 TEM micrograph of the brown precipitate M from synthesis route 3 before (a) and after (b) the decomposition due to the electron beam. Water was used as dispersing medium.

As can be deduced from TEM data, the morphologies of the reaction product, namely copper nanoparticles or layered copper thiolates depends

a) on the physicochemical conditions during the synthesis.
b) on the dispersing medium used to prepare the sample.

Synthesis method II allows to obtain stable nanoparticles of 1 to 2 nanometers in size both isolated and forming clusters. Nanoparticle cluster formation was enhanced as water was used as dispersing medium probably due to the idrophobic nature of the butanethiolate layers coating the nanoparticle surface. Methods I and III lead to large unstable spherical nanoparticles with sizes ranging between 20 to 50 nanometers rapidely disappearing during the TEM experiment. These nanoparticles appeared in the TEM micrograph independently on the dispersing medium used in the sample preparation. This findings allows to conclude that stability and dimensions of the copper nanoparticles are inversely related.

Optical Absorption studies

The UV visible pattern of the butanethiolate protected copper nanoparticles redispersed in dichlorometane was the same for all the three syntheses and revealed a Mie scattering trend typical of thiol surface protected metallic nanoparticles (Fig. 38). However a plasmon resonance absorption maximum didn't appear in the nanoparticle spectrum. This behaviour also found by Chen and Sommers for hexanethiolate protected copper nanoparticles synthesized with a one phase method, was ascribed to the size of the nanoparticles with average diameter of 2 nanometers [66]. The plasmon resonance absorption maximum at 570nm was observed only in the spectrum of copper nanoparticles more than 4nm in size.

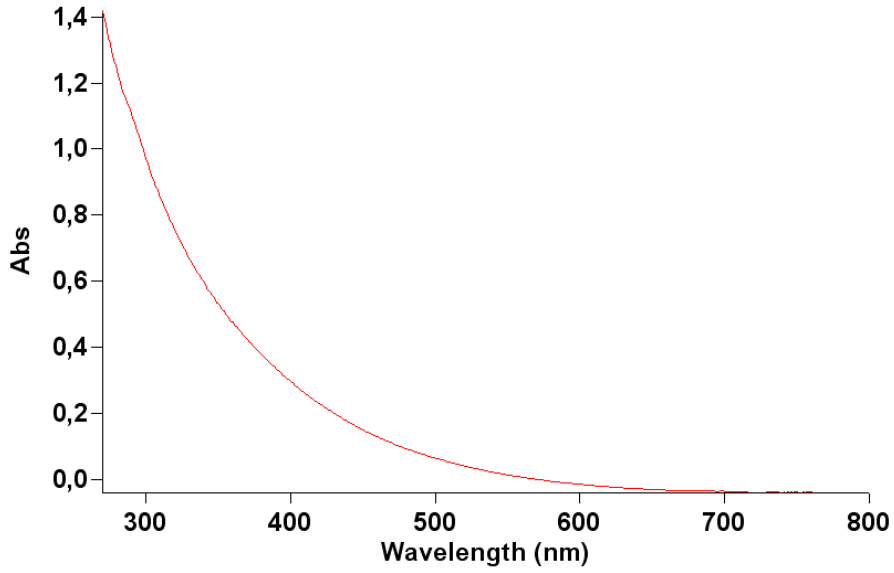

Fig.38 Optical absorption spectrum, of synthesized butanethiolate protected copper nanoparticles dispersed in dichloromethane.

X-Ray diffractometric analysys

Butanethiolate protected copper nanoparticles

Only a peak at 2 θ =4,7 is present in the butanethiolate protected copper nanoparticles diffractogram (Fig.39) suggesting a mesoporous nature of the solid formed by these copper nanoparticles.

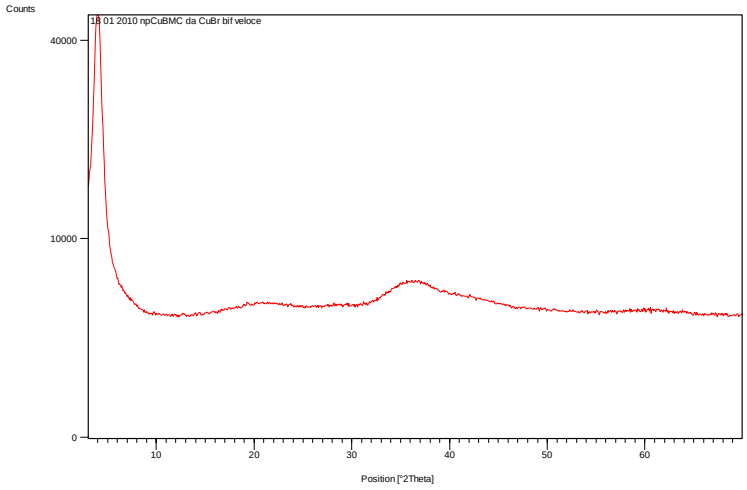

Fig.39 X-ray diffraction pattern of the butanethiolate protected copper nanoparticles (R)

Crystalline compound C

The X-ray diffraction pattern of the crystalline compound C , is reported in Fig.40.

Peaks at 2 θ = 5.6, 11.2, 16.8, 20,7 and 30.0 are present in this diffractogram while those due to the fcc copper metal and Cu_2O phases appearing at 2θ =38 and 18° are not detected. The series of peaks at low angles suggests a layered structure for this compound like that found by Sundyarany and Pradeep [57] for layered copper thiolates synthesized with the two phase Brust method [2] . The thermal decomposition at 423 K of these layered thiolates generates a product with a diffractometric pattern similar to that of the butanethiolate protected copper nanoparticles [57].

As can be deduced comparing the diffractometric patterns of M from the three syntheses, different amounts of nanoparticles and layered copper thiolates were obtained with the three methods. Namely method 3 led to a larger formation of thiolates with respect to the other two as can be deduced from diffractometric data (Fig.3)

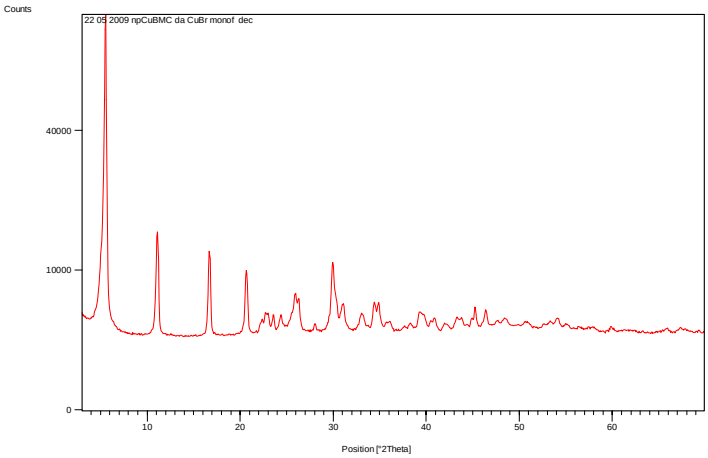

Fig.40 X-ray diffraction pattern of the yellow brown compound C.

FT-IR analysis

Butanethiolate protected copper nanoclusters

The butanethiolate copper nanoparticles, the layered copper thiolate C and the brown product M patterns presented only slight differences in the range 3000-2800 for all the three synthetic methods (Fig. 41).

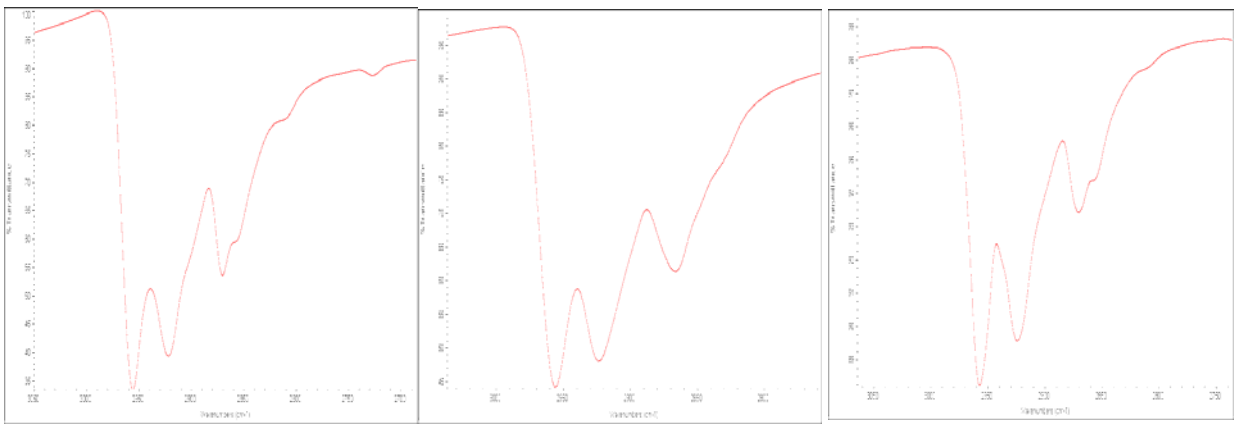

Fig 41 FT-IR spectra in the range 2800-3000cm-1 of the crystalline compound C(1), of the butanethiolate protected copper nanoclusters (2) and of the precipitate M (3)

The main absorption bands appearing in the spectra are due to symmetrical and antisymmetrical stretching vibrational modes of the methylenic protons (2871cm^{-1} and 2956 cm^{-1} respectively) and

to methylic protons (2924 cm^{-1}). This finding suggests a low degree of order in the butilic chain arrays both in the copper thiolates and copper nanoparticles. In fact bands at 2845 cm^{-1} and 2916 cm^{-1} are attributed to the same vibrational modes in the spectra of crystalline long chain hydrocarbons. This behaviour has been ascribed to the increased order degree of the all trans long alchilic chains in the crystalline phase with respect to the liquid one and is also found in the layered copper alkanethiolates when a number of CH_2 more than 8 is present in the chains [57].

In table 1 are reported the absorption bands in the range between 3000 and 2800 cm^{-1} for the nanoparticles R, the crystalline compound C and the precipitate M.

Table 1

	Value(cm-1)	Vibrational mode	Shape and intensity
Butanethiolate protected copper nanoparticles	2956	CH2 antisymmetrical stretching	Sharp and strong
	2925	CH3 stretching	Sharp and strong
	2872,2857	CH2 symmetrical stretching	Sharp and strong
crystalline compound C	2955, 2944,	CH2 antisymmetrical stretching	Sharp and strong
	2932	Shoulder	
	2902	shoulder	
	2922	CH3 stretching	Sharp and strong
	2872	CH2 symmetrical stretching	Sharp and strong
precipitate M	2957	CH2 antisymmetrical stretching	Sharp and strong
	2924	CH3 stretching	Sharp and strong
	2871	CH2 symmetrical stretching	Sharp and strong
	2856	shoulder	

FT-IR frequencies in the range 3000-2800cm-1 for the butanethiolate protected copper nanoparticles, crystalline compound C and the dark brown product M obtained with the synthetic route 2.

The absorption bands in the range between 1600-400 cm^{-1} for the butanethiolate protected copper nanoparticles (tab. 2), the layered copper thiolate C (tab. 3) and the brown precipitate M are reported in tables 2, 3 and 4 respectively.

Wavenumber(cm-1)	Absorption band shape	Vibrational mode
1458	Sharp, strong	Methylene shissoring
1425	medium shoulder	Deformation of the methylene adjacent to sulphur
1375 1351	Sharp; medium Weak shoulder	Methyl protons symmetrical bending
1291, 1261 1213	Sharp; weak Sharp; medium Sharp, strong	Wag twist progression series
1096, 1060, 1019	medium, sharp Unresolved, weak	C—C—C vibrational modes
909-872-802-779 621	Weak; sharp strong	Rocking modes

Table2. FT-IR main absorption frequencies in the range 1600-400 cm-1 appearing in the spectrum of the butanethiolate protected copper nanoparticles R

Wavenumber(cm-1)	Absorption band shape	Vibrational mode
1465	Sharp, strong	Methylene shissoring
1426	Sharp; strong	Deformation of the methylene adjacent to sulphur
1378 1348	Sharp; weak	Methyl protons symmetrical bending
1290, 1260 1209	Sharp; medium weak Shoulder Sharp, strong	Wag twist progression series
1095, 1053	Medium to weak Sharp, medium	C—C—C vibrational modes
904 721	Sharp, medium Sharp, strong	Rocking modes

Table 3 FT-IR main absorption frequencies in the range 1600-400 cm^{-1} appearing in the spectrum of the crystalline compound C

Wavenumber(cm-1)	Absorption band shape	Vibrational mode
1463	Sharp, strong	Methylene shissoring
1425	Sharp; medium	Deformation of the methylene adjacent to sulphur
1376	Sharp; medium weak	Methyl protons symmetrical bending
1290, 1262 1209	Sharp; medium to weak Sharp; medium to weak Sharp; strong	Wag twist progression series
1096 1053 1024	Weak, Sharp; Medium to weak weak	C—C—C vibrational modes
906 802, 778 721 624	Sharp, medium to weak Weak Medium, sharp Medium wide	Rocking modes

Table 4 FT-IR main absorption frequencies in the range 1600-400 cm^{-1} appearing in the spectrum of the brown precipitate from methanol M

Absorptions at 621(strong) and 624 nm (medium) appear in the copper nanoparticles and brown precipitate M spectra respectively but not in that of C (Fig.42). This finding is consistent with an hindrance in compound C of the rocking modes responsible for this absorption and can be ascribed to the order degree featuring the butylic moieties array on the nanoparticle surface. Furthermore the compound C presents more distinct in shape FT-IR absorptions than those appearing in the spectra of the nanoparticles and of the precipitate M. The presence of the wag–twist progression series (in the range of 1175 cm^{-1} to 1300 cm^{-1}) in all the spectra suggests that the butilic chains are in an all-trans arrangement [57].

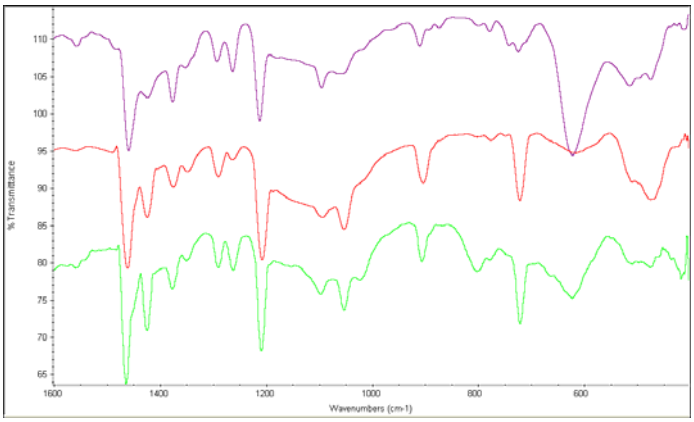

Fig.42 from the top: FT-IR spectra of the copper nanoparticles R, of the crystalline compound C, and of the brown compound precipitating from methanol M

5) 4-methylbenzenethiol protected copper nanoparticles

The same methods above described in for the butanethiolate protected copper nanoparticles were used.

Morphological analysys

The morphology of the reaction products was investgated by TEM microscopy.

The samples were prepared redispersing the brown precipitate both in dichloromethane and ethanol. Differences in morphology and stability of the products were found in the TEM micrographs depending only on the medium used to disperse the sample.

Synthesis route II(Dispersing medium: dichloromethane)

In Fig. 43 is reported the TEM micrograph of 4-methylbenzenethilate protected copper nanoclusters. They are round shaped, well monodispersed and present an average diameter of 3,5 nanometers. However dichloromethane was no more used as dispersing medium because of a partial disruption of the graphite layer protecting the copper grid.

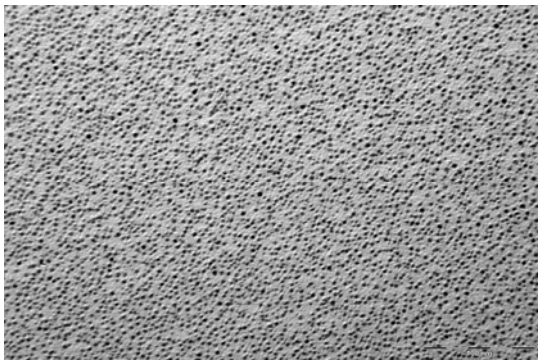

Fig. 43 TEM micrograph of 4-methylbenzenethiolate protected copper nanoparticles synyhesized a with method 2. Dichloromethane was used as dispersing medium.

Synthesis route II and III (Dispersing medium: ethanol)

Disordered strongly electro dense nanoparticle clusters kept together by a less dense binding medium appear in the TEM micrographs relative to both sintheses 2 and 3 (Fig. 44).

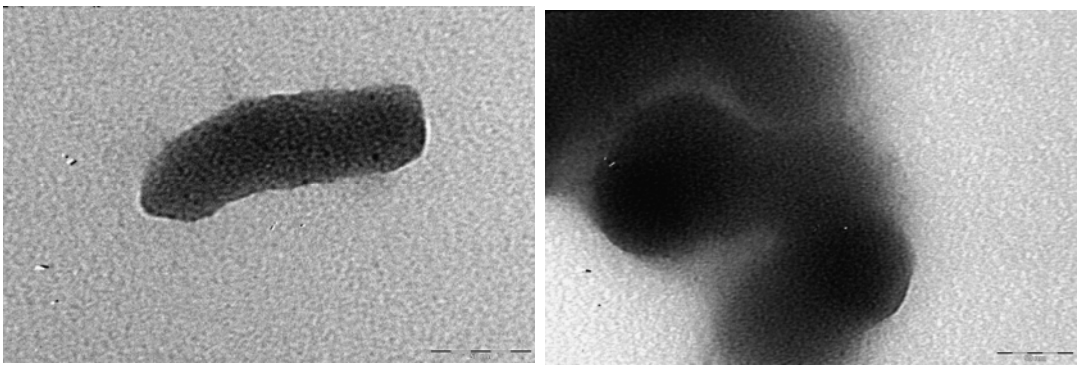

a b

Fig. 44 TEM micrograph of 4-methylbenzenethiolate protected copper nanoparticles synyhesized a) a with method 2 and b) with method 3) . Ethanol was used as dispersing medium.

Optical absorption studies

The spectrum of the 4-methylbenzenethiol protected copper nanoparticles revealed a Mie scattering profile like that observed for those butanethiol protected (Fig. 15). In this case however a net absorption maximum was observed at about 258 nm (Fig. 45) resembling that featured by monodispersed silver or gold nanoparticles protected with alcanethiols.

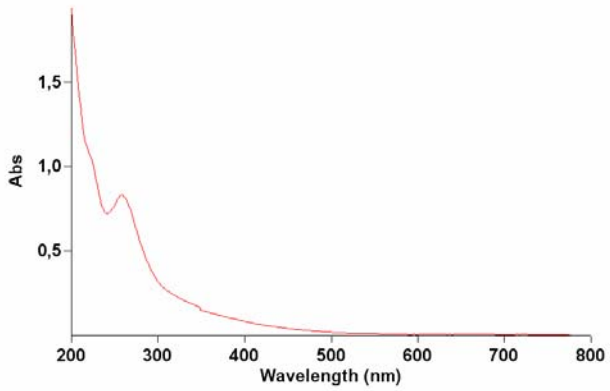

Fig. 45 Optical absorption spectrum, of synthesized 4-methylbenzenethiolate protected copper nanoparticles dispersed in dichloromethane (synthesis 2)

4 methylbenzenethiol spectrum recorded for comparison purpose (Fig. 46), shows an UV vis pattern typical of aromatic rings: Namely very strong absorption maxima at 223(A1) and 239,5 nm(A2) probably due to allowed $\pi \rightarrow \pi^*$ electronic transitions (these absorption maxima can be observed only in very diluted solutions 10-4—10-5 molar) and only a weak shoulder spanning the range 225-300nm (A3) appear in this spectrum. The last absorption can be attributed to a forbidden electronic transition that occurs owing to the molecule vibrational motions. The molar absorptivity ratios A1/A3 and A2/A3 were of 7,8 and 10 respectively.

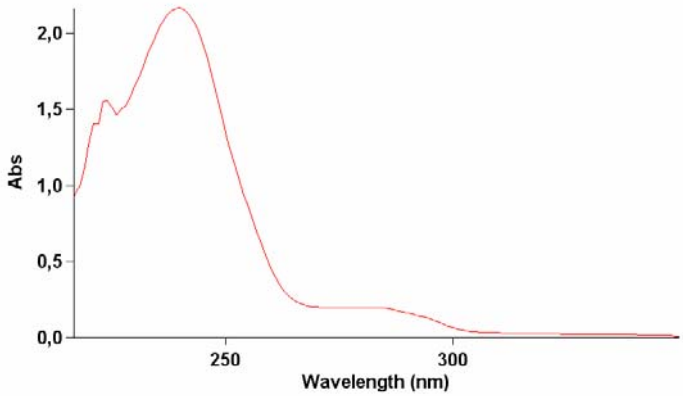

Fig. 46 Optical absorption spectrum obtained from a very diluted (about 10^{-4}molar) solution of the 4-methylbenzenethiol

The net maximum at 258 nm in the nanoparticle spectrum completely replaces the above said small shoulder in the 4methylbenzenethiol spectrum (Fig.47). This shoulder probably disappears also for an hindrance affecting the vibrational motions of the molecules blocked in rigid positions in the

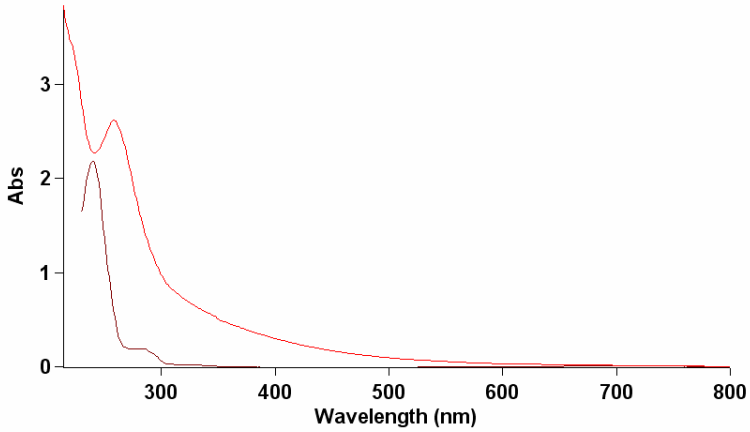

Fig. 47 Optical absorption spectrum of 4methylbenzenethiolate protected copper nanoparticles (above) and that of 4methylbenzenethiol .

ordered array on the nanoparticle surface. These findings suggested that the net absorption maximum at 258 nm in the 4methylbenzenethiolate copper nanoparticles could be due to the plasmonic resonance. Our hypothesis is strengthened by the work of Aslan and co-workers. They observed a plasmonic resonance absorption maximum at 289nm in the spectra of decanethiol, lauric acid and tridecylammine protected copper nanoparticles with average diameter of about 3,5 nm.
The presence of a net plasmonic resonance maximum in the spectrum is a proof that nanoparticles are well monodispersed (all with the same dimensions).

X-Ray diffraction analysys

The DRX patterns of 4-methylbenzenethiol protected copper nanoclusters synthesized with methods 2 and 3 are reported in Fig. 48. Only one peak is present in these diffractograms at 2θ=4,7° suggesting a mesoporous nature for the solid formed by the nanoparticles.

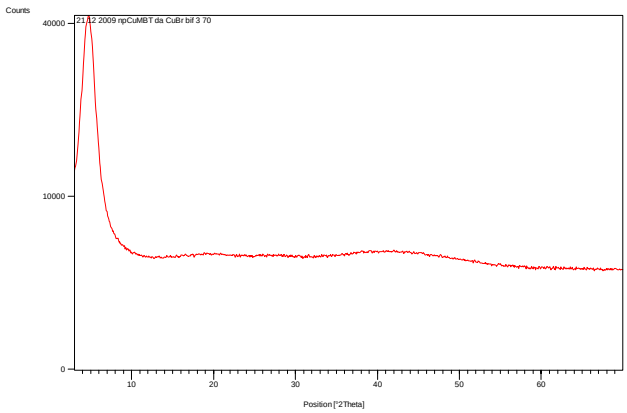

Fig. 48 X-ray diffraction pattern of synthesized 4-methylbenzenethiol capped copper nanoparticle. The diffraction pattern is the same for syntheses 2 and 3

FTIR Spectral Analysys

The most representative absorption bands appearing in the 4-methylbenzenethiolate protected copper nanoclusters FT-IR spectrum are reported in the following table with the relative vibrational modes:

Wavenumber(cm-1)	Absorption band shape	Vibrational mode
3017	Sharp, medium to weak	Aromatic C—H stretching
2959 2918 2861	shoulder Sharp strong Sharp medium	Methyl protons stretching
2000-1700	weak	Para substituted ring overtones
1629 1486	Sharp, Weak Sharp, strong	Aromatic ring carbon atoms stretching
1450 1396	Sharp weak Sharp, weak	Asymmetric methylic C—H bending Symmetric methylic C—H bending
1173 1084 1016	Shoulder medium Sharp, strong Sharp, strong	Aromatic C—H in plane bending
810	Sharp, strong	Aromatic C—H out of plane bending
622	Sharp, medium to weak	Methylic protons rocking

Table 4

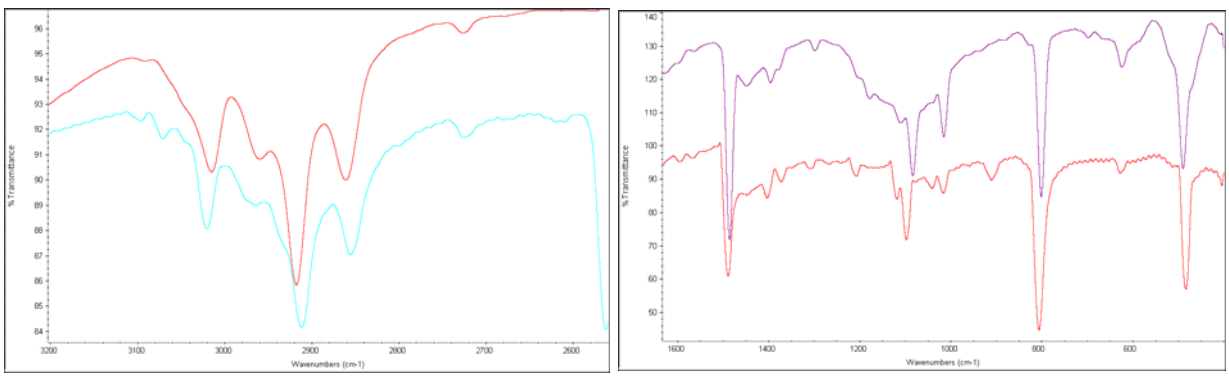

Fig. 49 FT-IR spectra of the 4methylbenzenethiol protected copper nanoparticles (above) and of the 4methylbenzenethiol.

The FT-IR spectrum of 4-methylbenzenethiolate protected nanoparticles is reported along with that of the 4-methylbenzenethiol for comparison purpose in Fig. 49.

Differences in the spectra relative to the synthesis methods 2 and 3 were not detected.

Absorptions due to aromatic C—H and methyl proton stretching, aromatic ring carbon atoms stretching and aromatic C—H out of plane bending have been found at almost the same wavenumbers and with the same features of intensity and shape in both the 4methylbenzenethiolate protected copper nanoclusters and crystalline 4methylbenzenethiol spectra. This finding suggests that the toluenic moieties surrounding the nanoparticle core, feature a degree of order similar to that observed in the solid phase 4-methylbenzenethiol. Namely they form a monomolecoular ordered array on the nanoparticle surface similar to that found in metallic nanoparticles coated with long chain (CH2>8) thiols.

In conclusion three synthesis methods to obtain copper nanoparticles protected with small molecules (butanethiol and 4-methylbenzenethiol) were compared.

Copper oxides were not detected in the reaction products for all the synthesis routes.

In the case of butanethiol, two reaction products formed in the three cases: namely butanethiolate protected copper nanoparticles and layered copper butanethiolates.

The last one couldn’t be detected by TEM investigation.

Reaction products featured different morphologies depending on the synthesis method:

Very small stable butanethiolate protected copper nanoparticles with dimensions ranging from two to three nanometers isolated or forming small clusters were obtained with synthesis route 2. On the contrary, syntheses 1 and 3 led to large nanoparticles with sizes ranging between 20 and 50 nanometers and rapidly disappearing under the electron beam of the TEM microscope.

In the case of 4-methylbenzenethyol syntheses 2 and 3 led both to the same product while a pale yallow crystalline compound was obtained with 1.

Differences in morphology depending on the dispersing medium used to prepare the TEM samples were observed also in this case: well monodispersed round shaped nanoparticles with average diameter of 3,5 nanometers and large nanoparticle clusters 100nanometers in size were observed when dichloromethane and water were used to prepare the TEM samples respectively. Both butanthiolate and 4-methylbenzenethiolate protected copper nanoparticle arrays showed diffraction patterns typical of mesoporous materials.

6) Phenol protected selenium nanoparticles

Phenol protected selenium nanoparticles have been synthetized according to the methods reported in the exsperimental section.

Morphological analysis

Nematic and spherical microstructures appear in the TEM micrograph of A from both the syntheses 1 and 2 (Fig. 50). They act as microvessels partially filled with the medium used to disperse the samples . The walls of these microstructures were found to be more fragile and easy to break when the reaction temperature was kept at 96° C instead of 104 °C.

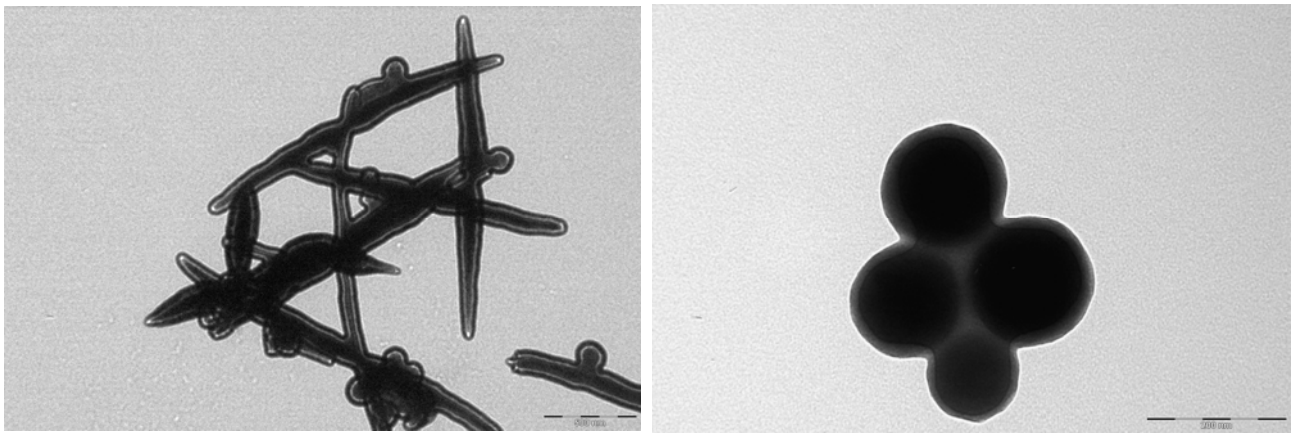

a b

Fig. 50 TEM micrograph of trigonal Se nanostructures observed after dispersion in ethanol of the precipitate A from formic acid (synthesis 1) revealing a nematic (a) and spherical (b) shape.

The TEM micrographs relative to the emptyng of these hollow structures under the TEM electron beam are reported in Fig. 51.

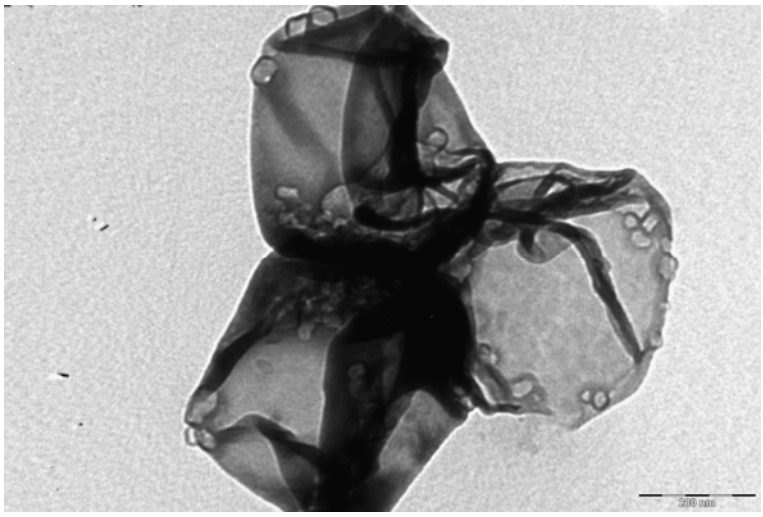

Fig. 51 TEM micrograph of trigonal Se nanostructures observed after dispersion in ethanol of the precipitate A from formic acid (synthesis 1 carried ot at 96°C) after removal of the liquid phase filling the cavities . Only few bubbled nanostructures were observed in the TEM micrograph of the precipitate B (Fig.3b)

A layer coating the selenium nanovessels can be clearly seen in the TEM micrograph relative to A and B from synthesis 1(Fig 52). This layer can be observed in other TEM micrographs but is quite difficult to distinguish from the graphite ground of the TEM grid due to the small sizes and low electrodensity of the nanoparticles. It can be thought to be formed by an ordered array of nanoparticles kept close together by means of hydrogen bonds occurring between the hydroxylic functions on phenol molecules coating the nanoparticle cores but also by polymeric species formed by reaction of phenol and formic acid. The granular nature of this layer can be pointed out by comparison with the TEM micrograph of floroglucinol capped selenium nanoparticles synthesized with a method reported in this work.

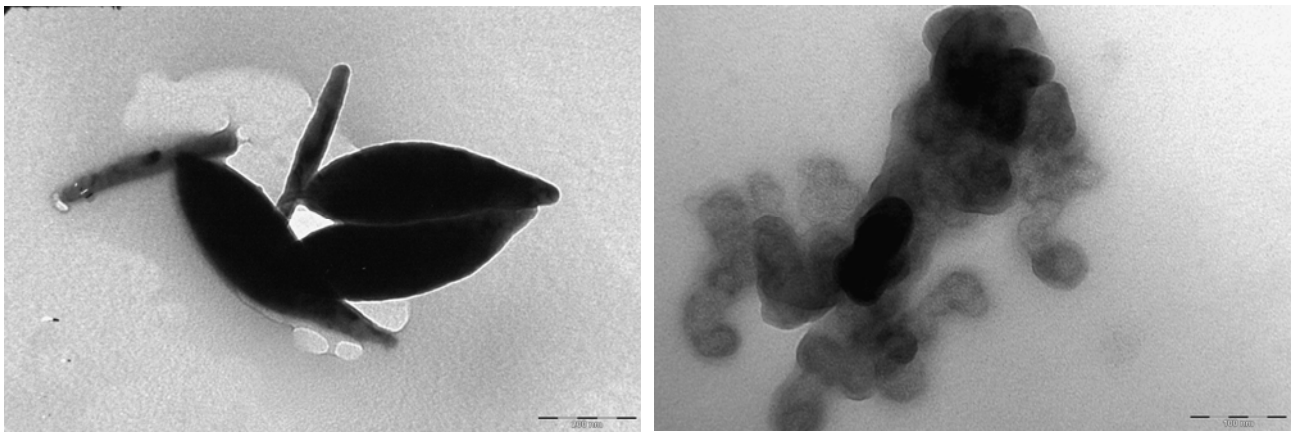

a b

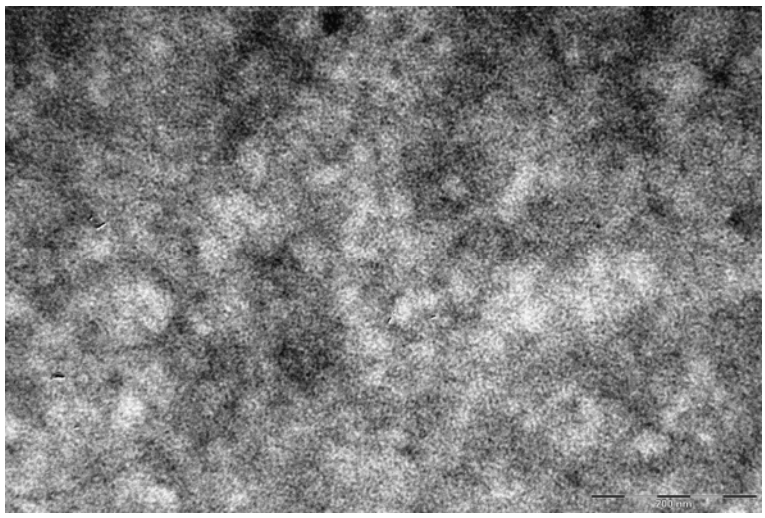

c

Fig. 52 TEM micrograph of the Se nanoparticles array coating the trigonal Se nanostructures observed after dispersion in ethanol of the precipitate A from formic acid a) B from water b)and of phloroglucinol capped Se nanoparticles revealing a nanometric dimension of about 2-3 nm in diameter c). Both A and B are relative to synthesis 1. Ethanol was used to disperse the samples.

Optical absorption studies

UV vis spectra were recorded with a CARY 300 BIO spectrometer in a double beam mode. The determinations were carried out dissolving about 3 mg of B from syntheses 1 and 2 in 2 ml of methanol. The suspension was centrifugated at 10000 rpm for 5 minutes and the supernatant diluted 1/10 (concentrated solution C) and 1/100(diluted solution D). 1ml path length quartz cuvettes were used in the experiment.

The spectra of both C and D present a typical Mie scattering profile according to the data reported in the work of Zong-Hong and co-workers (Fig. 53).

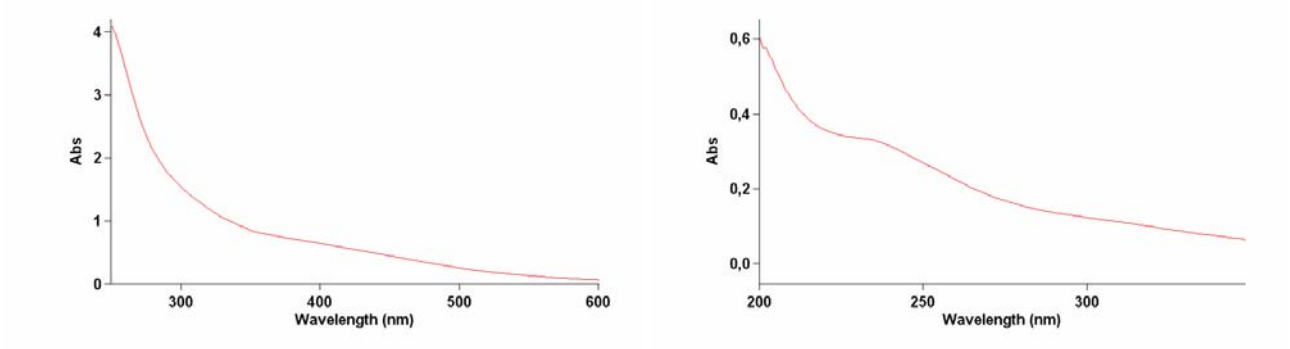

a b

Fig. 53 Optical absorption spectrum, recorded in the 350-600 nm wavelength range, of synthesized phenol capped Se nanoparticles sol dispersed in methanol in concentrated condition (a) Optical absorption spectrum, recorded in the 200-350 nm wavelength range, of synthesized phenol capped Se nanoparticles sol dispersed in methanol in deluded condition (b)

These authors found that the blue shift of the plasmonic resonance absorption maximum in the spectra of Se nanoparticles synthesized reducing selenous acid with sodium thiosulfate in presence of sodium dodecilsulfate as stabilizer, was directly dependent from a decrease of the nanoparticle average diameter. They recorded the spectra in a wavelength range spanning from 250 to 900nm and associated the absorbance maximum lacking spectral patterns with nanoparticle sizes less than 20nm. In the present work, spectra were recorded from 200nm with the aim of detect the absorptions of the phenolic moieties coating the selenium nanostructures. In fact the phenol spectrum presents two strong absorptions at 217 and at 272nm typical of aromatic rings. However the nanoparticle spectrum presented only a shoulder at around 250nm that was attributed to the plasmonic resonance according to the literature data. This finding is a proof that the synthesized nanoparticle average diameter is less than 20 nm and that a r crystalline semiconducting phase constitutes the nanoparticle core. The absence of the aromatic absorption maxima are probably due to the loose of the symmetry conditions that allow the electronic transition in the free molecule. In alternativa an absorption maximum at 205nm is ascribed to the electronic transition typical of aromatic rings.

X-Ray Diffractometric analysis

Comparison of the diffractometric pattern of A with that of the amorphous selenium (obtained reducing selenous oxide with ascorbic acid) shows that the former is a mixture of crystalline trigonal and amorphous phases (Fig. 5).

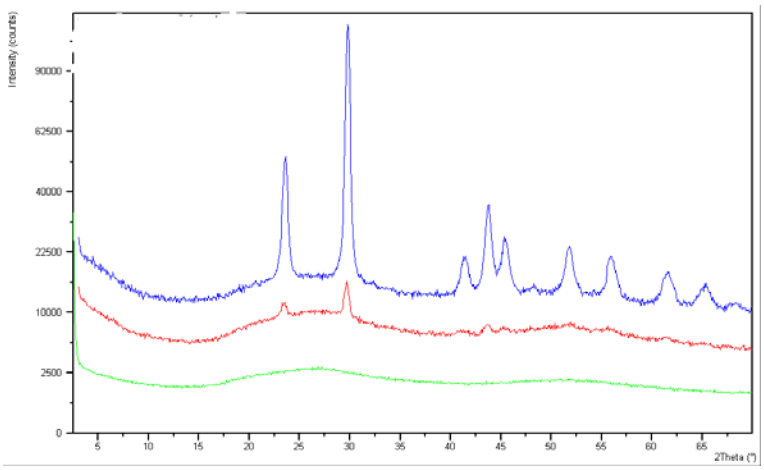

Fig. 54 From the top: X-ray diffraction patterns of the precipitate A from formic acid obtained at 104 °C, at 96°C and of the amorphous selenium obtained reducing selenous oxide by means of ascorbic acid.

The reflexes appearing in the diffractogram can be readily indexed to a trigonal phase of selenium (space group: $P3_121$ (152), with infinite, helical chains of selenium atoms packed parallel to each other along the *c*-axis) with lattice constants of *a*) 0.4365 nm and *c*) 0.4948 nm, which are in agreement with the values reported in literature(JCPDS 73-0465).

In table 1 are reported the angle values appearing in the diffractogram with the relative crystallographic indexes.

2θ(degree)	Crysiallographic index
23,5	100
29,6	101
41,3	110
43,6	012
45,4	111
51,7	201
55,7 (fused peaks)	003 112
61,4(fused peaks)	103 022
65,3	210
68,0	121

Table 1. Reflexes appearing in the precipitate A diffractogram

The diffractometric pattern of amorphous selenium shows two smooth maxima at 2θ = 26,9° and 52,4.

Only a maximum is present in the B diffractogram at 2θ =23,4° proving the presence of an organic phase coating the nanoparticle surface (Fig. 55). Identical patterns were found for B obtained with synthetic route 2 or when the synthesis 1 was carried out at 96°C.

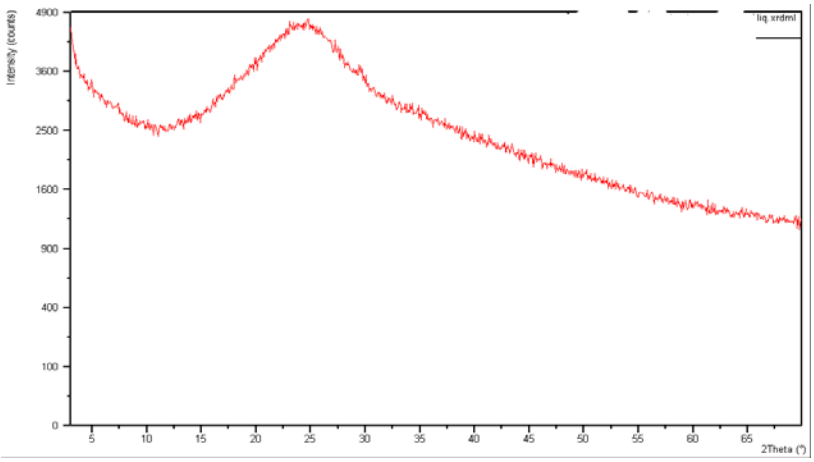

Fig. 55 X-ray diffraction pattern of the precipitate B from water obtained at 104 °C.

This organic phase prevents to detect possible weak (owing to the nanometric sizes of the objects studied) reflexes due to an underlyng crystalline phase and hence to prove that selenium trigonal phase constitutes the nanoparticle core.

A greater amount of amorphous selenium was observed to form when synthesis 1 was carried out at 96 °C (Fig.54).

FT-IR analysis

The samples for FT IR spectroscopic analysis were prepared mixing 2mg of A and B from syntheses 1 and 2 with 200mg of spectroscopic grade KBr. The pellets were obtained pressing at 10 tons 100 mg of the finely grinded mixture.

The infrared spectra were recorded under nitrogen atmosphere with transmission mode from 4000 to 400 cm^{-1} with a 2 cm^{-1} resolution using a NICOLET 380 FT-IR spectrometer. Other settings include a 4 mm aperture, 64 scans, velocity of 10 kHz, DLATGS detector and a 3-term Blackman-Harris apodization function.

The FT-IR spectra of A and B are reported in fig 56. Spectra of B from both syntheses 1 and 2 are identical.

They show about the same absorption bands appearing in that of A but more intense and resolved. This finding proves that the samples of B used to prepeare the KBr pelletts are more concentred in surface adsorbed molecules than those of A of the same weight. Id est the specific surface and hence the number of molecules adsorbed per surface unit is greater for B than for A. This evidence strengthens the suggestion that the precipitate B from water is formed by nanoparticles.

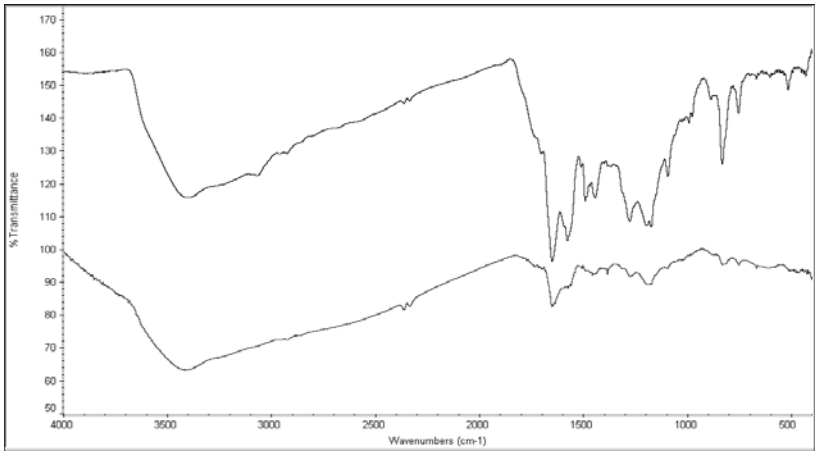

Fig. 56 FT-IR absorption spectra in the range 400-4000 cm^{-1} of A (above) and B from synthesis 1

The phenol molecules coating the nanoparticles surfaces form low ordered arrays as can be seen from the wider shape of the absorptions in the B FT-IR spectrum with respect to those appearing in that of loose crystalline phenol (Fig.57).

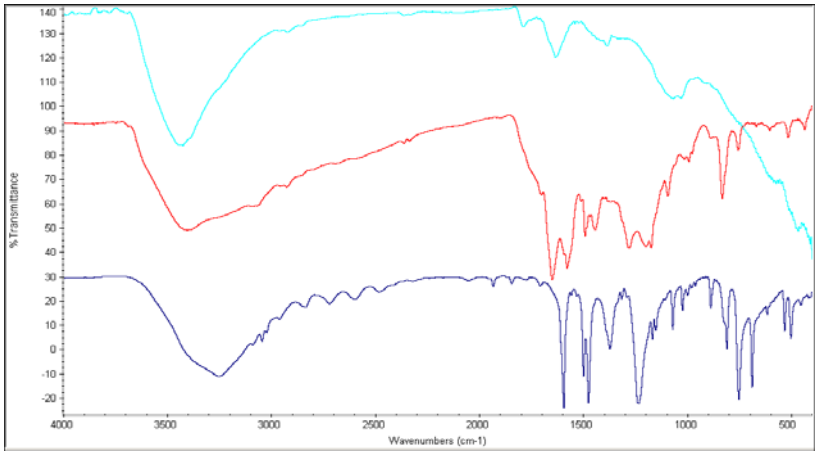

Fig. 57 From the top FT-IR absorption spectra of amorphous selenium obtained reducing selenous oxide with ascorbic acid, of precipitate B and of loose crystalline phenol used in the syntheses.

In FTIR pattern obtained for B a wide and strong absorption ranging from 3700cm^{-1} to 1800cm^{-1} with a minimum at 3403cm^{-1} and a shoulder from 3400 to 3100 are probably the superposition of a more sharp and symmetric band with a minimum at 3436 cm^{-1} present also in the spectrum of amorphous selenium (and ascribed to the presence of water irreversibly trapped in the amorphous phase) and another wide and asymmetric with a minimum at 3248 cm^{-1} due to the phenolic stretching (Fig. 57).

This evidence allows to conclude that the oxygen atom is not involved in the bond with the selenium nanoparticle surface.

A small shoulder centered around 3060 cm^{-1} is attributed to the fused C—H stretchings.

A series of small bands at 2958, 2921 and 2856 cm^{-1} are also present in the spectra of both precipitate B and amorphous selenium.

A series of absorptions typical of the aromatic C==C stretchings appear at 1648 (sharp and strong), 1577 cm^{-1} (sharp and strong), 1492 cm^{-1} (medium, sharp).

The absorption at 1648 appears blue shifted of 47cm^{-1} with respect to that ascribed to the same vibrational mode in the crystalline phenol spectrum.

An absorption with a trasmittance minimum at 1702 partially fused with that at 1648 cm^{-1} can be ascribed to the fusion of two bands appearing in the amorphous selenium spectrum and due to the presence of water.

A series of other bands below 1500 cm^{-1} are attributed to the vibrational modes reported in brackets: 1444cm^{-1}(medium to weak, sharp; O—H in plane bending), 1281 or 1199cm-1(strong, sharp; C—O stretching), 831(strong, sharp; C—H out of plane bending) and 756cm-1(weak; C—H out of plane bending).

Thermogravimetric and Differential scanning calorimetric analysis

Thermogravimetric (TGA-DTA) measurements were carried out using a ThemalAnalysis-SDT Q600 (TA Instruments, New Castle, DE, USA). Heating was performed in nitrogen flow (100 ml min^{-1}) using an alumina sample holder at a rate of 10 °C/min from room temperature to 1000 °C. The weight of the samples was approximately 1,8mg.

The TGA-DTA thermograms of the phenol capped synthesized Se nanoparticles (precipitate B) are reported in Fig. 58.

The sample is stable up to 232°C only small weigh losses of 0,4 and 1,1% taking place due to the desorption of water or phenol molecules weakly bonded to the nanoparticle surface.

Beyond this temperature the weigh% diminishes with temperature gradually. The derivative curve of the weigh% / T curve shows two large maxima ranging between 232 and 556°C
with Tmax of 342 and 475°C. Other hexothermic processes occur in the ranges 677-742°C and 742-816°C with weigh losses of 4,12 %and 4,80%. A slight slope change in the weigh% / T curve appears at about 556°C approximately corresponds with a minimum in the heath flow/T curve. An hexothermic process, probably the fusion of selenium nanoparticles in microparticles can be detected from a slight change in the heath flow/temperature curve between 186 and 500°C .

A ΔH of 2415J/g is observed in this temperature range.

The gradually decreasing ΔT/T curve trend up to a minimum at about 695°C proves that many physicochemical endothermic processes occur at the same time: Namely the cleavage of the C—Se bonds with depletion of the molecoular layer coating the nanoparticle surface, the selenium sublimation favoured by the depletion of the coating organic layer, a series of condensation reactions with loss of water and release of small more volatile compounds and finally the formation of a carbonic residue due to hydrogen loss from the remaining organic phase.

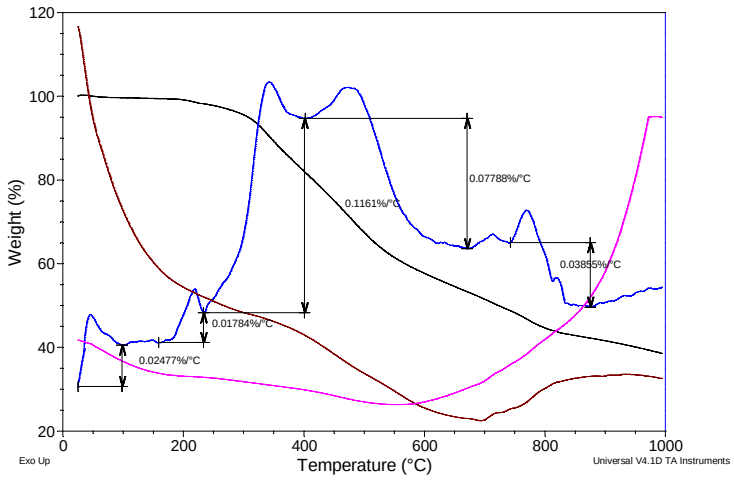

Fig. 58 TGA-DTA thermograms of the synthesized phenol capped Se nanoparticles (precipitate B).

To interprete these experimental data, a reaction mechanisms reported in fig.59 is proposed involving the presence in the reaction environment of the ionic couples (H—C==O+) (HCOO)- and (H—O—Se==O)+ HCOO- due to the autoprotolitic equilibrium taking place in formic acid.

2HC(O)OH → HCOO- + H—C==O+

According to the proposed mechanism, formonium (H—C==O)+ and selenonium (H—O—Se==O)+ cations react with phenol with an electronic substitution pathway that leads to 2-hydroxyaldehyde (or 4-hydroxyaldheide) and hydroxyphenilselenous acids (or hydroxyphenyl selenoxides) respectively . These cationic species can be protonated in their turn and react with other phenol molecules so becoming chain reaction propagators.

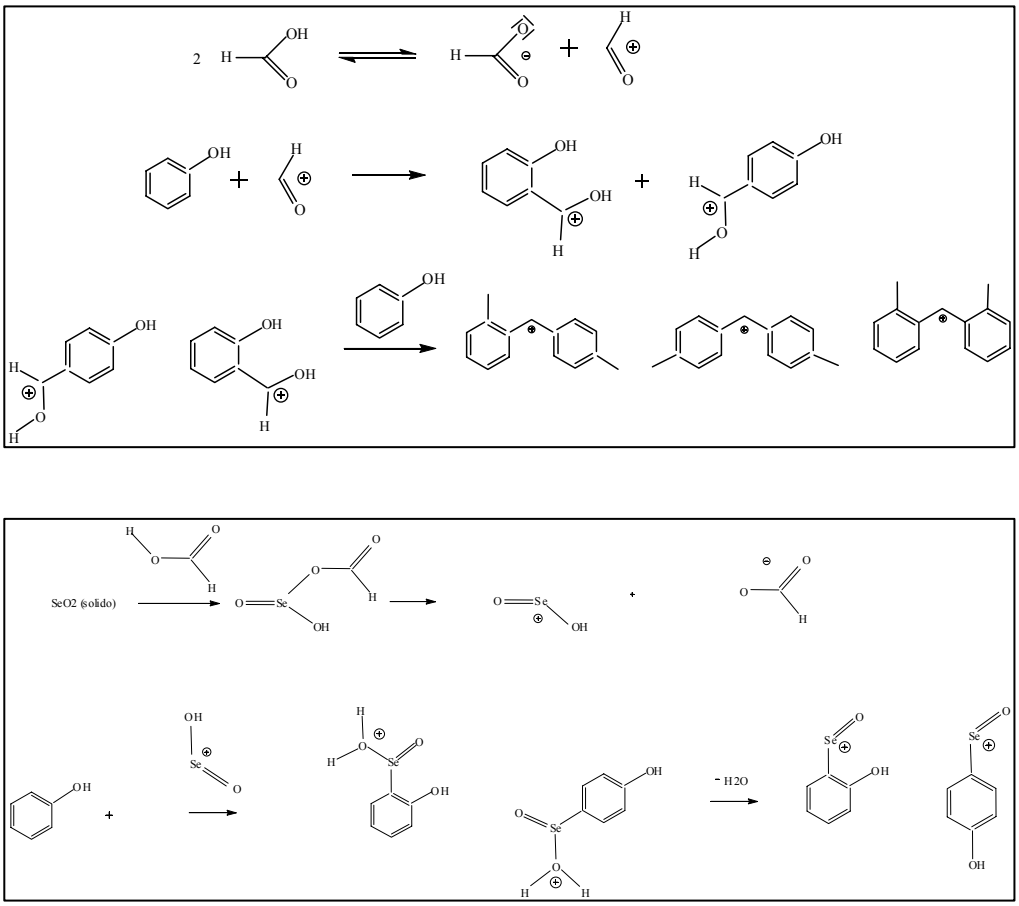

Fig. 59 Reaction mechanisms trigged by the autoprotolytic equilibrium of formic acid and leading to cationic reactive species able to bind to the nanoparticle surfaces

All these cationic species can be easily adsorbed on the selenium nanoparticle surfaces so blocking their growth and contrasting their tendence to form clusters.

On the other end polycondensations between phenol and hydroxybenzaldehyde (Fig. 60) formed by reaction between formonium cation and phenol (Fig. 59a) can occur involving also molecules

bonded to the nanoparticle surface and forming polymeric species which link the nanoparticles together and to the trigonal selenium microstructures. Nanoparticle- polymer composite layers are also among the causes of the absorptions appearing in the FT-IR specrum of the precipitate A.

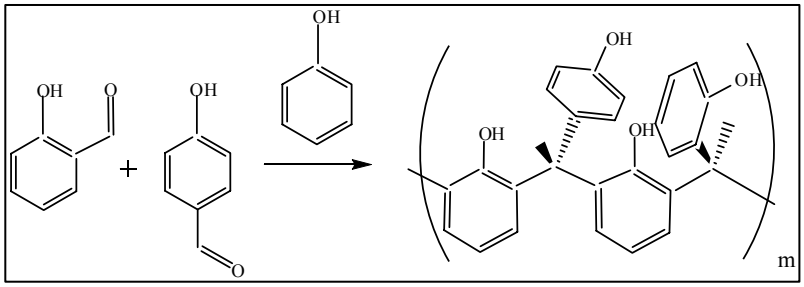

Fig. 60 Polycondensation reactions of ortho and para hydroxyaldehyde

A mechanism suggested by the work of Guangcheng Xi and co-workers is proposed to explain the formation of both the selenium nanopaticles and the trigonal selenium microstructures appearing in the TEM micrographs: according to this mechanism, the reaction conditions featuring the first part of synthesis1 (formic acid used both as dispersing medium and reducing agent, the absence of phenol and a reaction temperature of 104 °C) cause the formation in the liquid phase of trigonal selenium nanocrystals that aggregate together forming the hollow round shaped or nematic microstructures observed in the TEM micrographs. An equilibrium between selenium solubilized in formic acid, the nanocrystalline trigonal selenium nanocrystals dispersed in the liquid phase and trigonal selenium forming the microstructures takes place. Selenium atoms solvated by formic acid can assemble other nanocrystals that are adsorbed on the nanostructure surfaces or otherwise they can be directly adsorbed on the crystalline microstructures so forming layers of amorphous selenium on their surfaces.

As the reaction mixture is heathed in the second step of the synthesis after phenol addition, trigonal selenium nanocrystals form again in the liquid phase and the atoms on their surfaces can bind to the different phenolic species existing in the reaction environment. These species are also adsorbed on the surface of the partially crystallized selenium microstructures along with surface protected selenium nanoparticles so explaining the FT-IR spectroscopic pattern of A. This finding is more evident in the case of synthesis 2 when selenous oxide and phenol are mixed at the same time.

The organic layer on the nanocrystal surface is probably responsible of the diffractometric pattern of B: reflexes typical of trigonal selenium cannot be detected probably due to both the low crystallinity degree of these nanometric size objects and to the organic layer coating their surface. However the presence of a shoulder at about 250 nm attributed to a plasmon resonance in the UV-vis spectrum of B according to the literature data, suggests that the nanoparticle core is made of a semiconducting crystalline trigonal selenium phase.

In conclusion the formation of semiconducting trigonal selenium nanocrystals is suggested by the presence of a shoulder at 250 nm in the UV-Vis spectrum of the precipitate B obtained with the two reported synthesis methods. This suggestion is strnghtened by the presence of partially crystallized trigonal selenium microstructures forming the precipitate A from formic acid and probably due to an irreversible aggregation process involving the trigonal selenium nanocrystals initially dispersed in formic acid. This process is typical of all the surface protected nanoparticles.Unfortunately these nanocrystals are very difficult to detect by TEM mycroscopy owing to their low electrodensity. They are supposed to form sheets coating both the grid graphite layer and the nanostructure surfaces. In this work dispersing agents like tetraoctilammonium bromide were not used. However nanoparticles can be easily redispersed in ethanol,methanol, acetone and dimethylsulfoxide and other organic solvents even after six months.

Diffractometric and spectroscopic data reveal that decomposition processes didn't occur in both the precipitates A from formic acid and B from water in this period of time.

The synthesis is easy to carry out and requires only two or three hours to be completed.

Furthermore reagents are cheap and easy to find.

Phloroglucinol protected selenium nanoparticles

TEM analysis

The morphology of the Se particles synthesized and stored in dried condition, as reported in experimental section, has been investigated by TEM. The samples were prepared evaporating small drops of a particle dispersion in booth ethanol or water on a carbon coated copper grid.

In Fig.61 is reported the TEM micrograph of the Se particles observed after dispersion in water; these reveal a spherical shape ranging from about 200 to 700 nm in diameter. The particles appear strongly electro dense coherently with their insolubility and fast separation in water in an orange-brown precipitate.

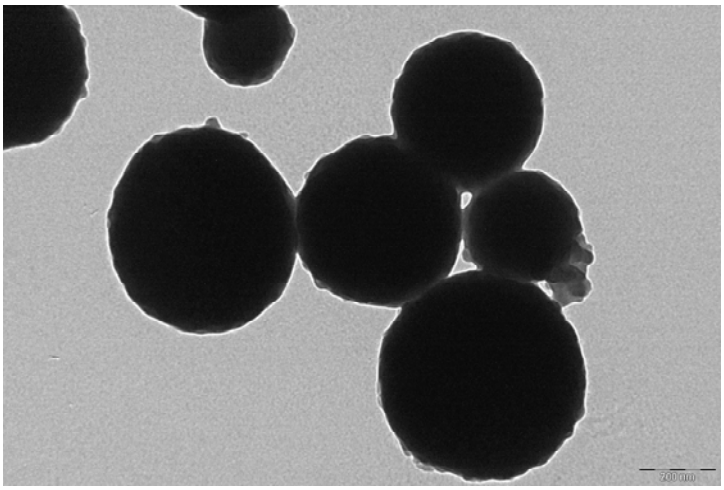

Fig.61 TEM micrograph of phloroglucinol capped Se nanoparticles observed after dispersion in water, revealing a spherical shape ranging from about 200 to 700 nm in diameter.

In Fig. 62 is reported the TEM micrograph of the same Se particles observed after dispersion in ethanol. In this solvent, Se particles appear homogenously dispersed forming a yellow suspension. Se particles reveal a nanometric dimension of about 2-3 nm in diameter which remain stable in drying condition or if stored in ethanol at room temperature and in dark conditions.

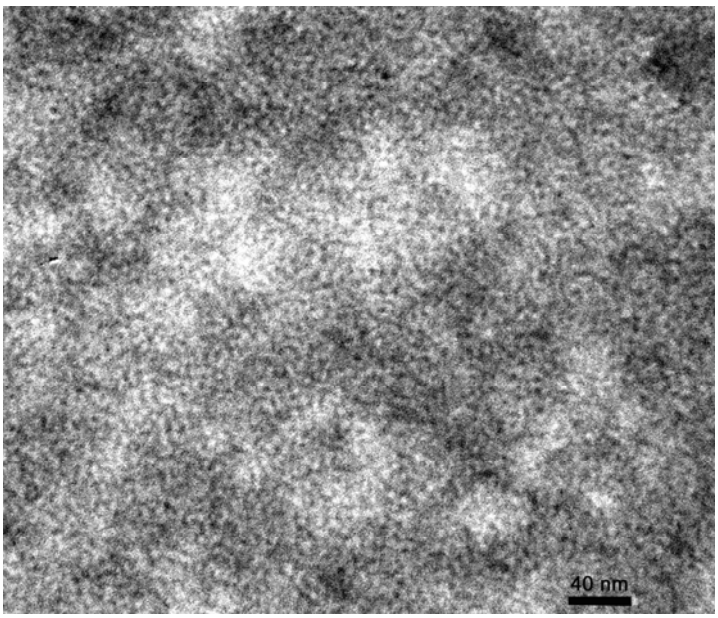

Fig. 62 TEM micrograph of phloroglucinol capped Se nanoparticles observed after dispersion in ethanol, revealing a nanometric dimension of about 2-3 nm in diameter.

The homogeneous nanometric size of the particles can be ascribed to the phloroglucinol molecules bound on the Se particles surface. Phloroglucinol molecular assembly on the Se nanoparticles can be partially removed by heat treatment at 285 °C for 10 minutes and Se nanoparticles aggregate in micrometric entities with a morphology (Fig. 63) that resembles closely that obtained in water dispersion (Fig. 62)

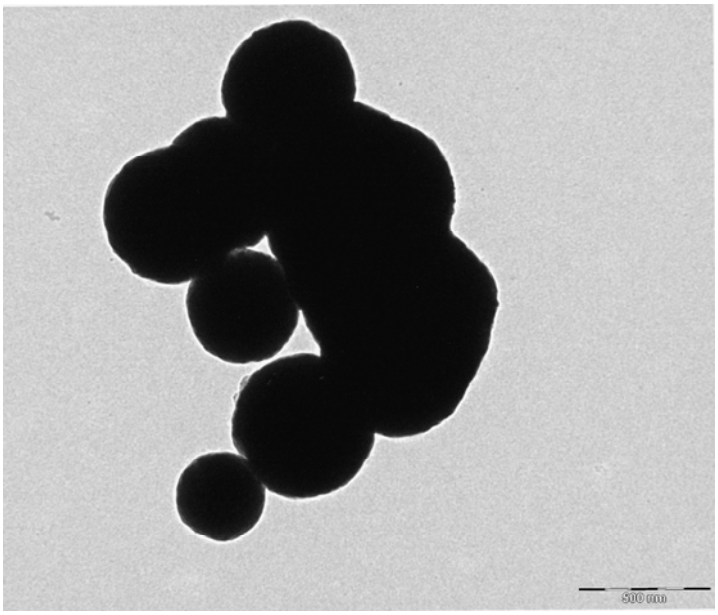

Fig.63 TEM micrograph of dispersed in ethanol phloroglucinol capped Se nanoparticles after heat treatment at 285 °C for 10 minutes.

FT-IR Analysis

The FT-IR absorption pattern of phloroglucinol surface protected Se nanoparticles dispersed in ethanol is reported in Fig. 64a. This pattern does not differ appreciably from that recorded for phloroglucinol surface protected Se nanoparticles stored in ethanol at room temperature and in darkness for a week (Figs. 64b and 65b) and for two month (Figs. 64c and 65c). We can compare the FT-IR absorption pattern of phloroglucinol surface protected Se nanoparticles Fig. 64a with that of phloroglucinol Fig. 64e. The FT-IR absorptions bands at 2958, 2925 and 2852 cm^{-1} , typical of the symmetrical and antisymmetrical C-H stretching vibration, are present in both the patterns and well resolved in phloroglucinol capped Se particles FT-IR spectrum. The latter exhibits three sharp and strong absorption bands at 1597, 1426 and 1467 cm^{-1} which appear shifted to lower wave numbers with respect to those ascribed to the same modes in the phloroglucinol FT-IR spectrum (1618, 1535, and 1499) and are indicative of stretching vibrations due to carbon atoms in aromatic rings. This finding can be attributed to the interaction of phloroglucinol molecules via π electrons

with the Se particles surface. In FT-IR spectrum of phloroglucinol capped Se particles the absorption at 1618 cm^{-1} appears like a single band (Fig. 65a), which gradually splits into bands after about two months storage at room temperature in dark environment, probably due to a structural reorganization of phloroglucinol molecules surface capped on Se particles. In fact, this splitting of the single absorption band at 1597 cm^{-1} is present in the FT-IR spectra not only of phloroglucinol, but also of many molecules with aromatic rings bearing C-O bonds in alternate position like resorcinol and 2-metil resorcinol. The FT-IR spectrum of 1618 cm^{-1} capped Se particles heated at 285 °C for 10 minutes (Fig. 65d) shows a single absorption band at 1618 cm^{-1} suggesting a breaking of the surface interaction between Se particles and phloroglucinol molecules decomposition products.

The strong wide and sharp absorption band at 3359 cm^{-1} can be attributed to the OH stretching vibrational mode, allowing to hypothesise the presence in the molecule linked to the Se surface of single OH group. In fact, phloroglucinol FT-IR pattern exhibits three fused absorption bands in the 3000 – 3500 cm^{-1} region coherently with its three OH groups. This finding suggests a condensation reaction between subsequent phloroglucinol molecules fastened on the Se surface, inducing a C-O-C bond between them. This hypothesis is supported by two absorption bands appearing at 1246 and 1046 cm^{-1}, which can be ascribed to the symmetrical and antisymmetrical C-O-C stretching vibration.

The phloroglucinol FT-IR spectrum shows three sharp and strong absorption bands at 821, 780 and 727 cm^{-1}, which may be due to the out of plane bending modes of the hydrogen atoms.

On the contrary, in the phloroglucinol capped Se nanoparticles FT-IR spectrum a lack of strong absorptions between 900 and 700 cm^{-1} is evident; in fact, there is only a weak and sharp band at 820 cm^{-1}, which can be ascribed to the hindered bending vibrational modes of the hydrogen atoms in phloroglucinol molecules constrained on the nanoparticle surface in rigid positions and forming an ordered array.

Consequently, in the phloroglucinol capped Se nanoparticles FT-IR spectrum, the stretching vibrational modes of the O—H an C—H bonds free from sterical hindrance give rise to absorption bands at 3359 cm^{-1}(O—H) and at 2958, 2925 and 2852 cm^{-1}(C—H), which appear sharper than those observed after thermal treatment (Fig. 64d). In fact, the shoulder shaped form or the absorption bands in the 3500-3000cm^{-1} region observed in the thermal treated Se nanoparticles FT-IR spectrum is probably due to a partial disruption of the quite ordered phloroglucinol molecular array initially present on the Se nanoparticle surface.

The evaluation of FT-IR results provided information about the structural organization of phloroglucinol molecules bound on the Se particles surface corresponding to a network of

molecules linked together by C-O-C bonds.

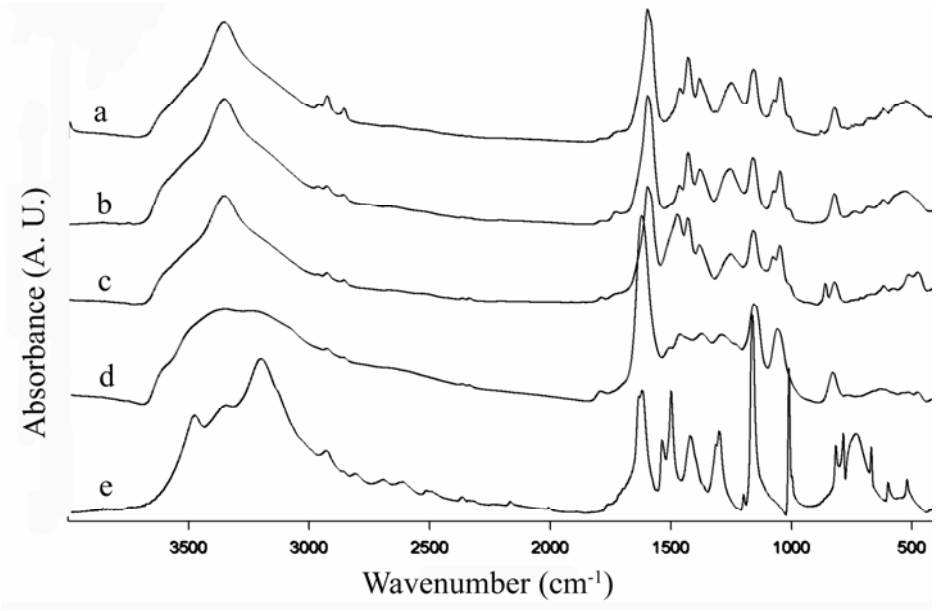

Fig.64 FT-IR absorption spectra in the range 400-4000 cm^{-1} of phloroglucinol capped Se nanoparticles as synthesized a), stored for a week b), stored for two months c) after heat treatment at 285 °C for 10 minutes d) and phloroglucinol crystalline powder e)

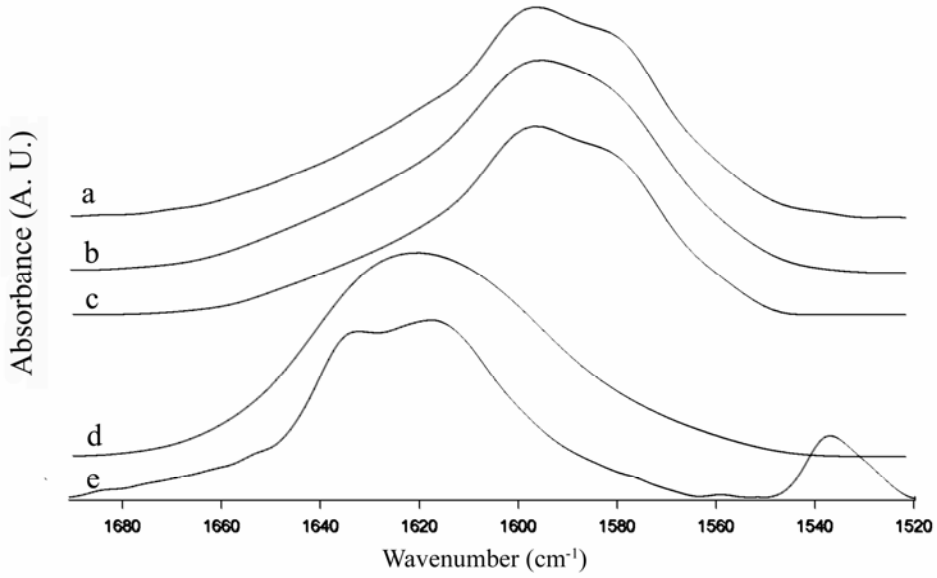

Fig.65 FT-IR absorption spectra in the range 1500-1700 cm^{-1} of phloroglucinol capped Se nanoparticles as synthesized a), stored for a week b), stored for two months c) after heat treatment at 285 °C for 10 minutes d) and phloroglucinol crystalline powder e)

X-ray diffraction studies

The X-ray diffraction pattern of synthesized phloroglucinol capped Se nanoparticles is reported in Fig. 66a and compared with the X-ray diffraction pattern of the same sample treated at 285 °C

for 10 minutes (Fig. 66b). This thermal treatment causes a partial desorption of the phloroglucinol molecules on the Se nanoparticle surface, as it can be hypnotized from the results obtained by thermogravimetric and differential scanning calorimetric analysis. The X–ray diffraction pattern of phloroglucinol capped Se nanoparticles shows three broadened diffraction maxima probably due to the phloroglucinol molecoular assembly on the Se nanoparticle surface. This poorly crystalline molecular assembly is partially removed by heat treatment and the X–ray diffraction pattern (Fig. 66b) shows no sharp Bragg reflections, except for a broad peak centred at about 2θ = 25° and its second order at about 2θ = 50° resembling closely the X–ray diffraction pattern observed for amorphous Selenium.

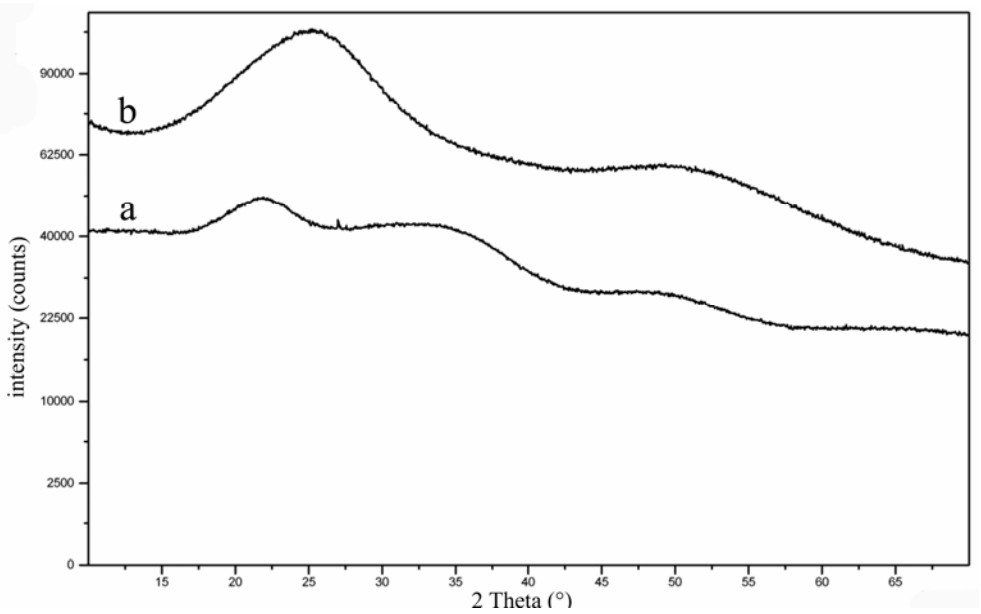

Fig.66 X-ray diffraction pattern of synthesized phloroglucinol capped Se nanoparticles before (a) and after heat treatment at 285 °C for 10 minutes (b)

Optical absorption studies

The UV-visible optical absorption spectrum of the yellow-orange coloured concentrated sol dispersed in ethanol of synthesized phloroglucinol capped Se nanoparticles has been recorded in the wavelength range of 350-700 nm and reported in Fig. 67a. This absorption spectrum shows a characteristic shoulder in the 450-500 nm region and can be considered as an excitonic maximum for Se nanoparticles proving the Se nanoparticles existence.

The UV-visible optical absorption spectrum of the pale yellow diluted sol of synthesized phloroglucinol capped Se nanoparticles dispersed in ethanol has been recorded in the wavelength range of 200-350 nm and reported in Fig. 67b. The absorption maximum to about 220 nm can be

ascribed to the phloroglucinol molecules linked on the Se nanoparticles surface according to the results previously reported in the UV-vis kinetic study carried out on phenyl Se oxide molecules. In fact, the phloroglucinolic moieties could be linked together on the Se nanoparticles surface forming a net of entities resembling phenyl Se oxide molecules very closely.

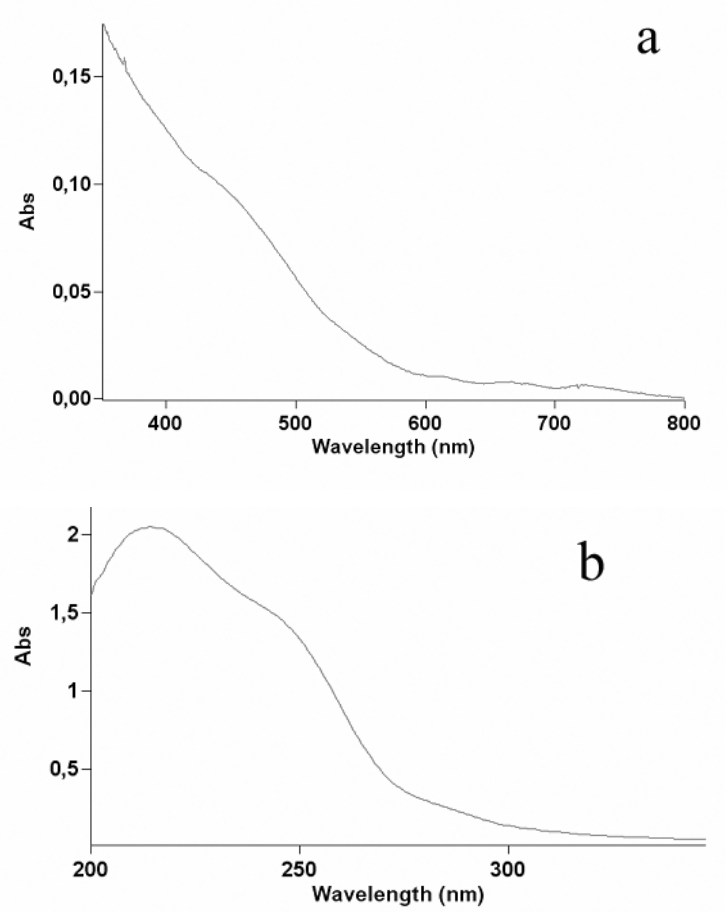

Fig. 67 Optical absorption spectrum, recorded in the 350-700 nm wavelength range, of synthesized phloroglucinol capped Se nanoparticles sol dispersed in ethanol in concentrated condition (a) Optical absorption spectrum, recorded in the 200-350 nm wavelength range, of synthesized phloroglucinol capped Se nanoparticles sol dispersed in ethanol in deluded condition (b)

Thermogravimetric and Differential scanning calorimetric analysis

The TGA-DTA thermograms of both the phloroglucinol capped synthesized Se nanoparticles and the phloroglucinol crystalline powder are reported in Fig. 68a and 68b respectively.

The TGA-DTA thermogram of phloroglucinol crystalline powder show a first weight loss of about 20 % in the 80-95 °C range ascribed to crystallization water remotion. Endothermal processes of sublimation and fusion of the phloroglucinol are responsible for the DTA signal at around 223 °C,

while other two weight losses at 256,09 °C and at 315,73 °C are due to thermal decompositions (probably polycondensation reactions) of the phloroglucinol molecules.

The TGA-DTA thermogram of the synthesized Se nanoparticles shows an about 12% weight loss at 275 °C and the almost complete weight loss (50%) at about 500 °C, ascribable to the amorphous Selenium sublimation process.

The former weight loss at 275 °C can be ascribed to an exothermal aggregation process of the Selenium nanoparticles which cast together in microspheres of amorphous Selenium (Fig. 63).

Namely, due to the increased thermal motion, Se nanoparticles can reach an activation energy that allows them to fuse together (Fig. 63), partially removing the layer made of phloroglucinol molecules and other decomposition products on their surface (Fig. 64d).

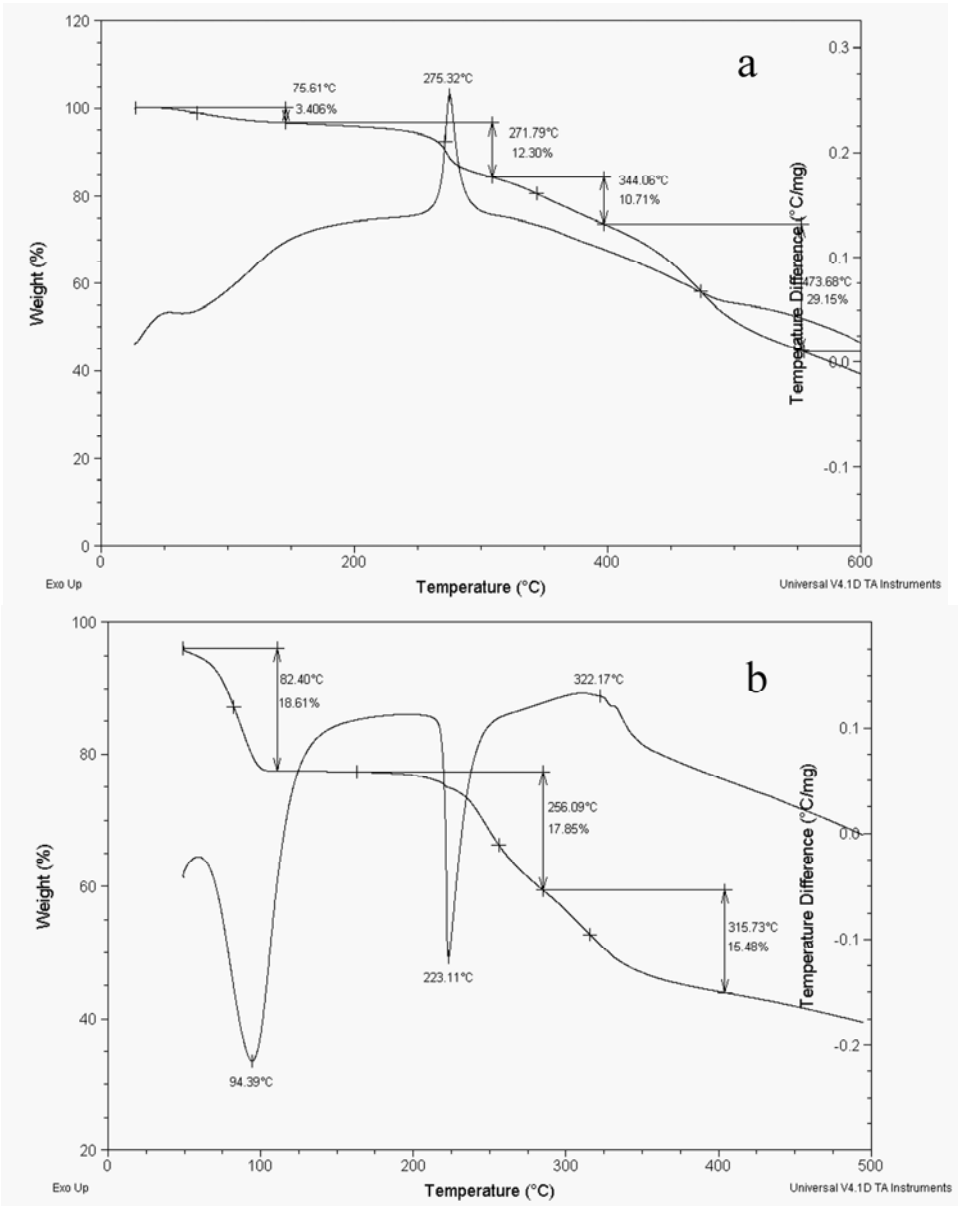

Fig. 68 TGA-DTA thermograms of the synthesized phloroglucinol capped Se nanoparticles and the phloroglucinol crystalline powder are reported in (a) and (b) respectively.

In conclusion, Phloroglucinol surface protected Se nanoparticles have been synthesized by a green method without any organic solvent and utilising phloroglucinol as reducing and capping agent, to obtain Se nanoparticles for biomedical application. In fact, phloroglucinol is a molecule present in many flavonoid compounds widely present in vegetables and it was found to possess cytoprotective effects against oxidative stress. The antioxidizing and cytoprotective properties of phloroalucinol can produce synergies with the specific anticarcinogenic effects of Se nanoparticles.

Phloroglucinol exhibits a high reactivity due to its three hydroxyl groups disposed in alternate positions along a benzene ring, which is so activated toward electrophilic substitutions. Phloroglucinol acts as a reducing agent on selenous acid according to a complex path that probably passes through an organic selenoxide intermediate. This intermediate can be formed by an electrophilic substitution reaction involving selenous acid as the electrophilic species and phloroglucinol as an electron donor. The reaction product can be bound on the Selenium nanoparticle surface via the Selenium atom, forming an organic layer that prevents nanoparticle aggregation.

The phloroglucinol molecules on the Se nanoparticle surface are probably linked each other via oxygen atoms bridging subsequent molecules, as it can be deduced comparing FT-IR spectra in Fig 64e and 64a. In fact, only one of the three absorption bands in the 3500-3000 cm^{-1} range of FT-IR at phloroglucinol spectrum (Fig. 64e), ascribed to the three OH stretching vibrational mode, is detectable in the FT-IR spectrum of phloroglucinol capped Se nanoparticles (Fig. 64a).

The poorly crystalline phloroglucinol molecular assembly coating on the Se nanoparticle surface can be disrupted and partially removed by an hexothermal casting process at about 275 °C. The depletion of the surface protective phloroglucinol coating causes the Se nanoparticles aggregation in micrometric clusters (Fig. 63) very morphologically similar to those observed when nanoparticles are dispersed in water medium (Fig. 61). In ethanol, phloroglucinol protected amorphous Se nanopartcles of 2-3 nm in diameter appear homogeneously distributed. They appear stable without an appreciable dimension change if stored at room temperature and in darkness, even if probably a structural reorganization of phloroglucinol molecules surface capped on Se particles gradually takes place after two months.

Conclusions

The stabilization of nanoparticles against their irreversible particle aggregation and oxidation

reactions. is a requirement for further advancement in nanoparticle science and technology. For this reason the research aim on this topic focuses on the synthesis of various metal nanoparticles protected with monolayers containing different reactive head groups and functional tail groups. In this work cuprous bromide nanocrystals haave been synthetized with a diameter of about 20 nanometers according to a new sybthetic method adding dropwise ascorbic acid to a water solution of lithium bromide and cupric chloride under continuous stirring and nitrogen flux. Butane thiolate Cu protected nanoparticles have been synthetized according to three different syntesys methods. Their morphologies appear related to the physicochemical conditions during the synthesis and to the dispersing medium used to prepare the sample. Synthesis method II allows to obtain stable nanoparticles of 1-2 nm in size both isolated and forming clusters. Nanoparticle cluster formation was enhanced as water was used as dispersing medium probably due to the idrophobic nature of the butanethiolate layers coating the nanoparticle surface. Synthesis methods I and III lead to large unstable spherical nanoparticles with size ranging between 20 to 50 nm. These nanoparticles appeared in the TEM micrograph with the same morphology independently on the dispersing medium used in the sample preparation. The stability and dimensions of the copper nanoparticles appear inversely related. Using the same methods above described for the butanethiolate protected copper nanoparticles 4-methylbenzenethiol protected copper nanoparticles have been prepared. Diffractometric and spectroscopic data reveal that decomposition processes didn't occur in both the 4-methylbenzenethiol copper protected nanoparticles precipitates from formic acid and from water in a period of time six month long.

Se anticarcinogenic effects by multiple mechanisms have been extensively investigated and documented and Se is defined a genuine nutritional cancer-protecting element and a significant protective effect of Se against major forms of cancer. Furthermore phloroglucinol was found to possess cytoprotective effects against oxidative stress, thanks to reactive oxygen species (ROS) which are associated with cells and tissue damages and are the contributing factors for inflammation, aging, cancer, arteriosclerosis, hypertension and diabetes. The goal of our work has been to set up a new method to synthesize in mild conditions amorphous Se nanopaticles surface capped with phloroglucinol, which is used during synthesis as reducing agent to obtain stable Se nanoparticles in ethanol, performing the synergies offered by the specific anticarcinogenic properties of Se and the antioxiding ones of phloroalucinol. We have synthesized selenium nanoparticles protected by phenolic molecules chemically bonded to their surface. The phenol molecules coating the nanoparticles surfaces form low ordered arrays as can be seen from the wider shape of the absorptions in the FT-IR spectrum with respect to those appearing in that of crystalline phenol.

On the other hand, metallic nanoparticles with unique optical properties, facile surface chemistry and appropriate size scale are generating much enthusiasm in nanomedicine. In fact Au nanoparticles has immense potential for both cancer diagnosis and therapy. Especially Au nanoparticles efficiently convert the strongly adsorbed light into localized heat, which can be exploited for the selective laser photothermal therapy of cancer. According to the about, metal nanoparticles-HA nanocrystals composites should have tremendous potential in novel methods for therapy of cancer. 11 mercaptoundecanoic surface protected Au4Ag1 nanoparticles adsorbed on nanometric apathyte crystals we have successfully prepared like an anticancer nanoparticles deliver system utilizing biomimetic hydroxyapatyte nanocrystals as deliver agents.

Furthermore natural chrysotile, formed by densely packed bundles of multiwalled hollow nanotubes, is a mineral very suitable for nanowires preparation when their inner nanometer-sized cavity is filled with a proper material. Bundles of chrysotile nanotubes can then behave as host systems, where their large interchannel separation is actually expected to prevent the interaction between individual guest metallic nanoparticles and act as a confining barrier.

Chrysotile nanotubes have been filled with molten metals such as Hg, Pb, Sn, semimetals, Bi, Te, Se, and with semiconductor materials such as InSb, CdSe, GaAs, and InP using both high-pressure techniques and metal-organic chemical vapor deposition. Under hydrothermal conditions chrysotile nanocrystals have been synthesized as a single phase and can be utilized as a very suitable for nanowires preparation filling their inner nanometer-sized cavity with metallic nanoparticles. In this research work we have synthesized and characterized Stoichiometric synthetic chrysotile nanotubes have been partially filled with bi and monometallic highly monodispersed nanoparticles with diameters ranging from 1,7 to 5,5 nm depending on the core composition (Au, Au4Ag1, Au1Ag4, Ag). In the case of 4 methylbenzenethiol protected silver nanoparticles, the filling was carried out by convection and capillarity effect at room temperature and pressure using a suitable organic solvent. We have obtained new interesting nanowires constituted of metallic nanoparticles filled in inorganic nanotubes with a inner cavity of 7 nm and an isolating wall with a thick ranging from 7 to 21 nm.

References

1. Schmid G, Pfeil R, Boese R, et al. $Au_{55}[P(C_6H_5)3]_{12}Cl_6$ - a gold cluster of unusual size. Chemische Berichte 1981;114(11):3634-42.

2. Brust M, Walker M, Bethell D, et al. Synthesis of Thiol-derivatized Gold Nanoparticles in a Two-phase Liquid-Liquid System. J Chem Soc, Chem Commun 1994;801-2.

3. Allen C. Templeton, W. Peter Wuelfing, Royce W. Murray. Monolayer-Protected Cluster Molecules. Acc Chem Res 2000;33(1):27–36.

4. Daniel MC, Didier Astruc D. Gold Nanoparticles: Assembly, Supramolecular Chemistry, Quantum-Size-Related Properties, and Applications toward Biology, Catalysis, and Nanotechnology. Chem Rev 2004;104:293–346.

5. Shon YS, Choo H. Organic reactions of Monolayer-Protected Metal Nanoparticles. In: Astruc D editor. Dendrimers and Nanosciences. Volume 6, Paris: CR Chime; 2003, p. 1009-1018.

6. Y. -S. Shon, "Metal nanoparticles protected with monolayers:
synthetic methods," in Dekker Enciclopedia of Nanoscience and
Nanotechnology, Taylor & Francis, Oxford, UK, 2004.

7. Jagminas A, Gailiute I, Niaura G, Giraitis R. Template-assisted fabrication of pure Se nanocrystals in controllable dimensions. Chemija 2005;16:15-20.

8. Zhang B, Ye X, Dai W, et al. Biomolecule-assisted synthesis of single-crystalline selenium nanowires and nanoribbons via a novel flake-cracking mechanism. Nanotechnology 2006;17:385-90.

9. Ulman, A. Formation and structure of self-assembled monolayers. Chem. Rev. 1996, 96, 1533–1554.

10. Giersig, M.; Mulvaney, P. Preparation of ordered colloid monolayers by electrophoretic deposition. Langmuir 1993, 9, 3408–3413.
11.Leff, D.V.; Ohara, P.C.; Heath, J.R.; Gelbart, W.M. Thermodynamic control of gold nanocrystal size: Experiment and theory. J. Phys. Chem. 1995, 99, 7036–7041.

12. Hostetler, M.J.; Wingate, J.E.; Zhong, C.-J.; Harris, J.E.; Vachet, R.W.; Clark, M.R.; Londono, J.D.; Green, S.J.; Stokes, J.J.; Wignall, G.D.; Glish, G.L.; Porter, M.D.; Evans, N.D.; Murray, R.W. Alkanethiolate gold cluster molecules with core diameters from 1.5 to 5.2 nm: Core and monolayer properties as a function of core size. Langmuir 1998, 14, 17–30.

13. Jana, N.R.; Gearheart, L.; Murphy, C.J. Evidence for seed-mediated nucleation in the chemical reduction of gold salts to gold nanoparticles. Chem. Mater. 2001, 13, 2313–2322.

14. Clarke, N.Z.; Waters, C.; Johnson, K.A.; Satherley, J.; Schiffrin, D.J. Size-dependent solubility of thiolderivatized gold nanoparticles in supercritical ethane. Langmuir 2001, 17, 6048–6050.

15. Hicks, J.F.; Miles, D.T.; Murray, R.W. Quantized double-layer charging of highly monodisperse metal nanoparticles. J. Am. Chem. Soc. 2002, 124, 13322–13328.

16. Brust, M.; Fink, J.; Bethell, D.; Schiffrin, D.J.; Kiely, C.J. Synthesis and reactions of functionalised gold nanoparticles. J. Chem. Soc., Chem. Commun. 1995, 1655–1656.

17. Paulini, R.; Frankamp, B.L.; Rotello, V.M. Effects of branched ligands on the structure and stability of monolayers on gold nanoparticles. Langmuir 2002, 18, 2368–2373.

18. Foos, E.E.; Snow, A.W.; Twigg, M.E.; Ancona, M.G. Thiol-terminated di-, tri-, and tetraethylene oxide functionalized gold nanoparticles: A watersoluble, charge-neutral cluster. Chem. Mater. 2002, 14, 2401–2408.

19. Kim, K.-S.; Demberelnyamba, D.; Lee, H. Sizeselective synthesis of gold and platinum nanoparticles using novel thiol-functionalized ionic liquids. Langmuir 2004, 20, 556–560.

20. Yonezawa, T.; Onoue, S.; Kimizuka, N. Formation of uniform fluorinated gold nanoparticles and their highly ordered hexagonally packed monolayer. Langmuir 2001, 17, 2291–2293.

21. Fitzmaurice, D.; Rao, S.N.; Preece, J.A.; Stoddart, J.F.; Wenger, S.; Zaccheroni, N. Heterosupramolecular chemistry: Programmed pseudorotaxane assembly at the surface of a nanocrystal. Angew. Chem., Int. Ed. 1999, 38, 1147–1150.

22. Choo, H.; Cutler, E.; Shon, Y.-S. Synthesis of mixed monolayer-protected gold clusters from thiol mixtures: Variation in the tail group, chain length, and solvent. Langmuir 2003, 19, 8555–8559.

23. Link, S.; Beeby, A.; FitzGerald, S.; El-Sayed, M.A.; Schaaff, T.G.; Whetten, R.L. Visible to infrared luminescence from a 28-atom gold cluster. J. Phys. Chem. B 2002, 106, 3410–3415.

24. Tan, Y.; Li, Y.; Zhu, D. Fabrication of gold nanoparticles using a trithiol (thiocyanuric acid) as the capping agent. Langmuir 2002, 18, 3392–3395.

25. Fe´lidj, N.; Aubard, J.; Le´vi, G.; Krenn, J.R.; Hohenau, A.; Schider, G.; Leitner, A.; Aussenegg, F.R. Optimized surface-enhanced Raman scattering on gold nanoparticle arrays. Appl. Phys. Lett. 2003, 82, 3095–3097.

26. Liu, J.; Alvarez, J.; Ong, W.; Roma´n, E.; Kaifer, A.E. Phase transfer of hydrophilic, cyclodextrinmodified gold nanoparticles to chloroform solutions. J. Am. Chem. Soc. 2001, 123, 11148–11154.

27. Mitra, S.; Nair, B.; Pradeep, T.; Goyal, P.S.; Mukhopadhyay, R. Alkyl chain dynamics in monolayer- protected clusters (MPCs): A quasielastic neutron-scattering investigation. J. Phys. Chem. B 2002, 106, 3960–3967.

28. He, S.; Yao, J.; Jiang, P.; Shi, D.; Zhang, H.; Xie, S.; Pang, S.; Gao, H. Formation of silver nanoparticles and self-assembled two-dimensional ordered superlattice. Langmuir 2001, 17, 1571–1575.

29. Bunge, S.D.; Boyle, T.J.; Headley, T.J. Synthesis of coinage-metal nanoparticles from mesityl precursors. Nano Lett. 2003, 3, 901–905.

30. Manna, A.; Imae, T.; Iida, M.; Hisamatsu, N. Formation of silver nanoparticles from a N-hexadecylethylenediamine silver nitrate complexes. Langmuir 2001, 17, 6000–6004.

31. Rodriguez-Gattorno, G.; Diaz, D.; Rendo´n, L.; Herna´ndez-Segura, G.O. Metallic nanoparticles from spontaneous reduction of silver(I) in DMSO. Interaction between nitric oxide and silver nanoparticles. J. Phys. Chem. B 2002, 106, 2482–2487.

32. Porter, L.A., Jr.; Ji, D.; Westcott, S.L.; Graupe, M.; Czernuszewicz, R.S.; Halas, N.J.; Lee, T.R. Gold and silver nanoparticles functionalized by the adsorption of dialkyl disulfides. Langmuir 1998, 14, 7378–7386.

33. Yonezawa, T.; Onoue, S.; Kimizuka, N. Preparation of highly positively charged silver nanoballs and their stability. Langmuir 2000, 16, 5218–5220.

34. Kim, S.J.; Kim, T.G.; Ah, C.S.; Kim, K.; Jang, D.-J. Photolysis dynamics of benzyl phenyl sulphide adsorbed on silver nanoparticles. J. Phys. Chem. B 2004, 108, 880–882.

35. Shon, Y.-S.; Cutler, E. Aqueous synthesis of alkanethiolate-protected metal nanoparticles using bunte salts. Langmuir 2004, 20, 6626–6630.

36. Tan, Y.; Wang, Y.; Jiang, L.; Zhu, D. Thiosalicylic acid-functionalized silver nanoparticles synthesized in one-phase system. J. Colloid Interface Sci. 2002, 249, 336–345.

37. Tzhayik, O.; Sawant, P.; Efrima, S.; Kovalev, E.; Klug, J.T. Xanthate capping of silver, copper, and gold colloids. Langmuir 2002, 18, 3364–3369.

38. Bunge, S.D.; Boyle, T.J.; Headley, T.J. Synthesis of coinage-metal nanoparticles from mesityl precursors. Nano Lett. 2003, 3, 901–905.

39. Manna, A.; Imae, T.; Iida, M.; Hisamatsu, N. Formation of silver nanoparticles from a N-hexadecylethylenediamine silver nitrate complexes. Langmuir 2001, 17, 6000–6004.

40. Rodriguez-Gattorno, G.; Diaz, D.; Rendo´n, L.; Herna´ndez-Segura, G.O. Metallic nanoparticles from spontaneous reduction of silver(I) in DMSO. Interaction between nitric oxide and silver nanoparticles. J. Phys. Chem. B 2002, 106, 2482–2487.

41. Lin, X.Z.; Teng, X.; Yang, H. Direct synthesis of narrowly dispersed silver nanoparticles using a single-source precursor. Langmuir 2003, 19, 10081–10085.

42. Wang, W.; Chen, X.; Efrima, S. Silver nanoparticles 10 Metal Nanoparticles Protected with Monolayers: Synthetic Methods capped by long-chain unsaturated carboxylates. J. Phys. Chem. B 1999, 103, 7238–7246.

43. Bae, S.J.; Lee, C.; Choi, I.S.; Hwang, C.-S.; Gong, M.; Kim, K.; Joo, S.-W. Adsorption of 4-biphenylisocyanide on gold and silver nanoparticle surfaces: Surface-enhanced Raman scattering study. J. Phys. Chem. B 2002, 106, 7076–7080.

44. Hranisavljevic, J.; Dimitrijevic, N.M.; Wurtz, G.A.; Wiederrecht, G.P. Photoinduced charge separation reactions of J-aggregates on silver nanoparticles. J. Am. Chem. Soc. 2002, 124, 4536–4537.

45. Mitra, S.; Nair, B.; Pradeep, T.; Goyal, P.S.; Mukhopadhyay, R. Alkyl chain dynamics in monolayer- protected clusters (MPCs): A quasielastic neutron-scattering investigation. J. Phys. Chem. B 2002, 106, 3960–3967.

46. He, S.; Yao, J.; Jiang, P.; Shi, D.; Zhang, H.; Xie, S.; Pang, S.; Gao, H. Formation of silver nanoparticles and self-assembled two-dimensional ordered superlattice. Langmuir 2001, 17, 1571–1575.

47. Shah, P.S.; Holmes, J.D.; Doty, R.C.; Johnston, K.P.; Korgel, B.A. Steric stabilization of nanocrystals in supercritical CO2 using fluorinated ligands. J. Am. Chem. Soc. 2000, 122, 4245–4246.

48. Liu, J.; Ong, W.; Kaifer, A.E. A ‘‘macrocyclic effect’’ on the formation of capped silver nanoparticles in DMF. Langmuir 2002, 18, 5981–5983

49. Huang, T.; Murray, R.W. Luminescence of tiopronin monolayer-protected silver clusters changes to that of gold clusters upon galvanic core metal exchange. Langmuir 2003, 107, 7434–7440.

50. Yonezawa, T.; Onoue, S.; Kimizuka, N. Preparation of highly positively charged silver nanoballs and their stability. Langmuir 2000, 16, 5218–5220.

51. Kim, S.J.; Kim, T.G.; Ah, C.S.; Kim, K.; Jang, D.-J. Photolysis dynamics of benzyl phenyl sulphide adsorbed on silver nanoparticles. J. Phys. Chem. B 2004, 108, 880–882.

52. Shon, Y.-S.; Cutler, E. Aqueous synthesis of alkanethiolate-protected metal nanoparticles using bunte salts. Langmuir 2004, 20, 6626–6630.

53. Tan, Y.; Wang, Y.; Jiang, L.; Zhu, D. Thiosalicylic acid-functionalized silver nanoparticles synthesized in one-phase system. J. Colloid Interface Sci. 2002, 249, 336–345.

54. R. A. Salkar, P. Jeevanandam, G. Kataby, et al., “Elongated copper nanoparticles coated with a zwitterionic surfactant,” The Journal of Physical Chemistry B, vol. 104, no. 5, pp. 893–897, 2000.

55. S. Chen and J.M. Sommers, “Alkanethiolate-protected copper nanoparticles: spectroscopy, electrochemistry, and solid-state morphological evolution, The Journal of Physical Chemistry B, vol. 105, no. 37, pp. 8816–8820, 2001.

56. K. J. Ziegler, R. C. Doty, K. P. Johnston, and B. A. Korgel, “Synthesis of organic monolayer-stabilized copper nanocrystals in supercritical water, Journal of the American Chemical Society, vol. 123, no. 32, pp. 7797–7803, 2001. 6 Journal of Nanomaterials

57. N. Sandhyarani and T. Pradeep, “Crystalline solids of alloy clusters,” Chemistry ofMaterials, vol. 12, no. 6, pp. 1755–1761, 2000.

58. J. C. Love, L. A. Estroff, J. K. Kriebel, R. G. Nuzzo, and G.M. Whitesides, “Self-assembledmonolayers of thiolates onmetals as a form of nanotechnology,” Chemical Reviews, vol. 105, no. 4, pp. 1103–1170, 2005.

59. Michael B. Sigman, Jr., Ali Ghezelbash, Tobias Hanrath, Aaron E. Saunders, Frank Lee, and Brian A. Korgel Solventless Synthesis of Monodisperse Cu2S Nanorods, Nanodisks, and Nanoplatelets J. AM. CHEM. SOC. 9 VOL. 125, NO. 51, 2003)

60. G. N. Schrauzer and H. Prakash, Inorg. Chem., 1975, 14, 1200

61. Andreas Haubrich; Mayra van Klaveren, Gerard van Koten;. Gabriele Handke; and Norbert Krause, 1,g-Addition of Organolithium Compounds to Acceptor-Substituted Enynes Catalyzed by a Copper(1) Arenethiolate, J. Org. Chem. 1993,58, 5849-5852 5

62. M. van Klavereen, F. Lambert, D. J. M. F. Eijkelkamp, D. M. Grove and G. van Koten, Tetrahedron Lett., 1994, 35, 6135(a); A. Haubrich, M. van Klavereen and G. van Koten, J. Org. Chem., 1993, 58, 5849(b); M. van Klavereen, E. S. M. Persson, D. M. Grove, J.-E. Backvall and G. van Koten, Tetrahedron Lett., 1994, 35, 5931(c); M. van Klavereen, E. S. M. Persson, A. del Villar, D. M. Grove, J.-E Backvall and G. van Koten, Tetrahedron Lett., 1995, 36, 3059(d); M. van Klavereen, E. S. M. Persson, D. M. Grove, J.-E Backvall and G. van Koten, Chem. Eur. J., 1995, 1, 351(e)

63. S John T. York, Itsik Bar-Nahum, and William B. Tolman. Structural Diversity in Copper Sulfur Chemistry: Synthesis of Novel Cu/S Clusters through Metathesis Reactions Inorganic Chemistry, Vol. 46, No. 20, 2007

64. Mohammed Aslam, G. Gopakumar, T. L. Shoba, I. S. Mulla, K. Vijayamohanan, S. K. Kulkarni, J. Urban, and W. Vogel, Formation of Cu and Cu_2O Nanoparticles by Variation of the Surface Ligand: Preparation, Structure, and Insulating-to-Metallic Transition Journal of Colloid and Interface Science, 255, Issue 1, 1 November 2002, 79-90

65. T. P. Ang,T. S. A. Wee, and W. S. Chin, Three-Dimensional Self-Assembled Monolayer (3D SAM) of n-Alkanethiols on Copper Nanoclusters J. Phys. Chem. B 2004, 108, 11001-11010)

66. Shaowei Chen and Jennifer M. Sommers, Alkanethiolate-Protected Copper Nanoparticles: Spectroscopy, Electrochemistry, and Solid-State Morphological Evolution, J. Phys. Chem. B 2001, 105, 8816-8820

67. J.S. Zhang, H.L. Wang, Y.P. Bao, L.D. Zhang, Life Sci. 75 (2004)237.

68. B. Huang, J.S. Zhang, J.W. Hou, C. Chen, Free Radic. Biol. Med. 35 (2003) 805.

69. (i) D.A. Buckley, Red amorphous selenium. U.S. Patent 3,954,951, May 4, 1976; (ii) L. De Brouchere, A. Watillon, F. Van Grunderbuck, Nature (London) 178 (1956) 589; (iii) N.M. Dimitrijevic, P.V. Kamat, Langmuir 4 (1987) 782.

70. K.D. Gupta, S.R. Das, Indian J. Phys. 15 (1941) 401.

71. A.M.J. Shaker, Colloid Interface Sci. 180 (1996) 225

72. D.R. Mees, W. Pysto, P.J.J. Tarcha, Colloid Interface Sci. 170 (1995) 254.

73. Zong-Hong Lin, C.R. Chris Wang, Evidence on the size-dependent absorption spectral evolution of selenium nanoparticles, Materials Chemistry and Physics 92 (2005) 591–594

74. Sanghoo Lee , Chanho Kwon , Baeho Park, Seunho Jung, Synthesis of selenium nanowires morphologically directed by Shinorhizobial oligosaccharides Carbohydrate, Research 344 (2009) 1230–1234 .

75. Xueyun Gao, Jinsong Zhang, and Lide Zhang, Hollow Sphere Selenium Nanoparticles: Their In-Vitro Anti Hydroxyl Radical Effect, Adv. Mater. 2002, 14, No. 4

76. Guangcheng Xi, Kan Xiong, Qingbiao Zhao, Rui Zhang, Houbo Zhang, and Yitai Qian Nucleation-Dissolution-Recrystallization: A New Growth Mechanism for t-Selenium Nanotubes Crystal Growth & Design, Vol. 6, No. 2, 2006

77. Acid-induced synthesis of polyvinyl alcohol-stabilized selenium nanoparticles C P Shah, M Kumar and P N Bajaj, Nanotechnology 18 (2007) 385607)

78. Ihnat M. Occurence and Distribution of Selenium. CRC Press, Boca Raton, FL, USA; 1987, p. 1–347.

79. Foster LH, Sumar S. Selenium in health and disease: A review. Crit Rev Food Sci Nutr 1997;37:211-28.

80. Tinggi U. Essentiality and toxicity of selenium and its status in Australia: a review. Toxicol Lett 2003;137:103-10.

81. Flohé L, Günzler EA, Schock HH. Glutathione peroxidase: a selenoenzyme. FEBS Lett 1973;32: 132-34.

82. Rotruck JT, Pope AL, Ganther HE, et al. Selenium: Biochemical Role as a Component of Glutathione Peroxidase. Science 1973;179:588-90.

83. Böck A. Selenium Proteins Containing Selenocysteine: In: King RB editor. Encyclopedia of Inorganic Chemistry. Volume 8, Chichester, England: John Wiley & Sons; 1994, p. 3700.

84. Boyington JC, Gladyshev VN, Khangulov SV, et al. Crystal structure of formate dehydrogenase H: catalysis involving Mo, molybdopterin, selenocysteine, and an Fe_4S_4 cluster. Science 1997;275: 1305-8.

85. Pfeiffer M, Bingemann R, Klein A. Fusion of two subunits does not impair the function of a [NiFeSe]-hydrogenase in the archaeon Methanococcus voltae. Eur J Biochem 1998;256:447-52.

86. Wagner M, Sonntag D, Grimm R, et al. Substrate-specific selenoprotein B of glycine reductase from Eubacterium acidaminophilum. Biochemical and molecular analysis. Eur J Biochem 1999; 260:38-49.

87. Chu F-F, Doroshow JH, Esworthy RS. Expression, characterization. and tissue distribution of a new cellular selenium-dependent glutathione peroxidise. J Biol Chem 1993;268:2571-6.

88. Rayman MP: The importance of selenium to human health. Lancet 2000;356:233-41.

89. Combs GF jr. Selenium in global food systems. Br J Nutr 2001;85:517-47.

90. Whanger PD. Selenocompounds in Plants and Animals and their Biological Significance. J Am Coll Nutr 2002;21:223-32.

91. Mugesh G, du Mont W-W, Sies H. Chemistry of Biologically Important Synthetic Organoselenium Compounds Chem Rev 2001;101: 2125-79.

92. Organic Selenium Compounds: Their Chemistry and Biology. Klayman DL, Gűnther WHH, editors. New York: Wiley; 1973.

93. Shamberger RJ. Biochemistry of Selenium., New York: Plenum Press; 1983.

94. Parnham MJ, Graf E. Pharmacology of synthetic organic selenium compounds. Prog Drug Res 1991;36:9-47.

95. Sies H, Masumoto H. Ebselen as a glutathione peroxidase mimic and as a scavenger of peroxynitrite. Adv Pharmacol 1997;38:229-46.

96. Leonard KA, Hall JP, Nelen MI, et al. A selenopyrylium photosensitizer for photodynamic therapy related in structure to the antitumor agent AA1 with potent in vivo activity and no long-term skin photosensitization. J Med Chem 2000;43:4488-98.

97. Ip C. Selenium inhibition of chemical carcinogenesis. Fed Proc 1985;44:2573-78.

98. Milner JA. Effect of selenium on virally induced and transplantable tumor models. Fed Proc 1985;44:2568-72.

99. Schrauzer GN. Anticarcinogenic effects of selenium. Cell Mol Life Sci 2000;57:1862-73.

100. Clark LC, Combos JG, Turnbill BW, et al. Effects of Selenium Supplementation for Cancer Prevention in Patients With Carcinoma of the Skin: A Randomized Controlled Trial. J Am Med Assoc 1996;276:1957-63

101. Ormland RS, Herbel MJ, Blum JS, et al. Structural and Spectral Features of Selenium Nanospheres Produced by Se-Respiring Bacteria. Appl Environ Microbiol 2004;70:52-60.

102. Mishra B, Hassan PA, Pryadarsini KI, Mohan H. Reactions of Biological Oxidants with Selenourea: Formation of Redox Active Nanoselenium. J Phys Chem 2005;109:12718-23.

103. Kopeikin VV, Valueva SV, Kipper AI, et al. Adsorption of hydroxyethyl cellulose selenium nanoparticles during their formation in water. Russ J Appl Chem 2003;76(4):600-2.

104. Kopeikin VV, Valueva SV, Kipper AI, et al. Synthesis of selenium nanoparticles in aqueous solutions of poly(vinylpyrrolidone) and morphological characteristics of the related nanocomposites. Polym Sci Ser A 2003;45:374-9.

105. Zhang J, Zhang SY, XU JJ, Chen HY. A New Method for the Synthesis of Selenium Nanoparticles and the Application to Construction of H_2O_2 Biosensor. Chinese Chemical Letters 2004;15 (11):1345-48.

106. Shah CP, Kumar M, Bajaj PN. Acid-induced synthesis of polyvinyl alcohol- stabilized selenium nanoparticles. Nanotechnology 2007;18:385607.

107. Xi G, Xiong K, Zhao Q, et al. Nucleation – Dissolution –Recrystallization : A New Growth Mechanism for t-Selenium Nanotubes. Cryst Growth Des 2006;6(2):577-82.

108. Lickes JP, Dumont F, Buess-Herman C. Optical properties of rod-shaped selenium hydrosols. Colloids Surfaces 1996;118:167-70.

109. Zhang B, Hou W, Zhu X, et al. Multiarmed Tubular Selenium with Potentially Unique Electrical Properties: Solution-Phase Synthesis and First- Principles Calculation. Small 2007;3(1): 101-5.

110. Nadagouda MN, Varma RS. Green and controlled synthesis of gold and platinum nanomaterials using vitamin B_2: density-assisted self-assembly of nanospheres, wires and rods. Green Chem 2006;8:516 – 8.

111. Nadagouda MN, Varma RS. A Greener Synthesis of Core (Fe, Cu)-Shell (Au, Pt, Pd, and Ag) Nanocrystals Using Aqueous Vitamin C. Cryst Growth Des 2007;7(12):2582-87.

112. Molan AL, Flanagan J, Wei W, Moughan PJ. Selenium-containing green tea has higher antioxidant and prebiotic activities than regular green tea. Food Chemistry 2009;114:829-35.

113. Egorova EM, Revina AA. Synthesis of metallic nanoparticles in reverse micelles in the presence of quercitin. Colloids Surfaces 2000;168:87-96.

114. Kang KA, Lee KH, Chae S, et al. Cytoprotective Effect of Phloroglucinol on Oxidative Stress Induced Cell Damage via Catalase Activation. J Cell Biochem 2006;97:609–20.

115. Francisco R.M. Laurindo, MD; Protasio L. da Luz MD, et al. Evidence for Superoxide Radical-Dependent Coronary Vasospasm After Angioplasty in Intact Dogs. Circulation 1991;83(5):1705-15.

116. Nakazono K, Watanabe N, Matsuno K, et al. Does superoxide underlie the pathogenesis of hypertension? Physiology Proc. Natl. Acad. Sci. USA. 1991;88:10045-8.

117. Parthasarathy S, Steinberg D, Witztum JL. The Role of Oxidized Low-Density Lipoproteins in the Pathogenesis of Atherosclerosis. Annual Review of Medicine 1992;43:219-25.

118. Palinski W, Tangirala RK, Miller E, et al. Increased Autoantibody Titers Against Epitopes of Oxidized LDL in LDL Receptor–Deficient Mice With Increased Atherosclerosis. Arteriosclerosis, Thrombosis, and Vascular Biology 1995;15:1569-76.

119. Darley-Usmar V, Halliwell B. Blood radicals: reactive nitrogen species, reactive oxygen species, transition metal ions, and the vascular system. Pharm Res 1996;13(5):649–62.

120. Farinati F, Cardin R, Degan P, et al. Oxidative DNA damage accumulation in gastric carcinogenesis. Gut 1998;42:351–6.

121. R.L. Perkins and B.W. Harvey, Method for the Determination of Asbestos in Bulk Building Materials, EPA-600/R-93/116, 1993.

122. F.J. Wicks and D.S. O'Hanley: Serpentine minerals: Structures and petrology. Rev. Mineral. 19, 91, 1988.

123. K. Yada: Growth and microstructure of synthetic chrysotile. Am. Mineral. 62, 958, 1977.

124. F. Pott: Animal experiments on biological effects of mineral fibers. I. Arc. 2, 261 (1980 (5;42).42.

125]. R.P. Nolan, A.M. Langer, G.W. Oechesle, J. Addison, and D.E. Colflesh: Mechanisms in Fiber Carcinogenesis, edited by R.C. Brown (Plenum Press, New York, 1991) p. 231.

126. C. Riganti, E. Aldieri, L. Bergandi, I. Fenoglio, C. Costamagna, B. Fubini, A. Bosia, and D. Ghigo: Crocidolite asbestos inhibits pentose phosphate oxidative pathway and glucose 6-phosphate dehydrogenase activity in human lung epithelial cells. Free Radical Biol. Med. 32(9), 938 (2002).

127. C.B. Manning, V. Vallyathan, and B.T. Mossman: Diseases caused by asbestos: Mechanisms of injury and disease development. Int. J. Immunopharmacol. 2, 191 (2002).

128. M.C. Jaurand: Mechanisms of fiber-induced genotoxicity. Environ. Health Perspect. 105, 1073 (1997).

129. D.W. Kamp, V. Panduri, S.A. Weitzman, and N. Chandel: Asbestos-induced alveolar epithelial cell apoptosis: Role of mitochondrial dysfunction caused by iron-derived free radicals.
Mol. Cell. Biochem. 234/235(1&2), 153 (2002)

130. J. Cai and D.P. Jones: Superoxide in apoptosis. Mitochondrial generation triggered by cytochrome c loss. J. Biol. Chem. 273(19), 11401 (1998).

131. J. Jurinski and J.D. Rimstidt: Biodurability of talc. Am. Mineral. 86(4), 392 (2001).

132. J.M. Davis, J. Addison, R.E. Bolton, K. Donaldson, A.D. Jones, and T. Smith: The pathogenicity of long versus short fibre samples of amosite asbestos administered to rats by inhalation and intraperitoneal injection. Br. J. Exp. Pathol. 67(3), 415 (1986).

133. K. Miller: The effects of asbestos on macrophages. Crit. Rev. Toxicol. 5(4), 319 (1978).

134. F. Valerio, M. De Ferrari, L. Ottaggio, E. Repetto, and L. Santi: Cytogenetic effects of Rhodesian chrysotile on human lymphocytes in vitro. IARC Sci. Publ. 30, 485 (1980).

135. V.N. Bogomolov: Liquids in ultrafine channels. (Filamentary and cluster crystals). Usp. Fiz. Nauk. 124(1), 171 (1978). and metal-organic chemical vapor deposition (MOCVD)

136. H.M. Yates, W.R. Flavell, M.E. Pemble, N.P. Johnson, S.G. Romanov, and C.M. Sotomayor-Torres: Novel quantum confined structures via atmospheric pressure MOCVD growth in asbestos and opals. J. Cryst. Growth 170(1–4), 611 (1997).

137. S.G. Romanov and C.M. Sotomayor Torres: Nanoscale Science and Technology, edited by N. Garia, M. Nieto-Vesperinas, and H. Rohrer (Kluwer Academic Publisher, Dordrecht, The Netherlands, 1997) p. 225.

138. V. Dneprovskii, E. Zhukov, V. Karavanskii, V. Poborchii, and I. Salamatina: Nonlinear optical properties of semiconductor quantum wires. Superlattices Microstruct. 23(6), 1217 (1998).

139. V.V. Poborkii, V.I. Al'perovich, Y. Nozoue, N. Ohnishi, A. Kasuya, and O. Terasaki: Fabrication and optical properties of ultrathin CdSe filaments incorporated into the nanochannels of fibrous magnesium silicates. J. Phys.: Condens. Matter 9, 5687 (1997).

140 C.T. Kresge, M.E. Leonowicz, W.J. Roth, J.C. Vartuli, and J.S. Beck: Ordered mesoporous molecular sieves synthesized by a liquid-crystal template mechanism. Nature 359, 710 (1992).

141. G. Falini, E. Foresti, I.G. Lesci, and N. Roveri: Structural and morphological characterization of synthetic chrysotile single crystals. Chem. Commun. 14, 1512 (2002).

142. K. Yada: Study of chrysotile asbestos by a high resolution electron microscope. Acta Crystallogr. 23, 704 (1967).

143. M. Mellini: The crystal structure of lizardite 1T: Hydrogen bonds and polytypism. Am. Mineral. 67(5-6), 587 (1982).

144. M.M.J. Treacy, J.M. Newsam, and M.V. Deem: A general recursion method for calculating diffracted intensities from crystals containing planar faults. Proc. R. Soc. London A 433, 499 (1991).

145. M. Leoni, A.F. Gualtieri, and N. Roveri: Simultaneous refinement of structure and microstructure of layered materials. J. Appl. Crystallogr. 37(1), 166 (2004).

146. A.F. Gualtieri and G. Artioli: Quantitative determination of chrysotile asbestos in bulk materials by combined Rietveld and RIR methods. Powder Diffr. 10, 269 (1995).

147. F.J. Wicks: Comment on "Status of the reference x-ray powder diffraction patterns for the serpentine minerals in the PDF database-1997". Powder Diffr. 15, 42 (2000).

148. G. Falini, E. Foresti, M. Gazzano, A.F. Gualtieri, M. Leoni, I.G. Lesci, and N. Roveri: Tabular-shaped stoichiometric chrysotile nanocrystals. Chem.-Eur. J. 10, 3043 (2004).

149. E.N. Korytkova, A.V. Maslov, L.N. Pivovarova, I.A. Drozdova, and V.V. Gusarov: Formation of Mg3Si2O5(OH)4 nanotubes under hydrothermal conditions. Glass Phys. Chem. 30(1), 51 (2004).

150. Katz, E., and Willner, I., Angew. Chem. Int. Ed. (2004) 43, 6042

151. M. Brust, M. Walker, D. Bethell, D.J. Schiffrin, and R. Whyman: Synthesis of thiol-derivatized gold nanoparticles in a two-phase liquid-liquid system. Chem. Commun. 7, 801 (1994)

152. C.J. Zhong, J. Luo, M.M. Maye, L. Han, and N. Kariuki: Nanostructured gold and alloy electrocatalysts. Nanotechnology in Catalysis 1, 221 (2004).

153. Larson, A.C.; Von Dreele, R.B., GSAS Generalized Structure Analysis System. (1994) Laur 86-748. Los Alamos national laboratory, Los Alamos, New Mexico.

154. Cattaneo, A.; Gualtieri, A. F.; Artioli, G. Physics and Chemistry of Minerals 2003, 30, 177-183.